The Wind Imaging Interferometer (WINDII) on the upper atmosphere research satellite: A 20 year perspective

Gordon G. Shepherd, Gérard Thuillier, Young-Min Cho, Marie-Louise Duboin, Wayne F. J. Evans, William Gault, Charles Hersom, David Kendall, Chantal Lathuillere, R. P. Lowe, et al.

THE WIND IMAGING INTERFEROMETER (WINDII) ON THE UPPER ATMOSPHERE RESEARCH SATELLITE: A 20 YEAR PERSPECTIVE

G. G. Shepherd,[1] G. Thuillier,[2] Y.-M. Cho,[1] M.-L. Duboin,[3] W. F. J. Evans,[1] W. A. Gault,[1] C. Hersom,[4] D. J. W. Kendall,[5] C. Lathuillère,[6] R. P. Lowe,[7] I. C. McDade,[1] Y. J. Rochon,[8] M. G. Shepherd,[1] B. H. Solheim,[1] D.-Y. Wang,[9] and W. E. Ward[9]

Received 23 January 2012; revised 13 April 2012; accepted 16 April 2012; published 8 June 2012.

[1] The Wind Imaging Interferometer (WINDII) was launched on the NASA's Upper Atmosphere Research Satellite on 12 September 1991 and operated until 2003. Its role in the mission was to measure vector winds in the Earth's atmosphere from 80 to 110 km, but its measurements extended to nearly 300 km. The approach employed was to measure Doppler shifts from a suite of visible region airglow lines emitted over this altitude range. These included atomic oxygen O(^{1}S) and O(^{1}D) lines, as well as lines in the OH Meinel (8,3) and O_2 Atmospheric (0,0) bands. The instrument employed was a Doppler Michelson Interferometer that measured the Doppler shift as a phase shift of the cosinusoidal interferogram generated by single airglow lines. An extensive validation program was conducted after launch to confirm the accuracy of the measurements. The dominant wind field, the first one observed by WINDII, was that of the migrating diurnal tide at the equator. The overall most notable WINDII contribution followed from this: determining the influence of dynamics on the transport of atmospheric species. Currently, nonmigrating tides are being studied in the thermosphere at both equatorial and high latitudes. Other aspects investigated included solar and geomagnetic influences, temperatures from atmospheric-scale heights, nitric oxide concentrations, and the occurrence of polar mesospheric clouds. The results of these observations are reviewed from a perspective of 20 years. A future perspective is then projected, involving more recently developed concepts. It is intended that this description will be helpful for those planning future missions.

Citation: Shepherd, G. G., et al. (2012), The Wind Imaging Interferometer (WINDII) on the Upper Atmosphere Research Satellite: A 20 year perspective, *Rev. Geophys.*, *50*, RG2007, doi:10.1029/2012RG000390.

1. THE WINDII METHOD OF WIND MEASUREMENT

[2] The Wind Imaging Interferometer (WINDII), launched on 12 September 1991 on the National Aeronautics and Space Administration (NASA) Upper Atmosphere Research Satellite (UARS), embodied the first use in space of what may be called Doppler Michelson Imaging (DMI). (All acronyms and abbreviations used in the paper are listed in Table 1.) The Michelson interferometer employed was novel in three aspects: (1) it was field-widened, (2) the Doppler measurement was made by phase stepping over one fringe of the interferogram, and (3) it was thermally phase stable, allowing the measurement of wind velocity.

[3] Field widening in spectroscopic instruments was originally conceived by *Connes* [1956], using afocal telescopes in the two arms of a Michelson interferometer. *Bouchareine and Connes* [1963] replaced the telescopes with sliding prisms. *Hilliard and Shepherd* [1966a] recognized that field-widened Doppler temperatures could be measured from atomic line widths using a single plate of glass in one arm of the interferometer. Fundamentally, field widening involves using materials of lengths d_1 and d_2 with corresponding refractive indices n_1 and n_2 in the two arms of the interferometer; the expression for optical path difference

[1]Centre for Research in Earth and Space Science, York University, Toronto, Ontario, Canada.
[2]Service d'Aéronomie, CNRS, Verrières le Buisson, France.
[3]Formerly at Université de Paris, Paris, France.
[4]Spectral Applied Research, Inc., Richmond Hill, Ontario, Canada.
[5]Canadian Space Agency, Saint-Hubert, Quebec, Canada.
[6]UJF-Grenoble 1/CNRS-INSU, Institut de Planétologie et d'Astrophysique de Grenoble (IPAG) UMR 5274, Grenoble, France.
[7]Department of Physics and Astronomy, University of Western Ontario, London, Ontario, Canada.
[8]Environment Canada, Toronto, Ontario, Canada.
[9]Department of Physics, University of New Brunswick, Fredericton, New Brunswick, Canada.

Corresponding author: G. G. Shepherd, Centre for Research in Earth and Space Science, York University, 4700 Keele St., Toronto, ON M3J 1P3, Canada. (gordon@yorku.ca)

8755-1209/12/2012RG000390
Paper number 2012RG000390

TABLE 1. List of Acronyms and Abbreviations

Acronym/ Abbreviation	Definition
AGU	American Geophysical Union
AI	artificial intelligence
ANLC	Airborne Noctilucent Cloud campaigns
CARMA	Community Aerosol and Radiation Model for Atmospheres
CCD	charge-coupled device
CMAM	Canadian Middle Atmosphere Model
CLIO	circle to line interferometer optical (system)
DASH	Doppler Asymmetric Spatial Heterodyne (interferometer)
DMI	Doppler Michelson Interferometer
DMSP	Defense Meteorological Satellite Program
DTM	Drag Temperature Model
DWM	Disturbance Wind Model
EISCAT	European Incoherent Scatter (facility)
EP	Eliassen-Palm (fluxes)
ETON	Energy Transfer in Oxygen Nightglow
EUV	extreme ultraviolet
FOV	field of view
FWHM	full width at half maximum
GOES	Geostationary Operational Environmental Satellite
HIRES	High Resolution Echelle Spectrometer
HRDI	High Resolution Doppler Imager
HWM	Horizontal Wind Model
IRI	International Reference Ionosphere
LOS	line of sight
MICADO	Michelson Interferometer for Coordinated Auroral Doppler Observations
MF	medium frequency (radar)
MLS	Microwave Limb Sounder
MLT	mesosphere and lower thermosphere
MR	meteor radar
MSAO	mesospheric semiannual oscillation
MSIS	Mass Spectrometer and Incoherent Scatter (model)
NASA	National Aeronautics and Space Administration
NRLMSIS	Naval Research Laboratory Mass Spectrometer and Incoherent Scatter
OPD	optical path difference
PMC	polar mesospheric cloud
POAM	Polar Ozone and Aerosol Measurement
PSC	polar stratospheric cloud
QBO	quasi-biennial oscillation
SABER	Sounding of the Atmosphere using Broadband Emission Radiometry
SAGE	Stratospheric Aerosol and Gas Experiment
SAO	semiannual oscillation
SHS	spatial heterodyne spectroscopy
SME	Solar Mesosphere Explorer
SPW	stationary planetary waves
SSW	sudden stratospheric warming
STRATOGLOW	stratospheric airglow
SWIFT	Stratospheric Wind Interferometer For Transport studies
TIDI	TIMED Doppler Interferometer
TIMED	Thermosphere Ionosphere Mesosphere Energetics and Dynamics (satellite)
TIME-GCM	thermosphere-ionosphere-mesosphere-electrodynamic general circulation model
TIROS	Television Infrared Observation Satellite
TOVS	TIROS Operational Vertical Sounder
UARS	Upper Atmosphere Research Satellite
UKMO	UK Met Office
VER	volume emission rate
VSR	volume scattering rate
WAMDII	Wide-Angle Michelson Doppler Imaging Interferometer
WATS	Wind and Temperature Spectrometer
WINDII	Wind Imaging Interferometer

(OPD), denoted Δ, as a function of off-axis angle outside the interferometer, i, is given by

$$\Delta/2 = n_2 d_2 - n_1 d_1 - \left(\sin^2 i/2\right)\left(d_2/n_2 - d_1/n_1\right) - \left(\sin^4 i/8\right)\left(d_2/{n_2}^3 - d_1/{n_1}^3\right) + \text{higher-orderterms.} \quad (1)$$

By proper choice of d_1, n_1, d_2 and n_2, the term in $\sin^2 i$ can be made equal to zero, making Δ independent of i to the fourth order. This produces a field that is wider than the conventional Michelson interferometer by $n\sqrt{(2R)}$, where R is the resolving power, providing a gain that increases with increasing resolving power, unlike conventional spectroscopic instruments. Ground-based instruments for Doppler temperature measurements have been constructed by *Hilliard and Shepherd* [1966b], *Zwick and Shepherd* [1973], and *Duboin* [1974].

[4] Phase stepping and the use of a "solid" DMI was introduced in a precursor to WINDII called WAMDII, the Wide-Angle Michelson Doppler Imaging Interferometer [*Shepherd et al.*, 1985] intended for wind measurements from the Space Shuttle, but its flight was later canceled. Preliminary ground-based measurements were made with a developmental model [*Wiens et al.*, 1988]. WINDII [*Shepherd et al.*, 1993a] was based on WAMDII but had to meet more limited volume, mass, power, and telemetry requirements.

[5] Doppler wind measurements require stability in the measurement of phase as well as amplitude, but the use of glass for field compensation introduces a high phase sensitivity to any temperature change, which may occur on the ground or in space. However, as first pointed out by *Title and Ramsey* [1980], there is some freedom of choice in both the refractive indices and the lengths of the glasses in the two arms so that it is in principle possible by careful selection to achieve the desired phase stability for wind measurement. This approach was extended by *Thuillier and Shepherd* [1985], leading to a "fully compensated" Michelson interferometer. This compensation was described in terms of five conditions: (1) optical path difference, (2) field widening, (3) chromaticity, (4) thermal compensation, and (5) wavelength-independent thermal compensation. All of these conditions were simultaneously satisfied for WINDII, which meant that it was achromatically field-widened for the desired optical path difference and was thermally compensated for all wavelengths. Such a system has been used for ground-based wind measurements [*Thuillier and Hersé*, 1988; *Thuillier et al.*, 1990, 1996; *Gault et al.*, 1996b; *Fisher et al.*, 2000; *Bhattacharya et al.*, 2004] as well as for WINDII.

[6] The optical layout of the WINDII instrument is shown in Figure 1a. Inputs from the Earth's limb at 45° and 135° from the spacecraft velocity vector are reflected from the "limb pointing mirrors" and combined into a single beam at the "field combiner" prism. The combined beam then passes through a filter wheel which selects the desired airglow emission from atomic oxygen, hydroxyl, or molecular oxygen, after which it enters the "Michelson interferometer." Within the interferometer the phase stepping was accomplished by

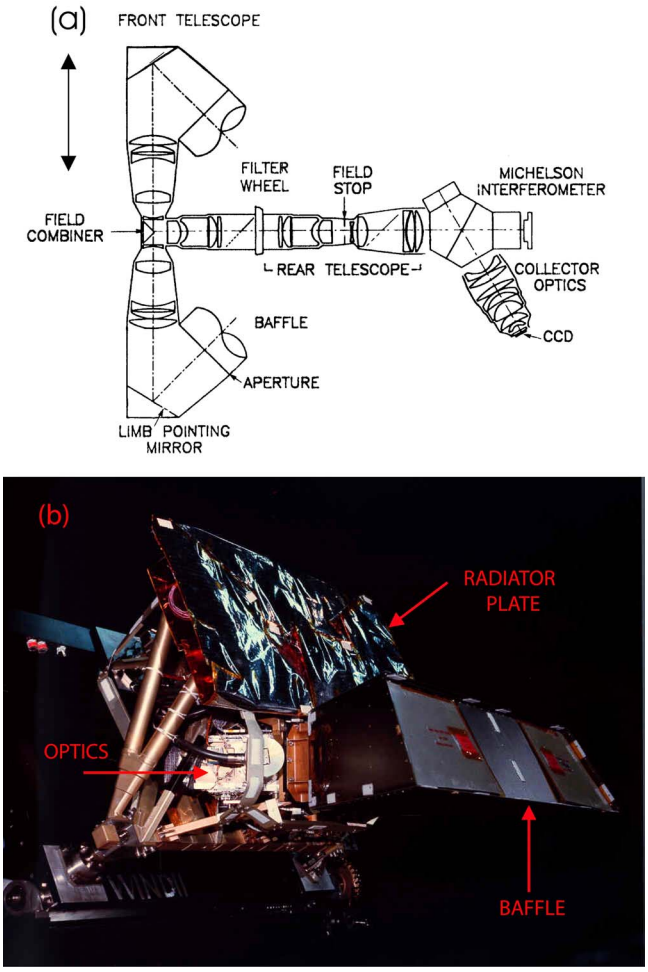

Figure 1. (a) WINDII optical schematic layout; the arrows show the two directions of WINDII motion corresponding to forward and backward UARS flight. (b) WINDII photo showing the baffle, the radiator plate, and the optics which are deep inside the structure.

moving the unattached Michelson mirror shown in Figure 1a (it actually is cemented to the main body with piezoelectric drivers, with the movement controlled by the measurement of capacitance between two spacers) using either four or eight steps over one fringe (360° of phase). The beam emerging from the interferometer forms two side-by-side images on the CCD (charge coupled device) detector, corresponding to the two fields of view. It is the field widening of the interferometer that allows this imaging of the entire altitude range from 80 to 300 km in single images, providing images of the wind.

[7] For the measurement of tides it was necessary to make observations over 24 h of local time, meaning that the airglow had to be measured during both the day and the night. To make the daytime observations possible a 1 m long baffle [*Gault et al.*, 1992] was required to screen the sunlight scattered from the cloud tops. The baffle is indicated but not shown in Figure 1a and is prominent in the photo of Figure 1b, projecting toward the right on the image, with the openings covered. Above the baffle are the radiator plates, needed to cool the CCD detector; these face cold space in the anti-Sun direction. The UARS orbit has an inclination of 57° so that after 36 days the spacecraft is reversed in its flight direction so that the Sun is kept on the "Sun side" of the spacecraft. This maneuver is called a "yaw," and the 36 days is called a "yaw period." The instrument is described in detail by *Shepherd et al.* [1993a].

[8] The airglow emissions observed were the $O(^1S)$ and $O(^1D)$ atomic oxygen lines, the OH (8,3) band $P_1(2)$ and $P_1(3)$ lines (see section 6.2), the $O^+(^2P)$ ionized atomic oxygen line pair at 732 and 733 nm (section 7.3), and the $^PP(7)$ and $^PQ(7)$ lines in the O_2 (0–0) Atmospheric band. The latter pair required an etalon for their spectral separation, which resolved the lines into two rings on the image as described by *Shepherd et al.* [1993a]. The etalon was in fact a solid narrowband interference filter, the first one that the supplier had ever made. It is now a standard product.

[9] The WINDII overall specifications were as follows: mass, 145 kg; volume, 0.85 m^3; power, 60 Watts average; data rate, 2 kilobits s^{-1}. The UARS orientation accuracy was better than 1 arcminute, and its drift rate was 1 arcsecond s^{-1}. This allowed the WINDII observations to be determined to slightly better than 1 km in altitude.

[10] Although the aeronomy community has generally adopted the rayleigh, proposed by *Hunten et al.* [1956] as a photometric unit for the aurora and airglow, confusion still exists about the terminology. The fundamental quantity is the "volume emission rate," the number of photons emitted per second from a unit volume, obtained through an inversion process. What is observed by WINDII is the "column integrated emission rate," the number of photons emitted per second in all directions from a column of unit area along the line of sight. *Hunten et al.* [1956] proposed that this quantity be called the rayleigh, in units of 10^6 photons cm^{-2} (column) s^{-1}, and noted that this is equal to $4\pi B$, where B is brightness in units of 10^6 photons cm^{-2} s^{-1} sr^{-1}. However, the current usage of "brightness" is as a perceived quantity, not a measured one. The word "brightness" has been replaced by "radiance," but one often sees other words such as luminosity or intensity used instead. In this present work only the terms "volume emission rate" and "radiance" are employed. Where "emission rate" stands alone it should be understood as "volume emission rate."

[11] WINDII was based on the concept that a single Gaussian airglow line, with a width determined only by its velocity distribution (temperature) produces at the output of a Michelson interferometer a cosinusoidal signal within a Gaussian envelope that is the Fourier transform of the spectral line. The wind is measured simply from the phase of the signal, and the temperature is determined from the line visibility, V, where I_{max} is the maximum signal at the peak of the cosinusoid and I_{min} is the minimum value in its valley:

$$V = (I_{max} - I_{min})/(I_{max} + I_{min}). \quad (2)$$

Different aspects of the retrieval of volume emission rate, wind, and Doppler temperature profiles from the WINDII airglow emission measurements were described by *Shepherd et al.* [1993a], *Gault et al.* [1996a], and *Lathuillère et al.*

[2002], with details provided by *Rochon* [1999]. The WINDII Level 1 processing involves data calibration and the subtraction of the background continuum from the phase stepped measurement images. The Level 1 data were organized into six columns across the image, each 25 km wide, but these were combined into single profiles in the Level 2 processing. The first stage of the Level 2 processing, which includes the zero wind phase removal, consists of reducing the phase-stepped images to profiles in tangent height of the three Fourier coefficients, J_1, J_2, and J_3, of the fringe interferograms. These Fourier coefficients, also referred to as the apparent quantities, are related to any point i along a fringe interferogram I for a given tangent height through the equation:

$$\begin{aligned} I_i &= J_1[1 + UV\cos(\Phi_i + \varphi)] \\ &= J_1 + J_2 U\cos\Phi_i - J_3 U\sin\Phi_i, \end{aligned} \tag{3}$$

where U and V are the instrumental and line-of-sight atmospheric line visibilities, Φ_i is the known phase contribution, and φ is the line-of-sight atmospheric wind phase, with

$$\begin{aligned} J_2 &= J_1 V\cos\varphi \\ J_3 &= J_1 V\sin\varphi. \end{aligned} \tag{4}$$

This is followed by inversions of the Fourier coefficients to profiles in altitude using a two-iteration Twomey-Tikhonov approach. The first iteration provides an initial solution from which the layer-by-layer change can be compared with the local and unconstrained random error level. At the second iteration, this information is applied to avoid or reduce overconstraining in regions where this layer-by-layer change exceeds the random error level. The constrained solution equations for the three apparent quantity vectors have the general form

$$\hat{x} = \left(\mathbf{K}^T\mathbf{S}^{-1}\mathbf{K} + \gamma\mathbf{C}^T\mathbf{C}\right)^{-1}\mathbf{K}^T\mathbf{S}^{-1}\boldsymbol{J}, \tag{5}$$

where $\hat{x}$ is the solution profile, $\mathbf{K}$ is the data kernel matrix reflecting the line-of-sight integration assuming locally spherical atmospheric uniformity, $\mathbf{S}$ is the diagonal error covariance matrix for the apparent quantity vector $\mathbf{J}$, γ is a preselected weighting factor, and $\mathbf{C}$ is a weighted second-order difference matrix [*Twomey*, 1963; *Tikhonov*, 1962; *Phillips*, 1962]. The application details are provided by *Rochon* [1999]. The inversion of J_1 directly gives the airglow line volume emission rate profile. The profiles in altitude of the atmospheric wind phase, φ, and line visibility, V, the equivalent of the line-of-sight averages, φ and V, in equation (4), are extracted from the solutions of the other inversions. The Doppler wind velocities, w, are obtained from the wind phases using

$$\varphi = \frac{2\pi}{\lambda_0} D\frac{w}{c}, \tag{6}$$

where λ_0 is the emission line wavelength for a volume at rest, c is the speed of light, and D is the "effective" optical path difference from *Thuillier and Hersé* [1991]. The zonal and meridional wind components are obtained from the Doppler wind profiles of the two nearly orthogonal look directions. For the case of a Gaussian line shape, the relationship between the visibility and the temperature is

$$V = \exp\left(-QTD^2\right), \tag{7}$$

where $Q = 3.033 \times 10^{-39}\ \mathrm{K}^{-1}\ \mathrm{kg} \times \lambda_0^{-2}\mathrm{m}^{-1}$, and m is the atomic mass of the emitting species. The difference between the resulting temperature, referred as the Doppler temperature, and the actual temperature, depends on the applicability of the Gaussian line shape model for the given atmospheric state (section 6.1).

[12] The prelaunch characterization of WINDII was described by *Hersom and Shepherd* [1995], while *Gault et al.* [1996a] studied the changes in WINDII characteristics over the first 2 years of operation. The optical path difference changed gradually by about two wavelengths over this period before settling down to a stable value. The reason for this is unknown but may be a result of cement shrinkage. Since it was routinely tracked by the onboard calibration lamps, this did not present a problem. A detailed description of the WINDII calibration system, as well as an evaluation of the on-instrument orbit performance over the first 5 years of the mission, was presented by *Thuillier et al.* [1998].

[13] Not shown in equation (3) is a term representing the background, which must be subtracted from the data image and for the O(^{1}S) and O(^{1}D) emissions is measured with Filter 1 at 553 nm. A background image is recorded before each wind measurement sequence while dark level and phase calibration images are acquired roughly every 20 min. An instrument visibility calibration is taken weekly, along with responsivity calibrations for each filter. The WINDII frame of reference is checked against that of the spacecraft on a monthly basis, using star images recorded by WINDII at one by one pixel resolution. This ensured an accuracy of airglow altitude determination to a little better than 1 km.

[14] Because the WINDII observations were the first for a DMI in orbit, it was essential that the wind observations be validated. The objective of the validation was to establish the intrinsic precision of the measurements of wind (especially zero wind) and temperature made by WINDII, primarily by making observations with other instruments that observe similar or approximate common volumes. The uncertainties in establishing comparisons of precision are only as good as the established precision of the instruments being compared as well as the geophysical variability in the atmosphere due to waves (planetary, tides, and gravity waves) and instabilities at spatial and temporal scales inherent in the atmosphere. Thus, this became a community effort.

[15] Some cross-validation was available on orbit because of the High Resolution Doppler Imager (HRDI), a triple-etalon Fabry-Pérot interferometer [*Hays et al.*, 1993]. This instrument measured winds from lines of the O_2 Atmospheric band (hereinafter denoted as O_2 Atm) emission in the region where there was airglow, about 70–120 km [*Burrage et al.*, 1994], and winds at lower altitudes from the same band in absorption observed in scattered sunlight through the stratosphere. In the region of overlap, HRDI and

WINDII winds could be compared; it was a rigorous comparison because HRDI made its spectral observations simultaneously and its spatial observations (altitude) sequentially, just the opposite of WINDII. As well, the two instruments observed different airglow emissions with different vertical distributions. The first comparisons [*Burrage et al.*, 1996] showed that HRDI agreed well with some ground-based radars, but not with others, and that it agreed with rocket wind measurements and with the WINDII winds. *McLandress et al.* [1996b] also showed excellent agreement between HRDI and WINDII, which further established confidence in the UARS winds. *Gault et al.* [1996a] found good agreement of WINDII with ground-based optical wind measurements, including the Michelson Interferometer for Coordinated Auroral Doppler Observations (MICADO) [*Thuillier et al.*, 1990] and ground-based Fabry-Pérot instruments, but differences with some MF (medium frequency) and MR (meteor radar) radars were found. Because WINDII could measure winds in the thermosphere, comparisons with the European Incoherent Scatter (EISCAT) radar at 170 km were possible [*Gault et al.*, 1996a] and these agreed well. *Duboin* [1997] compared WINDII thermospheric winds at midlatitudes (250–260 km) with winds from the incoherent scatter radar at Saint-Santin and found good agreement. *Burrage et al.* [1997] made a later comparison of HRDI and WINDII and concluded that absolute wind biases may exist for both instruments, -4 m s^{-1} for WINDII and +2 m s^{-1} for HRDI.

[16] The discrepancy between WINDII winds and MF radars has taken a long time to become fully resolved. As late as 2006, *Portnyagin* [2006] was finding agreement between radars and HRDI winds but disagreement between HRDI and WINDII and between MF and MR radars. With a perspective of 20 years it seems that these differences arose from limitations in some of the MF radars at that time or in the way the comparative data were sampled. For example, *Portnyagin* [2006] did not use WINDII measured values but the empirical model derived from the data by *Wang et al.* [1997] for the years 1992–1993, while the radar data came from 1990 to 2001. In comparing monthly averages one has to keep in mind that different data sets will not sample all of the same days in each month, nor will the same local times be sampled. There are many reasons as to why discrepancies can arise, and it is not possible to unravel all of these here. However, *Jacobi et al.* [2009] made a careful comparison of MF and MR radars over 1 year and found reasonable agreement at 82 km but increasing differences with increasing altitude, reaching a factor of 2. To add further complexity, the difference was greater in winter than in summer; this was attributed to the influence of gravity waves. In a further study, *Hoffmann et al.* [2010] employed MF radar data from 70 to 83 km altitude and MR data from 82 to 95 km. *Ward et al.* [2010] compared radar wind tidal amplitudes with those from the TIMED Doppler Interferometer (TIDI) instrument on the Thermosphere Ionosphere Mesosphere Energetics and Dynamics (TIMED) satellite as well as with the Canadian Middle Atmospheric Model (CMAM) model and found good agreement. It seems that this optical/radar discrepancy has been resolved through an evolution of radar improvements and a better recognition of the limitations of the different methods.

[17] Further closure has been brought about by the definitive Horizontal Wind Model 2007 (HWM07) as presented by *Drob et al.* [2008], covering the altitude range 0–500 km and 50 years of data. WINDII and HRDI each contributed about 30 million measurements, while 12 ground-based Fabry-Pérot interferometers and one lidar provided about 100,000 measurements each and three MF radars contributed about one million measurements each. The good agreement of the WINDII observations with the model is expected but also satisfying, as it was not the sole contributor. What it means is that a researcher wishing to use WINDII data, but not finding it at the desired location or time, may simply make use of the accessible HWM07 model. The extension to geomagnetically disturbed conditions is provided by the companion model DWM07; the Disturbance Wind Model by *Emmert et al.* [2008] provides the thermospheric winds as a function of Kp. WINDII winds are compared with ground-based Fabry-Pérot instruments and with the WATS (Wind and Temperature Spectrometer) instrument on Dynamics Explorer, all with good agreement.

[18] The Dynamics Explorer 2 Fabry-Pérot Interferometer was the first to measure winds remotely from space [*Killeen et al.*, 1982]. It employed fused silica plates separated with Zerodur spacers, held in an invar mounting that was insensitive to temperature change. Spectral scanning was accomplished with a multianode focal plane detector, using primarily the O(^{1}D) emission for thermospheric measurements. It is remarkable that there has been only one wind instrument launched since the UARS mission and that is the TIDI instrument launched on the TIMED spacecraft in December 2001. Described by *Killeen et al.* [2006], the concept is based on experience from HRDI; both were designed and built at the University of Michigan. TIDI is a smaller instrument than HRDI, with only one etalon and a CCD detector replacing the HRDI multianode photomultiplier. It features the CLIO (circle to line interferometer optical system) [*Hays*, 1990], a conical reflector which converts the circular Fabry-Pérot rings to straight lines. An ingenious fiber-optic coupler interfaces four input telescopes to these Fabry-Pérot straight-line fringes. Although there have been problems with light leakage causing increased background signal and frosting on mirror surfaces, TIDI has achieved essentially continuous operation from 2002 until the present time, which has allowed a detailed description of nonmigrating tides [*Oberheide et al.*, 2007].

[19] Section 2 describes the primary measurements made by WINDII, the mean winds and migrating tides. This is followed by a description of the influence of these dynamics on species concentrations through airglow observations in section 3. Sections 4 and 5 cover the observations of planetary waves and gravity waves, respectively, as well as direct observations of small-scale structures in airglow. Temperature measurements are described in section 6, and section 7 contains descriptions of what are called "spin-off" science: science studies that were not envisaged in the

TABLE 2. Summary of WINDII Observations[a]

Filter Number	Emission	Total Days	Year						
			1991	1992	1993	1994	1995	1996	1997
1	bg-O(^{1}S)	1013	33	219	222	170	166	139	64
2	O(^{1}S)	764	16	167	172	113	129	130	37
3	O(^{1}D)	191	9	44	51	59	22	5	1
4	OH/O+	427	22	122	123	90	42	4	24
5	bg-OH	562	27	137	156	103	67	28	44
6	OH	303	22	84	81	58	30	4	24
7	O2	600	14	194	215	82	30	20	45

[a]The abbreviation "bg" stands for "background." Numbers are the number of days in each year for which WINDII made observations with the indicated filter; WINDII often observed with more than one filter on a given day, so the Total Days can be more than the number of days in a year.

design of the mission. These include airglow studies, nitric oxide observations, ionized atomic oxygen, polar mesospheric clouds, and solar flares. Section 8 describes the thermospheric dynamics observed, including the solar and geomagnetic influences and nonmigrating tides. A summary of what WINDII accomplished is presented in section 9, and what was not accomplished is given in section 10. Section 11 describes the future prospects for wind measurements, and a concluding summary in section 12 completes the story.

[20] To set the stage for the data presentation sections, Table 2 provides a summary of the analyzed data coverage from the mission to date. The data are organized by filter number, and the emission corresponding to each number is listed. Then for each year of data acquisition the number of days during that year that each filter was employed is given. On many days more than one filter was used, so the total numbers add up to more than the number of days in the year.

2. WINDII OBSERVATIONS OF MIGRATING TIDES AND MEAN WINDS

[21] Based on existing wind measurements such as those summarized by *Groves* [1980], the WINDII team members were of the opinion prior to launch that WINDII would not be able to accurately define the tides. The primary reason for this belief was that to determine the diurnal tide, it would be necessary to make measurements over 36 days in order to cover 24 h of local time. Given the variability of tidal amplitudes between different ground stations and the observed day-to-day variations, it seemed impossible that a coherent tide could be extracted over the course of 36 days. From the very first results for the meridional wind component it turned out that the diurnal tide at the equator was the most dominant feature of the WINDII observations [*McLandress et al.*, 1994]. There were at least three reasons for this unexpected result. The first was that through zonal averaging the variability seen at single ground-based stations was largely eliminated. The second was that with a global view, the diurnal tide at the equator stood out dramatically against the smaller tidal amplitudes at other latitudes—it could be seen clearly in a single pass of UARS over the equator. The third factor was that the amplitude of the tide was much larger than expected. *McLandress et al.* [1996a] presented the first detailed analysis of the diurnal and semidiurnal tidal components and showed that there was a semiannual variation in the amplitude of the diurnal tide, peaking at the equinoxes. *Yudin et al.* [1997, 1998] simulated the tides by tuning a mechanistic model to the UARS winds results. *McLandress* [2002] later explained the semiannual variation of the diurnal tide by using a linear mechanistic tidal model which was able to reproduce all of the important tidal features, in particular, the semiannual amplitude variation in the lower thermosphere at low latitudes. From this analysis the effects of both heating and mean winds were found to be responsible for this seasonal variation. An example of the meridional wind measured at 20°N as a function of altitude and local time is shown in Figure 2; to give the desired local time coverage, the data acquired included April and March from 1992 and 1993. The value of being able to measure the wind over 24 h of local time is clearly evident as the upward propagating tide is clearly seen as tilted wavefronts with a period of 24 h; the units of wind are meters per second, and so the meridional wind in the wavefronts reverses from 60 m s^{-1} northward (positive) and 60 m s^{-1} southward. The tide dissipates at about 120 km, and above that an in situ tide is seen. Although the night airglow exists as a thin layer (the thickness is 20 km for the nighttime local times) the vertical resolution is sufficient to see the propagation of the tide through the layer. It is also instructive to note that the measurements from different local times came from different days; it was the stability of the UARS spacecraft that

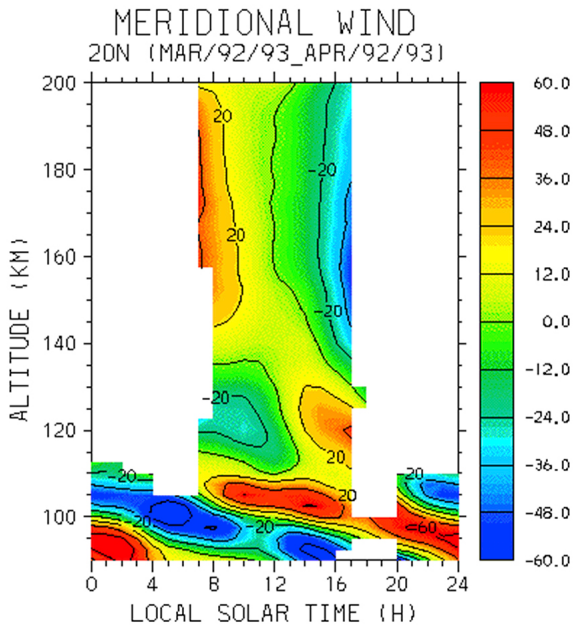

Figure 2. The meridional wind at 20°N for March/April 1992 and 1993 as a function of altitude and 24 h of local time. During the daytime hours the measurements extend to 200 km; during the night they are available in only the thin nightglow layer. The upward tilted migrating diurnal tide is dominantly evident, breaking at about 120 km. Above this the tide is excited in situ. On the color scale "60" indicates 60 m s^{-1} northward. Courtesy of Charles McLandress.

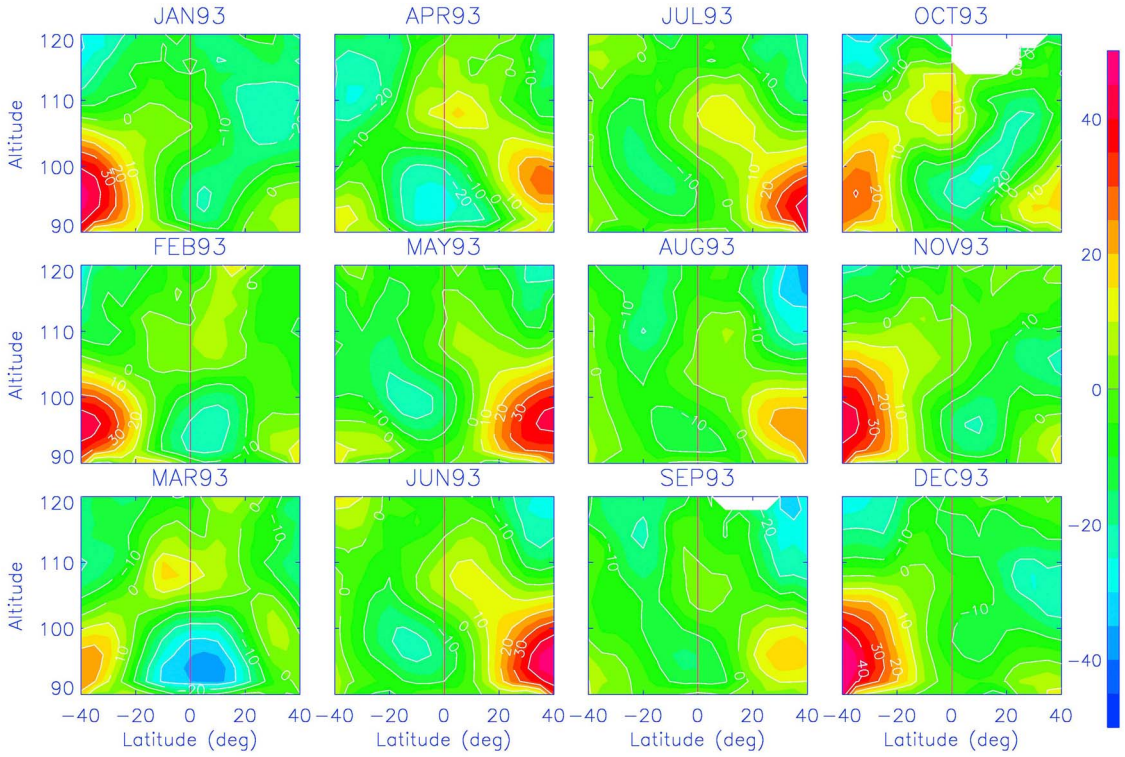

Figure 3. WINDII zonal mean zonal wind in meters per second (positive eastward) as a function of altitude and latitude month by month during 1993. Courtesy of Shengpan Zhang.

ensured consistency between measurement altitudes taken on widely separated days.

[22] An example of the variation of the zonally averaged mean zonal wind as a function of altitude and latitude over the course of the year is shown in Figure 3 for 1993. The primary feature is a prominent eastward wind jet at an altitude of about 95 km in the summer hemisphere at about 40° latitude, with a velocity of 40 m s^{-1}, seen clearly at −40° in January and +40° in June. A secondary feature is a westward wind located at the equator that maximizes in March at 40 m s^{-1} but is present for the rest of the year at about 10 m s^{-1}. The annual variation of the zonally averaged amplitude of the meridional component of the diurnal tide is shown in Figure 4 as a function of altitude and latitude month by month in 1993. The tidal amplitude shows sharply defined maxima near 20°N and 20°S latitude, extending from about 90–105 km, persisting over the course of the year but strongly maximizing at about 80 m s^{-1} in March. The amplitude of the zonally averaged zonal component of the semidiurnal tide is shown in Figure 5. The maximum amplitudes are confined to midlatitudes throughout the year, near 40°, but maximizing in September at an altitude of 105 km at 50 m s^{-1} and extending to the equator.

[23] The most recent results have been presented by *Zhang and Shepherd* [2005b], *McLandress and Zhang* [2007], and by *Zhang et al.* [2007]; the following conclusions are taken from the latter publication and expand on what has just been presented. With respect to the zonally averaged mean zonal wind, (1) the zonally averaged mean zonal winds at midlatitudes below 110 km are mostly eastward and have an annual variation with a maximum of 50 m s^{-1} in summer, while above 110 km westward winds are dominant, and (2) in the tropical region below 105 km the zonally averaged mean zonal winds are mostly westward and have a semiannual variation with maxima of 20–40 m s^{-1} at the equinoxes, while above 105 km there is an eastward flow which is prominent in March and April. The zonally averaged mean meridional winds are significantly weaker than the zonal component. In solstice months, there is a summer-to-winter flow of about 10 m s^{-1} below 100 km, which is driven primarily by forcing from small-scale gravity waves; this is the flow that keeps the winter mesopause warm and the summer mesopause cold. Above 100 km there is a winter-to-summer flow in some solstitial months. In the equinoctial months the zonally averaged mean meridional wind is characterized by a cell-like pattern at low latitudes with opposite wind directions on both sides of the equator. The size and magnitude of the cells vary from month to month. The authors consider these to be the first-ever observations of this structure, which is believed to arise from momentum deposition by the vertically propagating migrating diurnal tide.

[24] Concerning the migrating diurnal tide, *Zhang et al.* [2007] found two distinct migrating diurnal tides with comparable magnitudes in the WINDII winds; one is the well-documented upward propagating tide and the other is the less-studied evanescent tide. The propagating tide is dominant in the subtropical regions below about 105 km and has a semiannual variation with a maximum in March/April and a much weaker maximum in September/October. The

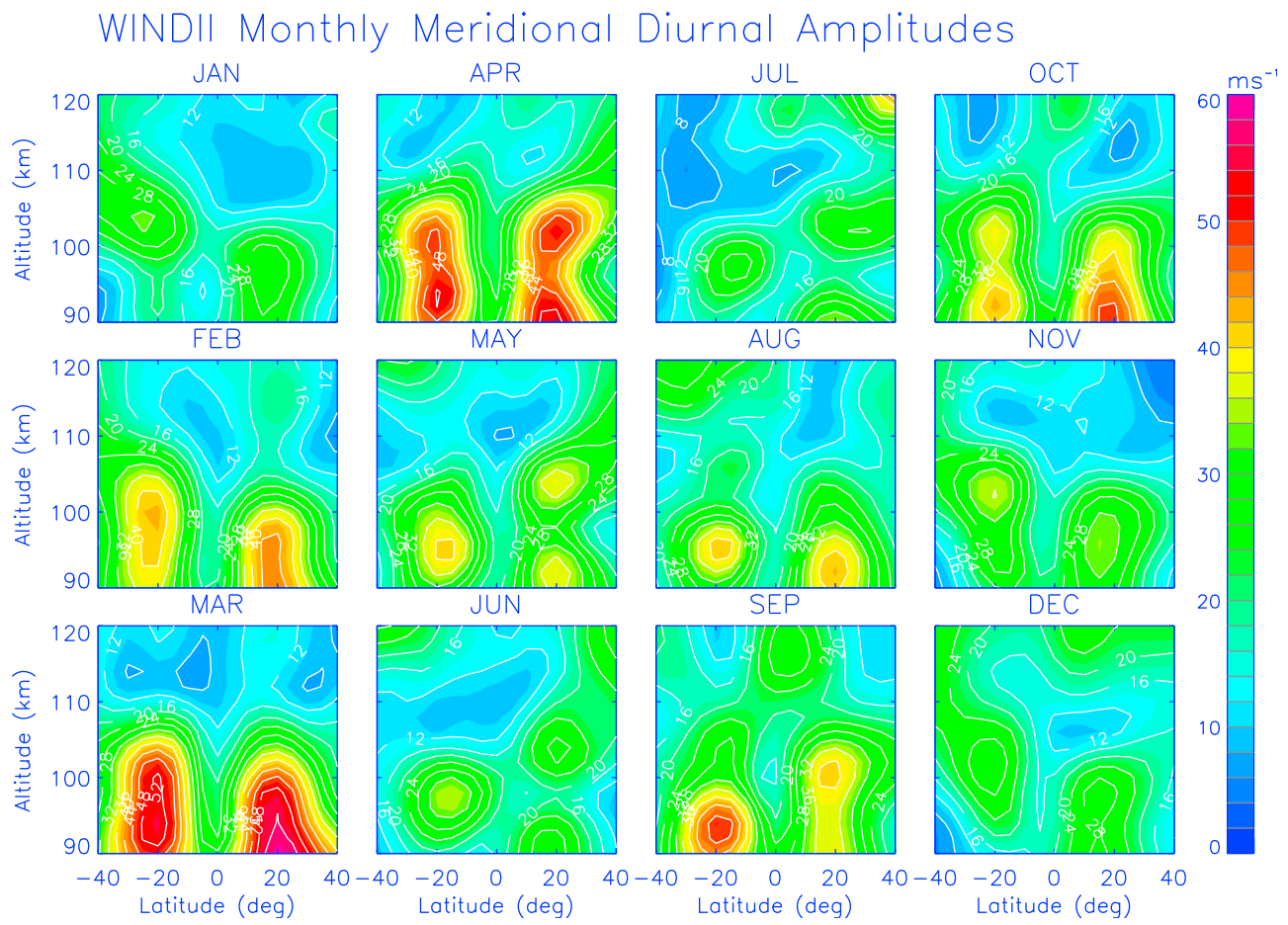

Figure 4. Amplitude of the WINDII zonally averaged meridional component of the migrating diurnal tide as a function of altitude and latitude month by month for 1993. Courtesy of Shengpan Zhang.

evanescent tide is dominant mainly at latitudes above 20° and altitudes above 105 km and has an annual variation with its maximum in summer. The coupling of the two produces the double-peaked structure observed in the diurnal amplitude vertical profile. The meridional component of the diurnal tide at the equator below 105 km in June is also evanescent.

[25] Regarding the migrating semidiurnal tides, *Zhang et al.* [2007] present the first global (i.e., 40°S–40°N) structure of the monthly semidiurnal tidal amplitude from 90 to 120 km. The semidiurnal tide is generally weaker than the diurnal tide, and its seasonal and latitudinal variation is very different from that of the diurnal tide. Both the zonal and meridional components of the migrating semidiurnal tidal winds are stronger in April through September than in October through March; that is, in the Southern Hemisphere semidiurnal winds are stronger in winter than in summer, whereas in the Northern Hemisphere, it is the reverse. The amplitude structures of the zonal and meridional components in April through September are distinct, in that the maximum zonal amplitude is at 30°–40°, whereas the maximum meridional amplitude is at 35°S, the equator, and somewhere poleward of 40°N [see *Zhang et al.*, 2007, Figure 14]. The complicated phase relationships and different vertical wavelengths of the semidiurnal tides indicate the existence of different symmetric and antisymmetric modes in the mesosphere and lower thermosphere (MLT) region. The WINDII wind climatology as presented by S.-P. Zhang may be further viewed at http://uars.gsfc.nasa.gov/Analysis/UARS/windii_wind_model/windii_model.html or by simply going to the UARS homepage and selecting "UARS Reference Atmosphere Project."

[26] Examination of nonmigrating tides in a combined WINDII/HRDI data set was undertaken by *Forbes et al.* [2003]. In this work, signatures associated with the eastward wave number 3, stationary wave number 0, and westward wave number 2 diurnal tides were identified and their seasonal variations determined. It is interesting to note that the tidal amplitudes identified in this study are one half of those diagnosed by *Oberheide et al.* [2006], although the phases are remarkably similar. Further work is needed to investigate the nature of these differences.

3. MESOSPHERE LOWER THERMOSPHERE DYNAMICS THROUGH AIRGLOW OBSERVATIONS

[27] Although the WINDII was included as part of the UARS mission primarily for its wind measuring capabilities, its ability to simultaneously measure airglow radiance proved almost as important and provided another valuable

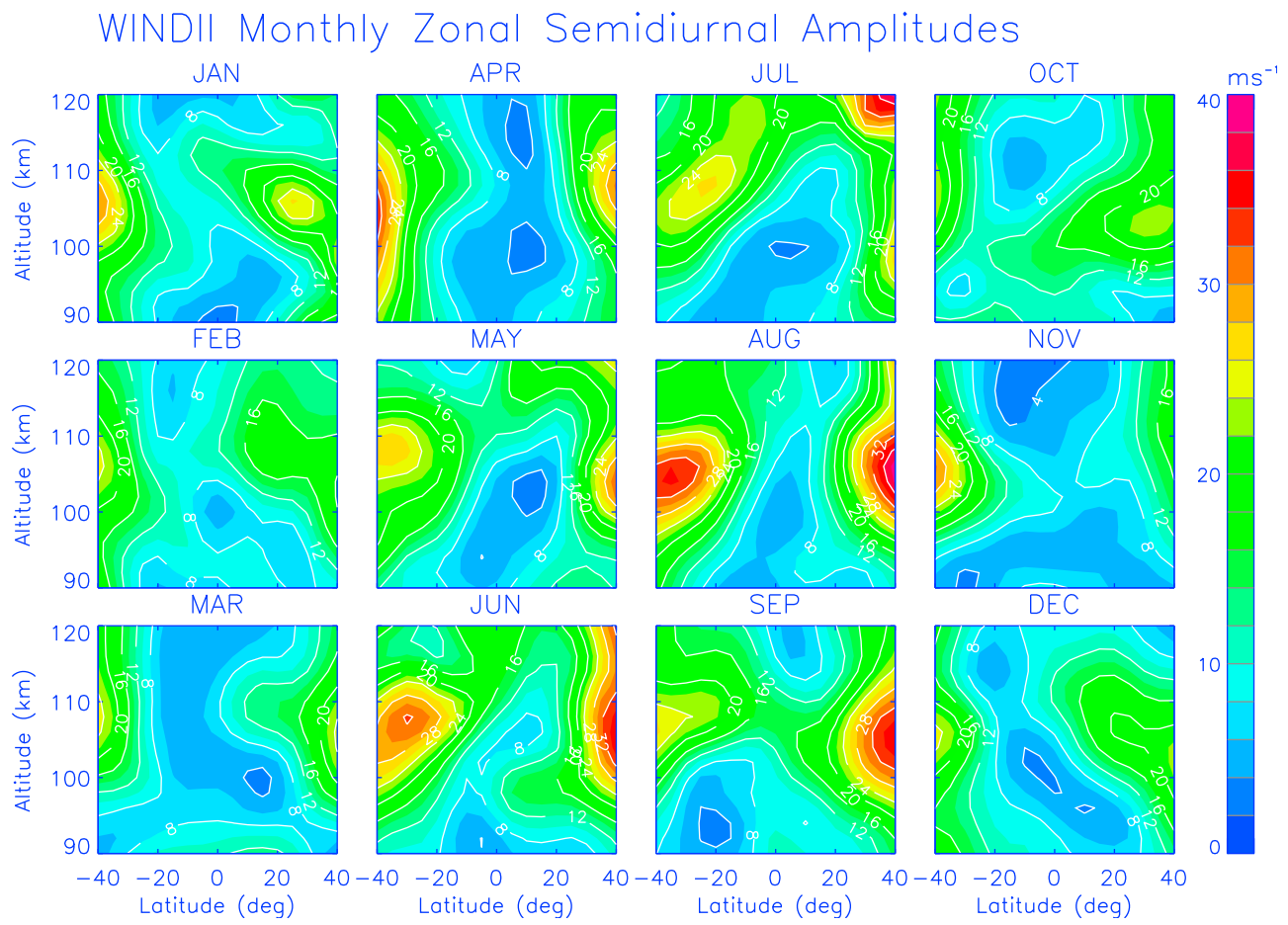

Figure 5. Amplitude of the WINDII zonally averaged zonal component of the migrating semidiurnal tide as a function of altitude and latitude month by month for 1993. Courtesy of Shengpan Zhang.

means to observe dynamical signatures in the mesosphere and thermosphere. Attention was concentrated on the nightglow emissions which included the O(^{1}S) atomic oxygen emission, the ^{P}P(7) and ^{P}Q(7) emissions in the O_2(0–0) Atmospheric band, and the OH P_1(3) line in the (8–3) Meinel band. Significant longitudinal variability in the airglow observations was immediately obvious in the first WINDII observations [*Shepherd et al.*, 1993b]. Agreement on how to interpret this variability, however, took the better part of a decade to develop. The reason for this slow development was that at the time of the launch of UARS (1991) there were several different threads of investigation relevant to the interpretation of airglow signatures which needed to mature.

[28] 1. Uncertainties in the chemistry associated with the nightglow remained, although the work associated with the ETON (Energy Transfer in Oxygen Nightglow) rocket campaign published in the mid-1980s [*Greer et al.*, 1986; *McDade et al.*, 1986a, 1986b, 1987] had done much to resolve the main questions.

[29] 2. The form of the expected profile of atomic oxygen in the mesopause region was uncertain. Eddy diffusion was considered the main process transporting atomic oxygen down from its source region in the lower thermosphere. As a result, its vertical profile was expected to be smooth and stable over time. Observed variability was ascribed to instrumental issues, and as late as 1988 a session at the American Geophysical Union (AGU) was held to determine what the atomic oxygen profile in the MLT region was (see *Llewellyn* [1988] and the papers in the associated special issue).

[30] 3. The identification of the dynamical processes underlying the eddy diffusion necessary for the observed mesospheric temperature and constituent profiles and energy balance was being developed. Observations by *Cogger et al.* [1981] of equinoctial maxima at midlatitudes in green line nightglow radiance were thought to be consistent with equinoctial reductions in the mixing associated with gravity wave breaking [*Garcia and Solomon*, 1985].

[31] 4. The systematic filtering of tidal phenomena associated with the orbit parameters of satellites had not yet been worked out.

[32] Striking indications of strong large-scale variations in the oxygen nightglow were first published by *Shepherd et al.* [1993b] where significant longitudinal variability (a variation of a factor of 10 between the minimum and maximum height integrated emission rates) was noted. Given the prevailing thinking at the time that the eddy diffusion would provide a smooth and uniform distribution of atomic oxygen, these results were striking. The following year, *Ward et al.* [1994] presented preliminary results

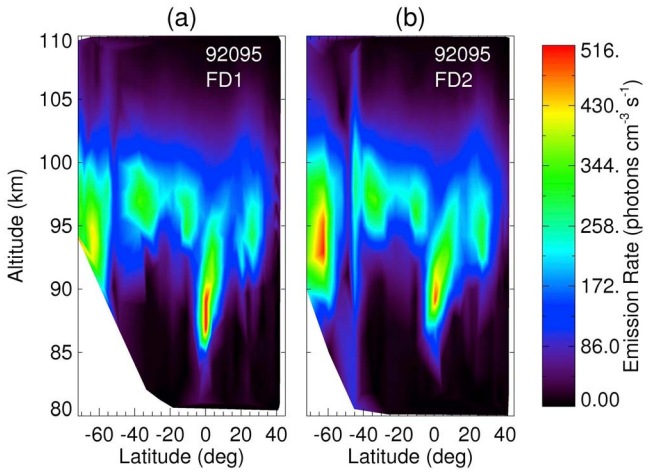

Figure 6. O(^{1}S) volume emission rate as a function of latitude and altitude for a single orbit across the equator on 4 April 1992, as seen by the two fields of view ((a) FD1 and (b) FD2) of WINDII during the time of year of maximum amplitude in the diurnal tide. The effect on the emission rate at the equator is strongly evident and is almost the same for the two orthogonal fields of view, confirming the validity of the inversions.

which showed that the strength of the emission rate increased as the height of the emission peak decreased and that the temperature (determined from the observed visibility) at the peak was highest when the emission peak was lowest. This behavior was noted to be consistent with vertical quasi-adiabatic motions with the oxygen mixing ratio conserved. While this observation was correct, the associated dynamics still needed to be worked out in full. *Zhang and Shepherd* [2008] studied one case of extreme longitudinal disturbance of wave number 1 in both winds and emission rate, with winds reaching 120 m s^{-1} in the MLT region.

[33] During the next few years, some aspects of the spatial and temporal form of the nightglow variability were clarified. The UARS orbit precesses slowly in local time so that over a yaw period, all local times are sampled at each latitude. By zonally averaging the airglow observations and ordering them in local time, it became clear that the airglow emission rate variation could be understood as a local time–dependent phenomenon. During the same period, work on the migrating tidal signatures in the wind data was progressing [*McLandress et al.*, 1996a, 1996b]. Papers with increasing sophistication both in the analysis of the observations and in comparisons with models of varying complexity clarified the local time behavior of the nightglow and linked this behavior to the migrating diurnal tide [*Shepherd et al.*, 1995, 1998; *McDade*, 1998; *Yudin et al.*, 1998; *Zhang and Shepherd*, 1999, *Zhang et al.*, 1998, 2001]. Figure 6 shows a previously unpublished plot of emission rate versus latitude across the equator acquired on 4 April 1992 (day 92095) as presented to a UARS Science Team Meeting in Aix-en-Provence in 1992, where it was pronounced by some as "impossible." There was suspicion that with such detailed structures the assumption of horizontal homogeneity built into the inversion algorithm might break down. Figure 6 therefore contains two plots, one from each field of view, confirming that the inverted orthogonal views of the same atmospheric region give almost the same result. Now, with the passage of time, the enormous influence of dynamics on airglow has become accepted by the community. This image was acquired at the March equinox, at which the amplitude of the diurnal tide has its maximum, as described earlier. Similar effects were later found on the altitude of peak emission of hydroxyl airglow by *Winick et al.* [2009] from SABER (Sounding of the Atmosphere using Broadband Emission Radiometry) data.

[34] As illustrated in Figure 7, taken from *Zhang and Shepherd* [1999], the main features of this modulation of the O(^{1}S) emission consisted of midlatitude maxima and equatorial minima with the peak height and emission rate at each latitude varying with local time. At midlatitudes the peak height decreased with increasing local time and the emission rate increased, whereas for the equatorial emission the opposite was true. For the hydroxyl emission an equatorial maximum is observed in the early evening. This feature diminishes in strength and disappears by morning, at which time midlatitude maxima make an appearance. For solstice conditions, the features are weaker and less symmetric about the equator. The emission rate exhibits a semiannual variation with maxima during the equinoxes, although the Northern Hemisphere spring equinoctial maximum is generally larger than that in the fall [*G. G. Shepherd et al.*, 2004b]. Similar local time variations were reported by *Yee et al.* [1997] based on analyses of HRDI observations with the O_2 Atm emissions having a local time dependence midway between the OH and O(^{1}S) behavior described above, with an equatorial maximum present until local midnight and midlatitude maxima appearing after midnight.

[35] In retrospect, the identification of the mechanism responsible for the airglow variability and its relationship to the diurnal tide should have been easier to determine than it was. Work by *Hines and Tarasick* [1987], using a Lagrangian perspective to interpret variations in airglow, had been published and included consideration of vertical displacements as well as temperature and density effects. Work by *Ehhalt et al.* [1983] had shown that vertical motion was one of the main processes responsible for temporal variability in ozone in the stratosphere. Recognition that the same processes were responsible for the observed tidal variability was delayed because of the variation in local time dependence exhibited by the different emissions, the limited local time coverage, and the complexity of the dependence of the chemistry on temperature and density. All the emission rates have a cubic dependence on density and involve reaction coefficients with a dependence on temperature.

[36] Early papers on the dynamical influence on airglow variability often neglected to include the effect of vertical advection on the airglow emission rate and consequently obtained variations which were out of phase with the observed variability. Identification of the correct process was developed by including vertical advection, appropriate thermodynamic relationships associated with adiabatic

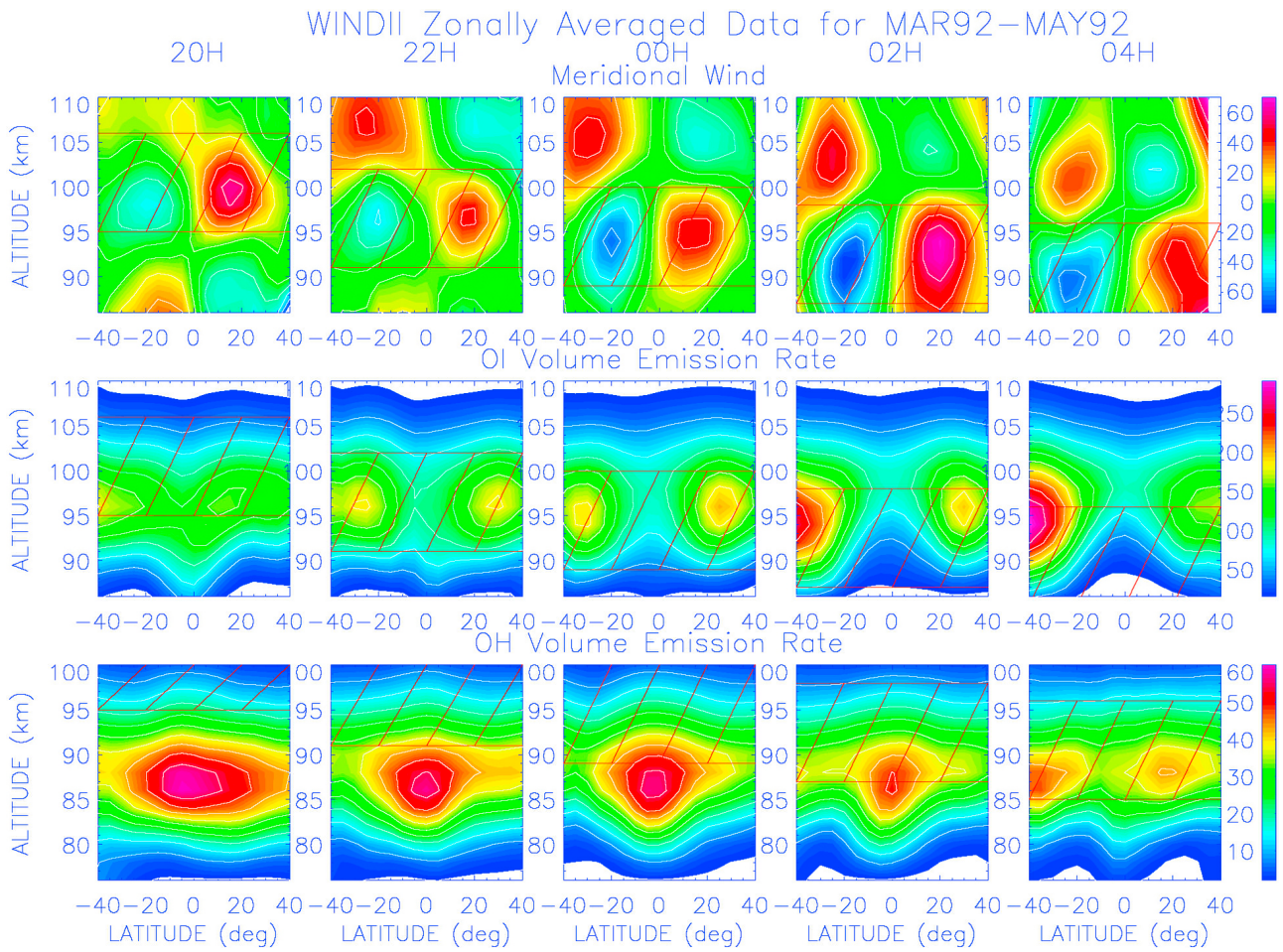

Figure 7. WINDII observations of the zonally averaged latitudinal and vertical distributions at 20:00, 22:00, 0:00, 2:00, and 4:00 LT of the meridional wind (in meters per second); the O(^{1}S) volume emission rate; and the OH volume emission rate of the $P_1(3)$ line of the (8,3) Meinel band (in photons cm^{-3} s^{-1}) for March through May 1992. The hatched regions are those of the diverging meridional wind. From *Zhang and Shepherd* [1999].

motion along with the airglow chemistry [*Ward*, 1998, 1999]. The mechanism involved is the same as that used by *Hines and Tarasick* [1987] except that tidal motions are large enough that linearization of the equations is no longer valid.

[37] For adiabatic parcel displacement in the vertical and a stable atmospheric temperature profile, parcel densities are less (greater) and parcel temperature is greater (less) than the surroundings for displacements below (above) the parcel equilibrium position. From the emission chemistry, the emission rate has a cubic dependence on density and through the rate constant decreases with increasing temperature. If the volume mixing ratio profile of atomic oxygen were constant with height, this would imply that the emission rate relative to its surroundings would decrease as the parcel is lowered and increase as it is lifted since its density (and hence constituent concentrations) would respectively be less than or greater than its surroundings. However, the oxygen mixing ratio increases with height sufficiently rapidly that downward displacements bring ample oxygen rich air with them so that this density/temperature/emission rate correlation is canceled and the opposite correlation occurs (i.e., downward displacements generally cause enhancements in the airglow). Figure 8, taken from *Ward* [1999], illustrates this dependence for a diurnal tide of average amplitude, with latitude structure given by the (1,1) Hough mode (Hough functions are eigenfunctions that are solutions to Laplaces's Tidal Equation for a windless and uniform temperature atmosphere [*Chapman and Lindzen*, 1970] which provide guidance for the general latitudinal structure for global modes even when the atmosphere deviates significantly from these idealized conditions), the accepted airglow chemistry [*McDade*, 1997], and vertical wavelength and phase appropriate to the equinox conditions for the hydroxyl emission shown in Figure 7. As is clear, the local time behavior of the WINDII observations is modeled surprisingly well for both the O(^{1}S) and hydroxyl emissions. The Lagrangian model developed by Ward has general application to adiabatic vertical displacements as long as the lifetimes of the species involved are long relative to the dynamical motion and the species can be considered to be horizontally stratified.

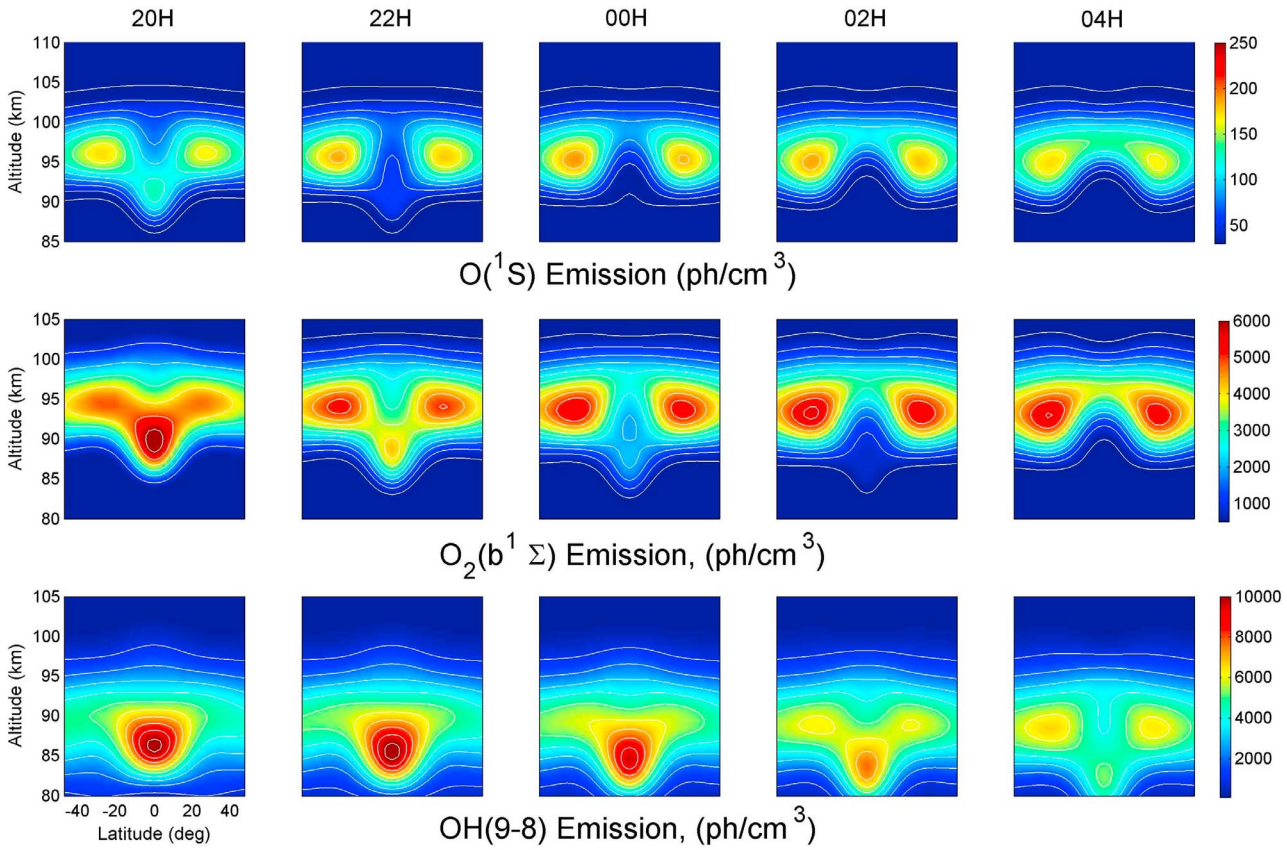

Figure 8. Model results of O(^{1}S), O_2($b^1\Sigma$), and OH (9–8) emission corresponding to the WINDII observations of Figure 7 [from *Ward*, 1999]. This is for a diurnal tide of average amplitude, with latitude structure given by the (1,1) Hough mode, the accepted airglow chemistry [*McDade*, 1997], and vertical wavelength and phase appropriate to the equinox conditions for the hydroxyl emission shown in Figure 7.

[38] Comparisons of WINDII O(^{1}S) emission rates with the thermosphere ionosphere mesosphere electrodynamics general circulation model (TIME-GCM) were made by *Roble and Shepherd* [1997]. They showed that if the diurnal tide was strong enough to penetrate the airglow at its normal altitude of 97 km, the atomic oxygen distribution was significantly altered, similar to the dramatic perturbation presented by *Shepherd et al.* [1995]. *Zhang et al.* [1998] extended these observations, showing that the maxima in emission rate moved from the equator to 20°N and 20°S at later local times. They also showed that the migrating diurnal tide maxima were modulated by the season and by longitudinal variations. Thus, although the tidal maxima were always evident, they could be degraded or strongly enhanced by other dynamical perturbations. The large seasonal variation of airglow emission rates, as already mentioned, is a feature that almost certainly is dynamically driven. *Liu et al.* [2008] investigated the seasonal variations of the O(^{1}S) and OH emissions in the context of the large-scale circulation and assessed the relative roles of vertical advection and eddy diffusion through comparisons with the TIME-GCM. Evidence for the large-scale circulation associated with high-latitude downwelling in winter and upwelling in summer was detected, but only below 88 km; above this altitude the signature vanished. The model comparisons suggested that vertical advection was dominant, but this did not rule out a role for "eddy diffusion," perhaps more accurately described as "small-scale mixing."

[39] Given that the nightglow variability was dominated by atomic oxygen advection (as indicated by *Ward* [1999]), it was natural to use the relevant photochemical equations to estimate the atomic oxygen present in the mesopause region. This work was undertaken by *Russell and Lowe* [2003], *Russell et al.* [2004], and *Russell et al.* [2005]. In the absence of direct colocated temperature measurements and knowledge of the background density, the MSIS (Mass Spectrometer and Incoherent Scatter) model was used to provide density and temperatures for the atomic oxygen derivations. These papers investigated aspects of the OH photochemistry by comparing the agreement of oxygen derived from OH nightglow using various transition rates and assumptions about the quenching (sudden death verses single quantum and multiquantum cascade) to oxygen derived from the green line measurements. Their analysis suggested that the best combination to use was the Goldman transition probabilities and the sudden death quenching model for the transition observed.

[40] Using this combination, a climatology of atomic oxygen was developed using the hydroxyl and green line nightglow. Features noted in this climatology include the

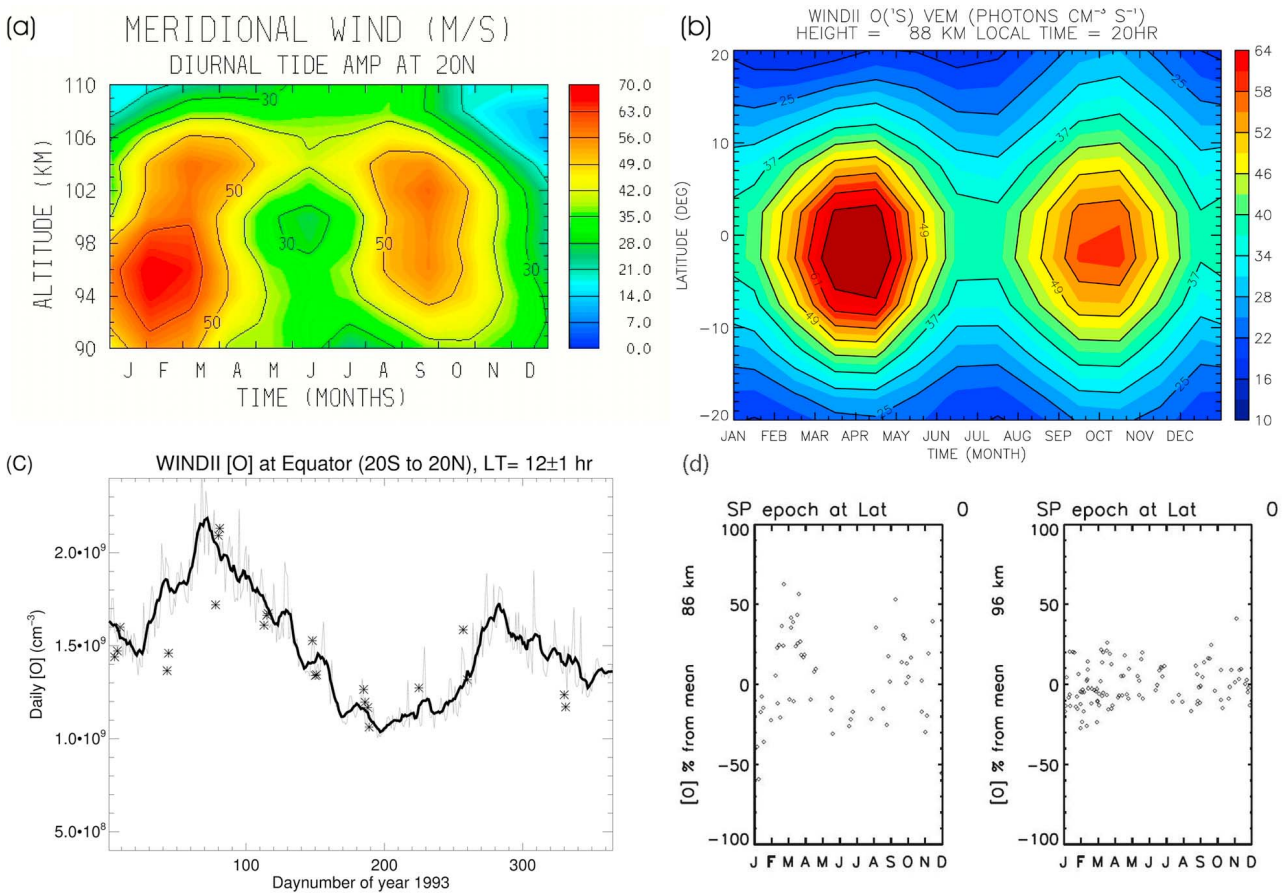

Figure 9. The semiannual variation at the equator as observed by WINDII for (a) the amplitude of the migrating diurnal tide meridional wind at 20°N adapted from *McLandress et al.* [1996a]; (b) the O(^{1}S) emission rate at 88 km and 20:00 LT as a function of latitude (courtesy of Guiping Liu); (c) the WINDII equatorial atomic oxygen concentration at 250 km at 12:00 for 1993 as asterisks—the thick solid line is NRLMSISE-00 averaged over 9 days and the gray line is for daily values; and (d) the atomic oxygen concentration variation at the equator for 86 and 96 km, adapted from *Russell et al.* [2004].

identification of significant local time variations in the oxygen concentration and mixing ratio. This matched the latitudinal and temporal structure associated with the temperature signature associated with the migrating diurnal tide (i.e., descending equatorial maxima with oppositely phased secondary maxima at midlatitudes) as would be expected given the dominance of vertical advection in the transport processes. This was in contrast to the local time variation from MSIS-90, which was out of phase by 180°, presumably because this advection was not taken into account. This also indicated that the interpretation of *Garcia and Solomon* [1985] of enhanced mixing during solstices would need to be revisited once the tidal signatures were accounted for. The now well-known equinoctial maxima during equinoxes, with the northern spring being the largest, were also reflected in the oxygen variations. Semiannual and annual variations in the oxygen concentration were also noted with their relative strengths depending on latitude and height.

[41] Figure 9 illustrates these semiannual variations in four different physical quantities: MLT winds (Figure 9a), MLT O(^{1}S) emission rates (Figure 9b), thermospheric atomic oxygen concentration (Figure 9c), and MLT atomic oxygen concentrations (Figure 9d). Figure 9a shows the semiannual variation of the meridional wind component of the diurnal tide at 20°N as a function of altitude as obtained by *McLandress et al.* [1996a, Figure 13]. This was the first clear indication of a dynamical driver for this variation. Figure 9b shows a dramatic semiannual variation of the O(^{1}S) emission, not at its "normal" altitude, but much lower down, at 88 km, and at 20:00 LT; this variation is not seen at higher altitudes. Figure 9b was kindly provided by Guiping Liu. Figure 9c shows the atomic oxygen concentration at 250 km, derived from the WINDII O(^{1}S) dayglow, on the assumption that the only excitation process is photoelectron impact on atomic oxygen and compared with the NRLMSISE-00 for the equator and a local time of noon. The limited number of WINDII observations is because the local time of noon is observed only for a few days during each yaw cycle. The WINDII data were normalized to the MRLMSISE-00 model for the month of January 1993, but the agreement over the year clearly defines a semiannual variation for both WINDII observations and the model. Figure 9d also shows the

semiannual variation of atomic oxygen, but in the MLT region.

[42] Issues associated with the atomic oxygen variability could not be resolved unambiguously with WINDII data because the nightglow observations did not allow complete local time coverage, and temperature measurements during the night were not available. These are starting to be resolved now that SABER observations of constituents and temperature are becoming generally available and extensive analyses of ground based observations have been undertaken. The dominance of vertical advection on the variability in airglow observations was confirmed by *Cho and Shepherd* [2006]. The significant longitudinal airglow variability seen by WINDII and HRDI, which at one time was attributed to mixing associated with gravity waves [*Hays et al.*, 2003], is now thought to be associated with vertical advection associated with nonmigrating tides [*Xu et al.*, 2010]. *Smith et al.* [2010] used SABER day and night observations of ozone, temperature, and airglow to develop a climatology of atomic oxygen for all local times. They found that the values of atomic oxygen they observed were higher than those observed with WINDII. Further work is needed to determine whether this is evidence for a longer-term trend or a secular variation.

[43] WINDII has also contributed to the knowledge of dynamical variations through the measurement by *Fauliot et al.* [1997] of vertical winds in the 80–120 km region derived from the divergence of the observed horizontal winds. The WINDII tidal measurements were also combined with a model by *Bruinsma et al.* [2002] to derive density variations. In another approach, *Bruinsma et al.* [2003] used the WINDII vertical temperature gradient measurements to derive the densities needed to fix the lower boundary of the DTM-2000 (Drag Temperature Model) empirical thermosphere model. Although these temperatures have a bias, as described later, it does not significantly affect the gradient.

4. PLANETARY WAVES: REVIEW OF WHAT WAS LEARNED

[44] At the time of the UARS launch, there existed a number of studies on stationary planetary waves (SPWs) in the stratosphere and mesosphere (for reviews, see *Barnett and Labitzke* [1990] and *Andrews et al.* [1987]); however, their presence in the 90–120 km region of the MLT for the most part had not been explored. The investigation of planetary waves in the region focused mostly on traveling modes, in particular, the 2 day wave. This is because researchers interpreting disturbance measurements from a single ground station or a limited network of stations must assume that the features are traveling disturbances. Because of the lack of relevant data, SPW variations between 90 and 130 km were not included in the Horizontal Wind Model HWM-93 [*Hedin et al.*, 1996]. Theoretical investigations of SPW, however, had been carried out. *Schoeberl and Geller* [1977] provided an analysis of these waves extending to 100 km.

[45] The WINDII experiment on board UARS produced a unique global data set, substantially increasing the quantity and quality of available wind measurements in the MLT region. The data on the horizontal winds [*Wang et al.*, 2000a] and the emission rates [*Wang et al.*, 2002] taken from the WINDII green line airglow observations during December 1991 through January 1996 were used to describe the climatology of SPW between 90 and 120 km. The mean features and the geographic and temporal variabilities in the SPW amplitudes and phases were analyzed.

[46] The horizontal wind data were taken at latitudes 70°S–70°N and altitudes 90–120 km from the WINDII green line measurements in December and January and March and April of 1991–1996 [*Wang et al.*, 2000a]. The observed solstitial SPW fields were relatively stronger and dominated by zonal wave number 1 variations. In contrast, the equinoctial SPW fields were weaker and characterized by zonal wave number 2 variations. The zonal amplitude maxima of 10–25 m s^{-1} were generally centered at midlatitudes between 35° and 40° in both hemispheres around 96 km, with the eastward perturbation velocity maxima around 90°E for wave number 1 and 60°E and 240°E for wave number 2. The meridional amplitude maxima were about 5–15 m s^{-1} and showed more variability in their latitude-height distributions. The meridional phases indicated that Eliassen-Palm (EP) fluxes were downward-poleward for the winter maxima, vertically varying poleward for the summer maxima, and more variable during March and April. The hemispheric-seasonal-interannual variations in amplitude and phase were of 10 m s^{-1} and 30°, respectively. In particular, a distinguishable local summer maximum with an amplitude of 10–20 m s^{-1} was found to exist in the wave number 1 variation of the zonal wind component. While the summer maximum of the wave number 1 component persisted during the 4 years, large variability was found in the winter hemisphere where the wave number 2 component became significant at the 90–105 km region during December 1992 and January 1993 and December 1993 and January 1994 and at the 105–120 km region during December 1991 and January 1992. The excitation due to in situ forcing of azonal gravity wave drag, which varied longitudinally, was thought to be largely responsible for the observed SPW, particularly for the summer maximum, while the leakage of upward-propagating SPW from the lower to the higher atmosphere also played a role, especially in the winter and the equinoctial periods. The in situ gravity wave forcing of SPWs in the summer extratropical mesosphere was later confirmed by simulations of *Osprey and Lawrence* [2001] using the Hines Doppler spread parameterization of gravity waves.

[47] Recently, the coupling between the stratosphere and mesosphere by planetary waves has attracted significant attention [*Pancheva et al.*, 2008]. It is now recognized that much of the variability in the MLT region is a result of upward propagation of disturbances from the stratosphere, particularly during the winter. The SPW observations of WINDII winds for the Southern Hemisphere summers 1991/1992, 1992/1993, and 1993/1994 have been compared with

the SPW amplitude and phase profiles of the geopotential heights in mid-January at 60°S for 1992, 1993, and 1994 from the TIROS (Television Infra Red Observation Satellite) TOVS (TIROS Operational Vertical Sounder) analysis [*Kirkwood and Stebel*, 2003]. They concluded that stationary planetary waves might be expected to grow in amplitude by about a factor of 10 and to tilt westward by about 90° between 2 hPa and 85 km height.

[48] WINDII observations were combined with HRDI observations to produce a climatology of stationary planetary waves extending from 15 to 110 km by *Forbes et al.* [2002]. They produced a climatology which allows the vertical propagation characteristics of these waves to be examined as a function of season. They concluded that even with this extended vertical coverage it was difficult to distinguish between in situ–generated waves and those which leaked upward through the propagation barrier which typically exists at 80 km.

[49] Longitudinal variations in the WINDII green line airglow volume emission rate data at latitudes 70°S–70°N and altitudes 90–120 km in December and January and March and April of 1991–1996 showed relatively stable or stationary patterns, which persisted from year to year and existed at fixed local times during the solstice and the equinox [*Wang et al.*, 2002]. In general, the nightglow exhibited zonal wave number 1 and 2 variations in the southern and northern latitudes around 35°, respectively. The dayglow displayed a wave number 2 variation near the equator, with a tendency toward 10°S–20°S for the solstitial period. All structures were seen to extend over 10° or more of latitude. The emission rates varied significantly, changing by a factor 2 or more at the minima and maxima of the wave structures. Primary maxima were around ~180°E–240°E for the nightglow, and ~300°E–360°E for the dayglow, while secondary maxima were near ~90°E–120°E for both airglows. Their magnitudes also showed systematic decrease by a factor of 3 from 1991 to 1996, perhaps due to decreases in solar activity and tidal amplitude. The existence of a stationary planetary wave structure suggests the importance of coupling processes between the mesopause and the Earth (or lower atmosphere) in understanding the airglow variations, in addition to the well-known solar-driven photochemistry.

[50] Work by *Ward et al.* [1996, 1997] examined the structure of the 2 day wave during a strong event during January/February 1993. Both the wind structure and oxygen green line airglow signatures associated with this wave were examined. Because of the particular character of the WINDII orbit at the time (close to 24 h of daylight in the Southern Hemisphere) this is one of the few papers which examines the vertical structure of this wave in the lower thermosphere. It shows the wave penetrating into the lower thermosphere with maximum amplitude near the mesopause and a secondary maximum near 110 km. Above 130 km, the wave appears to be evanescent. Variations in the wave amplitude with latitude were significant with maxima in the zonal wind in the Northern and Southern Hemisphere midlatitudes and at the equator. Significant 2 day variation in the airglow was observed during this event and was attributed to vertical advection associated with this wave.

5. GRAVITY WAVES: THE CAPABILITY OF WINDII FOR THEIR OBSERVATION

5.1. Gravity Wave Spectra Observed From WINDII Measurements

[51] Gravity waves play an important role in the mesosphere and lower thermosphere, where they determine to a large degree the large-scale circulation and thermal and constituent structures. In the early 1990s, theoretical and observational studies (see *Wang et al.* [2000b, 2000c] for detailed references) had shown a universality of the spectral shape and amplitude for the mean atmospheric motion spectra. For horizontal winds and temperature, mean frequency spectra typically exhibited a slope near $-5/3$ with only slight amplitude variations, while the form of the vertical wave number spectrum appeared generally to be consistent with spectra of a slope near -3 at high wave numbers. Various models had also been proposed to explain the features of the observed spectra. The Doppler spread theory [*Hines*, 1991a, 1991b], the diffusive [*Gardner*, 1994] and nondiffusive models [*Gardner et al.*, 1993], and the saturated-cascade model [*Dewan*, 1991, 1994] suggested the importance of the Doppler effect, wave energy dissipation, and cascade processes, correspondingly, in maintaining the observed spectral shape and amplitude. Observational data are required to test the fundamental physics upon which these theories are based.

[52] The horizontal wind and temperature data inferred from the WINDII green line observations were used to derive global maps of vertical and horizontal wave number spectra, and to investigate the temporal/geographic variations of atmospheric wave motions [*Wang et al.*, 2000b]. The planetary-scale disturbances between 90 and 120 km in September 1995 were found to be characterized by large RMS velocities of ~30–45 m s^{-1} and fractional temperatures of ~5–9%, with maximum velocity variances in the region over the equatorial Indian-Central Pacific oceans. In contrast, the small-scale gravity waves displayed mean fluctuation amplitudes of ~18–30 m s^{-1} and 3%–6%, with the maxima at midlatitudes. The velocity variances of both scales slowly increased with increasing altitude at the lower heights, with a faster growth for the large-scale waves, but remained virtually constant above ~105 km due to the wave breaking and saturation. The results also revealed strong correlations between the longitudinal and temporal variations of the large- and small-scale waves. Vertical and horizontal wave number spectra observed at different locations and times showed great similarities, supporting the notion of "universality." Horizontal wave number spectra are shown in Figure 10 for winds and temperatures determined from the O(^{1}S) emission for two altitude ranges, 97.5–102.5 km and 92.5–97.5 km. The data were taken between 14 and 21 September 1995.

[53] Vertical and horizontal wave number spectra of horizontal wind and temperature observed with WINDII were

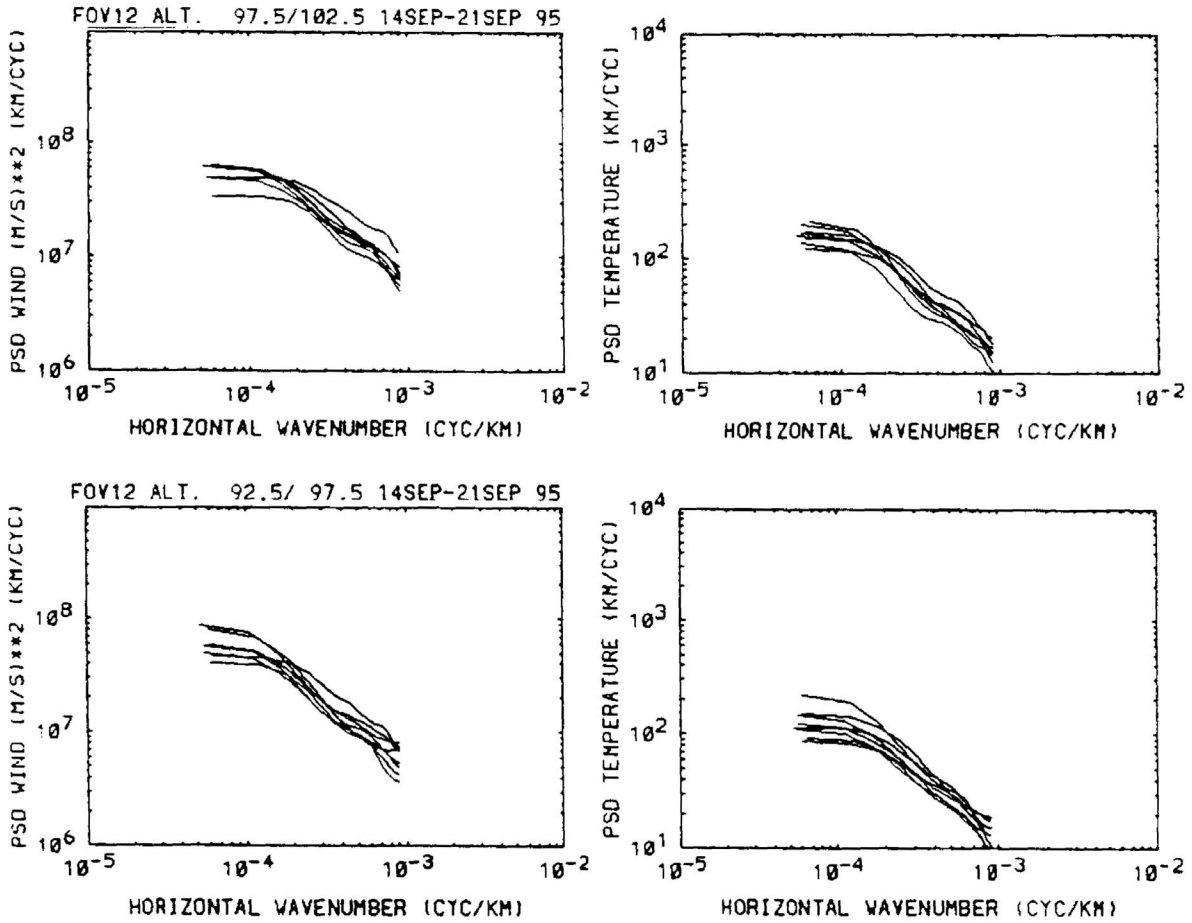

Figure 10. Horizontal wave number spectra determined from the O(^{1}S) emission for (left) wind and (right) temperature for two altitude ranges: 97.5–102.5 km (above) and 92.5–97.5 km (below). Data were acquired from 14 to 21 September 1995. Adapted from *Wang et al.* [2000b].

used to examine the effect of the diffusion process on the spectral evolution [*Wang et al.*, 2000c]. At small wave numbers, the spectral slope was generally found to be close to zero, due to the restriction of the diffusion process. The observed spectra were compared with the diffusive and cascade models, as well as the nondiffusive model [*Gardner et al.*, 1993]. The results showed that the diffusion process played an important role in maintaining the shapes and amplitudes of vertical wave number spectra but was less significant for horizontal wave number spectra at the observed large wavelengths.

5.2. Airglow-Gravity Wave Interactions Observed From WINDII Measurements

[54] The response of airglow emissions to the passage of gravity waves has been the subject of numerous studies (see references listed in *Wang et al.* [2001a, 2001b]). While most theoretical studies on the response process have been done in an Eulerian reference frame (fixed in space), *Hines and Tarasick* [1987] developed a quasi-Lagrangian treatment (with the physics inferred by following an air parcel in its orbit) of the effects of gravity waves on airglow intensity. They stressed the linear nature of the wave-airglow interaction [*Hines and Tarasick*, 1993] and summarized it as a fundamental theorem for ground-based measurements of the wave-induced airglow fluctuations [*Hines*, 1997]. For the wind measurements from ground-based and satellite limb airglow observations (e.g., WINDII and HRDI), the volume of space sampled by the limb scans is generally assumed to be spherically homogeneous, and the effects of small-scale variations of the atmosphere are neglected. In reality, the limb-measured airglow intensities under the influences of gravity waves can be significantly different from those in the absence of the waves and strongly depend on the viewing geometry and the wave parameters. An accurate knowledge of gravity wave-airglow interactions is particularly important for correctly retrieving the atmospheric field from the limb-scanned measurements.

[55] The linear theory of gravity wave-airglow interaction based on the Lagrangian approach [*Hines and Tarasick*, 1987] has been generalized to limb observations by *Wang et al.* [2001a, 2001b]. A set of equations describing the wave-induced fluctuations of temperature, line-of-sight (LOS) wind, and volume emission rate (VER) were obtained

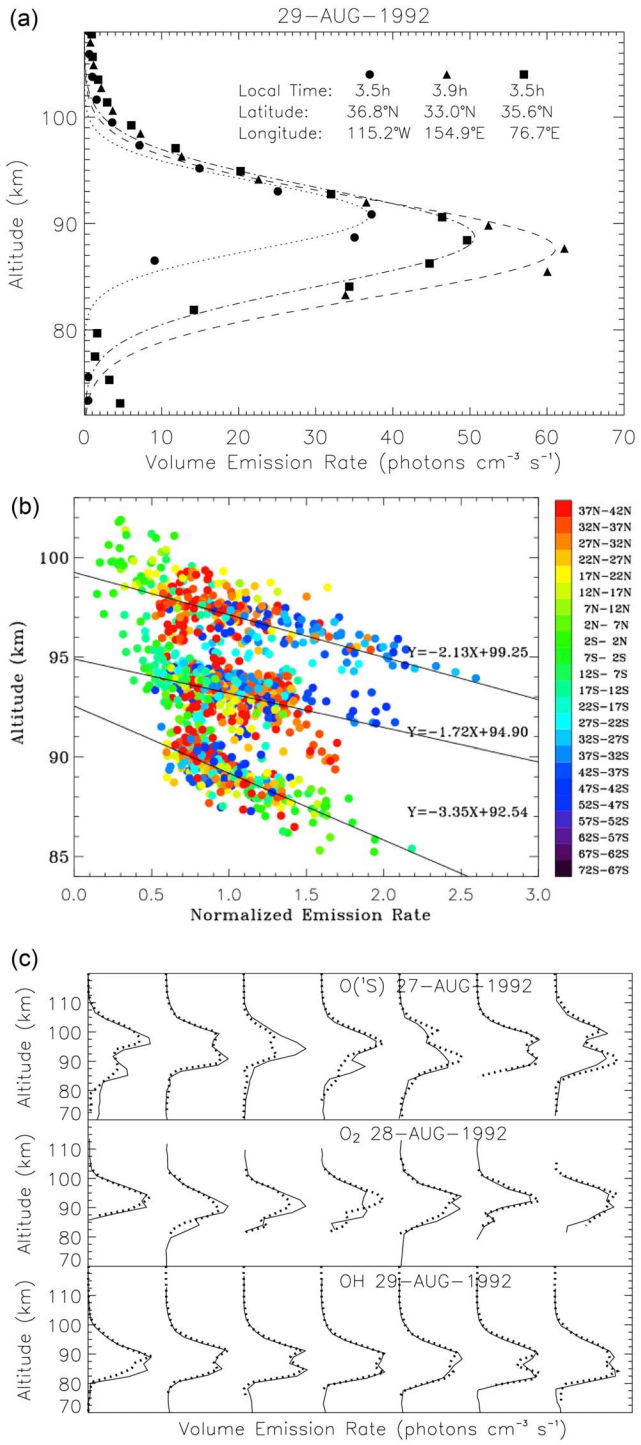

Figure 11. (a) Three OH emission rate profiles taken at the same local time and latitude but different longitudes on the same day, 29 August 1992, after *Liu and Shepherd* [2006a]. (b) Altitudes of emission rate peaks versus normalized emission rate for O(^{1}S), O_2(Atm), and OH (top to bottom, respectively) from 25 to 27 March 1992, respectively, showing the inverse relationship between the altitude and peak emission rate. The different colors correspond to different latitudes. Courtesy of Guiping Liu. (c) Perturbed profiles of O(^{1}S), O_2(Atm), and OH from 27 to 29 August 1992, respectively. The dotted and solid curves are for the two superimposed WINDII field of view profiles [after *Liu and Shepherd*, 2006b].

for limb observations with a photometer or interferometer [*Wang et al.*, 2001a]. The results can also be applied to ground-based measurements. Approximations at small and large zenith angles, θ, were considered. As a central part of the treatment, the VER variation is expressed in terms of the atmospheric density (or temperature) perturbation and the displacements parallel and perpendicular to the LOS. The relative importance of these effects is characterized by an effective scale, λ_c, of the photochemical-dynamical interactions between a wave and the airglow emission. This effective scale is shown to be ~33 km in the MLT for emission processes of three-body reactions and to slowly increase with increasing wave vertical scales. At small zenith angle observations, the VER variation is dominated by the effect of the vertical displacement (in geographic frame) or of the density (or temperature) perturbation for waves with vertical scales smaller or larger than λ_c, respectively. The small-scale height, H_ε, of the emission layer may play an important role only for limb measurements. When $\lambda_c > 2\pi H_\varepsilon$, the VER variation is primarily controlled by vertical wave motions for a broad spectrum of vertical scales.

5.3. Direct Observation by WINDII of Small-Scale Structure in Airglow Emission

[56] Mesospheric O(^{1}S) green line, $O_2(b^1\Sigma_g^+)$ Atmospheric (0–0) band, and OH (8–3) Meinel bands $P_1(3)$ line nightglow emissions originate from the recombination of atomic oxygen (e.g., as reviewed by *McDade and Llewellyn* [1986], *McDade et al.* [1987], and *Meriwether* [1989]). They have been used as passive tracers of atmospheric waves in the upper mesosphere. By observing these emissions, ground-based and rocket optical instruments have detected small-scale gravity waves [e.g., *Taylor et al.*, 1995; *Makhlouf et al.*, 1997; *Iwagami et al.*, 2002].

[57] *Baker and Stair* [1988] summarized many rocket measurements of the altitude of the hydroxyl airglow by various groups. Their data showed that the average value of the peak height was 87 km with a half width of about 8 km. Although the rocket profiles provide a good indication of hydroxyl volume emission rate profile, the sporadic character of the rocket measurements makes it difficult to identify variations associated with dynamical features and did not reveal their full impact on the atmosphere. The variability is illustrated in Figure 11a, in which three WINDII OH nightglow profiles are shown for the same local time and the same latitude on the same day, but at different longitudes. A consistent change of the altitude with peak emission rate is evident.

[58] The early WINDII measurements confirmed that the OH (8–3) volume emission rate generally has a maximum located between 85 and 90 km with an approximately exponential decay to both lower and higher altitudes [*Lowe et al.*, 1996; *She and Lowe*, 1998]. Subsequently, *Liu and Shepherd* [2006a] carried out a statistical analysis of 50,000 OH profiles and found a simple empirical relationship between the altitude of the emission rate peak and the peak emission rate at that altitude. As the peak emission rate increases, the altitude of the peak decreases, with an overall

variation of altitude of more than 7 km. This consistent behavior is shown in Figure 11b for the O(^{1}S), the O_2 Atm, and the OH emissions. As well, the height profile is sometimes more complex, as seen previously in some rocket experiments, frequently with two maxima in the volume emission rate separated by several kilometers [*Melo et al.*, 2000]. This is illustrated in Figure 11c for the O(^{1}S), O_2 Atm, and OH emissions, where superimposed profiles from the two fields of view are shown. For some cases the two profiles agree well, indicating horizontal homogeneity over the region of horizontal integration, about 300 km. For other cases, where the two profiles differ, horizontal structure of this scale is indicated.

[59] As shown by *Melo et al.* [2000], the frequency of occurrence of the double-peaked hydroxyl layers in the WINDII observations is a function of season, latitude, and local time. Among many thousands of the night measurements from November 1991 to April 1995, 5%–25% of the measured profiles have a more complex structure for the layer profile, most frequently with two peaks separated by 4–6 km. The horizontal extent varies from 200 to several thousand kilometers, and the duration may be as long as 1.5 h. Early in the night the double-peaked layers occur preferentially at low to medium latitudes, migrating toward the equator by midnight, where they remain for the rest of the night. There is a pronounced asymmetry between the hemispheres which reverses between the March/April equinox and the September/October equinox. The solstice behavior is similar, though not so pronounced.

[60] Through simulation, three possible causes of the observed OH double-peaked layers were identified; the occurrence of a mesospheric temperature inversion layer, disturbance in the shape of the bottom side of the atomic oxygen profile due to turbulence, and the propagation of short vertical wavelength gravity waves through the layer. Gravity waves are a likely source of isolated small-scale events, but the large horizontal-scale, long-duration structures are more likely to result from temperature inversion layers or mixing events, or a combination of the two.

[61] Similar studies were extended by *Liu and Shepherd* [2006b] to include the O(^{1}S), $O_2(b^1\Sigma_g^+)$ Atmospheric (0–0) band, and OH (8–3) Meinel bands $P_1(3)$ line, the three oxygen nightglow emissions. Occurrences of the apparent multiple-peak profiles were evaluated from the nearly 6 years of WINDII data in a near-global coverage. A systematic relationship was found between their latitude/local time distributions and the emission rate patterns that are dominated by the effects of the diurnal tide. Perturbed profiles having multiple peaks in the three nightglow emissions in the mesopause region were frequently observed by WINDII over the study period of 1991–1997, comprising up to 40% of the observations in bins having certain latitudes and local times. The preferred locations and times for their occurrences coincide with steep emission rate gradients associated with the diurnal tide. It is thus proposed that the perturbed profiles arise from the dynamical influence of the diurnal tide. It is also suggested that the WINDII multiple peak profiles may be caused by horizontal as well as vertical perturbations. The limb-viewing geometry of the satellite and the onion-peeling method for its data inversion imply that the multiple peaks can result from horizontal variations as well as vertical ones.

[62] To examine the influence of horizontal variations on the vertical emission profile, a 1-D model was developed by *Liu and Shepherd* [2006b]. It assumes that the airglow emission rates vary according to a sinusoidal function in the horizontal direction combined with a Gaussian function in height. Inverted emission rates were calculated for various horizontal wavelengths. The model results showed that the secondary peak in the vertical emission profile could be the reflection of a wavelike horizontal structure with wavelengths between 100 and 400 km. The features of the horizontal structures correspond to localized regions of gravity waves with extents up to 2000 km and lifetimes of one or more days. It is concluded that the WINDII perturbed emission profiles could be produced by horizontal variations induced by gravity waves with wavelengths between 100 and 400 km, and that these occur in preferred regions of steep emission rate gradients associated with the diurnal tide.

6. TEMPERATURE MEASUREMENTS IN THE MLT

[63] The WINDII instrument was designed to measure winds and temperatures, and these comprised the data provided to NASA. Although the emission rates subsequently turned out to be very useful scientifically, they were not included in the delivery. The measurement of winds has already been described and reference has been made to temperatures. Two types of temperature measurement were planned, Doppler temperatures and rotational temperatures. After launch it was found that temperatures could be found from Rayleigh scattering in the upper mesosphere. The Doppler method is described first.

6.1. Doppler Temperatures

[64] The Doppler temperatures were to be obtained from the O(^{1}S) and O(^{1}D) atomic oxygen lines following the procedures established in the original DMI measurements by *Hilliard and Shepherd* [1966b] and *Zwick and Shepherd* [1973]. This is based on a measurement of what Michelson called the "visibility," described in section 1. The determination of the atmospheric line visibility profiles as a function of altitude from the WINDII airglow emission measurements is summarized in that same section.

[65] Assuming that the line shape is Gaussian, corresponding to the atmospheric temperature, its transform in the interferogram is also Gaussian and so there is a direct relationship between the visibility of the atmosphere and the temperature [*Hilliard and Shepherd*, 1966b] as given in equation (7). For more details see *Shepherd* [2002] and *Lathuillère et al.* [2002]. It is also necessary to take into account the influence of the interferometer on the visibility. The observed visibility for a line of infinitesimal line width, such as from a laser, is called U and the observed visibility is $V_{obs} = U \times V$. Thus, a laser was carried on board, as described by *Shepherd et al.* [1993a] and used in the infrequent calibration, as described by *Thuillier et al.* [1998].

[66] In implementing this method there are two critical issues. The first is the correct subtraction of background referred to above and in section 1, since this directly affects the observed visibility. Care was taken in this for the O(^{1}S) emission at 557.7 nm, with a background channel at 553 nm. One has to be sure that no airglow lines, even weak ones, are present in the background channel. The emission and background channels have to be carefully calibrated and have allowance made for the slight differences in wavelength, as the calibration is done with a tungsten source and the background for O(^{1}S) in the daytime is Rayleigh scattered sunlight. For the nightglow, the NO_2 continuum (section 7.4) and starlight are the main background sources. The same background channel was used for the O(^{1}D) emission, which has a greater wavelength separation, but at these higher altitudes the background light is less. The laboratory calibrations were refined in orbit by comparing the emission and background from the two fields of view for observations of the same volume of atmosphere, for which the line emission is expected to be the same, but not necessarily the background [*Gault et al.*, 1996a]. The second issue is whether the emission is in thermal equilibrium, that is, whether the emitting atoms have a velocity distribution that is Boltzmann with respect to the temperature of the background atmosphere. It was considered that this would be true for the O(^{1}D) emission as its lifetime is about 110 s, which would seem to be long enough to thermalize, especially at the higher altitudes from which it occurs. For the O(^{1}S) emission with a 1 s lifetime, it was considered that the emission would become nonthermal above 130 km.

[67] Temperature measurements for the O(^{1}D) emission were reported upon by *Lathuillère et al.* [2002] and compared with the extension of the MSIS-90 model into the thermosphere by *Hedin* [1991]. A correlation coefficient of 0.97 was found reflecting the fact that during magnetically quiet times the WINDII temperatures tracked the model values extremely well, including the variations with latitude. During disturbed events WINDII showed larger variations, as expected from instantaneous measurements, as compared with a model. In spite of this agreement the WINDII temperatures were on average 100 K higher than the model. The possible reasons for this persistent bias are discussed by *Lathuillère et al.* [2002], consistent with the discussion above, but focusing on the nonthermalization explanation for which other evidence exists; they not repeated in full here but are discussed in detail by *Hubert et al.* [2001].

[68] *Lathuillère and Menvielle* [2004] showed that the WINDII O(^{1}D) temperature perturbations (the temperature difference between disturbed and quiet conditions) correlated well with magnetic activity, with a better description when regional rather than global indices were used. They also showed good qualitative agreement between the WINDII temperature measurements and the MSIS-90 and DTM94 models, although the models underestimate the observations.

[69] A preliminary O(^{1}S) temperature profile is shown by *Shepherd et al.* [1993a]; it is consistent with MSIS at 100 km with 250 K, but then increases linearly with altitude, reaching 1850 K at 250 km. This is as expected considering the short lifetime and the upper limit of 130 km expected for thermalization of these atoms. However, more extensive investigations have found, as for O(^{1}D), a large bias between observations and models. For the altitude range 90–140 km, the WINDII temperature differences with the MSIS model are in the range 30–70 K, although they are less in comparison with the measurements on which the MSIS model are based. Thus, at the present time for this lower temperature regime this bias is also not understood. For this reason, no results from these studies have been published, except for *Wang et al.* [2000b, 2000c] noted earlier, where relative temperatures were adequate.

6.2. Rotational Temperatures From Hydroxyl Airglow

[70] Considerable effort was put into the determination of rotational temperature from hydroxyl airglow emission in the upper mesosphere. The method is well established from ground-based measurements [*López-González et al.*, 2007] essentially taking the ratio of different lines in a rotational band, chosen to maximize the change of ratio as a function of temperature, reflecting the populations of the states giving rise to those lines. Filter 4 was designed to transmit the OH $P_1(2)$ line at 731.63 nm in the (8,3) Meinel band when viewed at an off-axis angle, corresponding to an altitude of around 80 km, at the bottom of the CCD. Near the top of the CCD, corresponding to 300 km and a different off-axis angle, it was intended that the same filter transmit the O^+ ^{2}P 732.0 line and a fraction of the 733.0 nm line. This requirement complicated the Michelson interferometer design as all these lines, OH and O^+, are doublets. In order to maintain the visibility, the interferometer should see the two components of the doublet in phase, putting a constraint on the optical path difference. It was not possible to achieve the ideal condition for all components, but an acceptable compromise was found. Unfortunately, most of the O^+ emission comes from above the top of the window, so meaningful inversions could not be carried out. The O^+ measurements are discussed in section 7.3.

[71] Filter 6 was designed to transmit the OH $P_1(3)$ line at 734.09 nm, providing with Filter 4 the required ratio measurement. However, the background is also critical and was measured with Filter 5, a filter split into two broad filters with different central wavelengths, one corresponding to the background and the other to the emission from the whole OH band. The images were separated on the CCD by covering one filter with a prism so that the two images were stacked one above the other. For reasons that are still not understood, acceptable rotational temperature results were not obtained. Because the background filter, with a full width at half maximum (FWHM) of 11.0 nm and a center wavelength of 714.8 nm, is close to the selected lines, the subtraction of background is not expected to be an issue. No drifting of the central wavelength or other degradation of the interference filters was detected during the mission, while the filters were operated at their normal operating temperature. Because the different filters were used sequentially in time, there was a problem with interpolation and registration.

Another possibility is the presence of "unknown" airglow lines. Although this region of the spectrum was thought to be well known, airglow measurements from the HIRES (High Resolution Echelle Spectrometer) instrument on the Keck telescope at Mauna Kea [*Slanger and Osterbrock*, 2000] have discovered previously unknown lines, so this may contribute to the problem. In any case, results from these observations have not been published.

6.3. WINDII Temperatures Derived From Rayleigh Scattering

[72] Upper mesospheric temperatures were derived using limb radiance measurements of the daytime Rayleigh scattered solar continuum at 553.1 nm wavelength, taken through Filter 1, the background filter for the atomic oxygen green line. The temperature retrieval algorithm consisted of two steps. First, the *Chahine* [1972] relaxation method was applied to the integrated line-of-sight radiance data to retrieve tangent height volume scattering rate (VSR) profiles which are a relative measure of atmospheric density. The method can specifically be employed in cases where the weighting functions have well-defined peaks, and thus, it is well suited for the WINDII inversion problem. Second, temperatures from the relative density profiles are calculated using hydrostatic equilibrium and the ideal gas law, an approach patterned after the methods used to derive Rayleigh lidar temperatures. Some early results were reported upon by *Evans et al.* [1994a, 1994b] and *Shepherd et al.* [1997]. The retrieval procedure employing WINDII Level 1 Rayleigh scattering radiances and the validation of the temperature data in the altitude from 65 to 90 km has been described in detail by *M. G. Shepherd et al.* [2001]. The typical temperature uncertainty values for individual profiles were determined to be <2.5%, 5.5%, and 13% for altitudes of 70 km, 80 km, and 90 km, respectively. A thorough comparison of the derived WINDII temperatures performed against a number of ground-based and satellite measurements showed the retrieved data to be in good to excellent agreement with a number of established methods; proving that WINDII data can be used to confidently derive near-global temperatures of the upper mesosphere between 65 and 90 km [e.g., *M. G. Shepherd et al.*, 2002, 2004a, 2004b].

[73] Subsequently, the Chahine method part of the algorithm was replaced by the normal WINDII Level 2 VSR inversion [*Rochon*, 1999]. Considering the exponential-like increase in VSR with decreasing altitude, the inversion solutions are unconstrained below about 95–100 km. Further details on the Level 2 VSR retrieval are provided in *M. G. Shepherd et al.* [2004b]. The WINDII Level 1 and Level 2 temperature data were employed in a number of studies examining the seasonal and longitudinal variability of mesospheric temperatures providing a 7 year global climatology of the upper mesosphere.

[74] *G. G. Shepherd et al.* [1999, 2004a] described a "springtime transition" in lower thermosphere atomic oxygen based on WINDII wind and airglow emission rates and on ground-based temperature and airglow emission rates. The ground-based data indicated rapid global perturbations in airglow emission rates and temperature lasting about two weeks near the end of March. The satellite observations were not capable of revealing the rapid variations at individual sites but showed a transient global perturbation in the planetary-scale structure of the oxygen emission rates. The transition is characterized by a rapid 2 day rise in the oxygen nightglow emission rate by a factor of 2 to 3 followed by a subsequent decrease by a factor of 10 in the same period of time indicating depletion of atomic oxygen that persists for days. The WINDII Rayleigh scattering temperatures were examined for signatures in the upper mesosphere temperature fields (70–95 km height range), which might be associated with the springtime depletion of the atomic oxygen [*Shepherd et al.*, 2002]. Comparisons with ground-based OH airglow rotational temperatures, Na lidar, and Rayleigh scattering lidar and meteor temperatures at middle and high latitude in the Northern Hemisphere for March/April 1992 and 1993 showed a rapid enhancement at Northern Hemisphere midlatitudes (35°N–45°N) over a period of 4 days centered on day 85 (25 March) with temperatures about 20 K higher than for the preceding 2 weeks and above the annual variation fit at 87 km. The average annual enhancement took place within a period of about 30 days from the second half of March to the first half of April. By the end of April the averaged annual temperature returned to its seasonal values on the annual variability fit. The pattern is similar to that associated with the "springtime transition" observed in the atomic oxygen. Analysis of other temperature data sets showed that the temperature enhancement observed was a feature of the annual temperature variability both at ~40°N and ~60°N. All results strongly indicated that the mesospheric temperature enhancement is associated with perturbations in the stratospheric thermal structure and the final stratospheric warming in particular, possibly leading to dynamical perturbation of wave numbers 1 and 2 in the Northern Hemisphere [*Shepherd et al.*, 2002].

[75] The WINDII daytime zonally (longitudinally) averaged temperatures were also employed in the study of the global and seasonal variability of the upper mesospheric temperature field [*M. G. Shepherd et al.*, 2004a]. The latitudinal variability of the annual cycle of mesospheric temperature at 75 km, 82 km, and 87 km was examined from 20°S to 65°N with particular attention being given to the latitude range of ±40° around the equator. The analysis revealed the presence of a dominant annual ~90 day and 60 day oscillations at high northern latitudes and a strong semiannual oscillation (SAO) at equatorial and tropical latitudes. A quasi-biennial oscillation (QBO) was also identified extending from 45°S to 65°N. At 75 km the SAO is manifested as minima in the temperature composites at spring and fall equinox and maxima at winter and summer solstice; at 87 km the SAO is out of phase with respect to the 75 km SAO, with maxima at equinox and minima around the solstice periods. The phase reversal takes place around 82 km and is associated with the temperature inversion between 77 km and 86 km height. The WINDII global climatology revealed mesospheric SAO asymmetry with a stronger September equinox and interhemispheric asymmetry with a quieter and colder Southern

Hemisphere. This is the first global daytime temperature climatology in the upper mesosphere and in the vicinity of the mesopause taken at high vertical and temporal resolution.

[76] The 7 year climatology at middle and high latitude also revealed a V-shaped signature of temperature decrease with amplitude of ~25 K below the annual mean and a duration of 3–4 weeks depending on the year following fall equinox (days 257–284) [*M. G. Shepherd et al.*, 2004b]. Satellite and ground-based temperature observations were successfully combined to infer tidal information, a key in the interpretation of the results obtained as shown and discussed by *M. G. Shepherd et al.* [2004b] and *Shepherd and Fricke-Begemann* [2004]. After accounting for the tidal perturbations a distinct structure of wave numbers 1 and 2, planetary perturbations were revealed at latitudes from 45°N to 65°N, maximizing on days 263–265 (20–22 September). A waveform with wave number 4 was found to be the third most persistent wave signature during fall equinox with a period of about 4 days, followed by a depressed planetary wave activity.

[77] The WINDII data between 1991 and 1997 have shown significant deviations from the global temperature climatology during the equinox periods which varied in magnitude from year to year. Combining correlative satellite and ground-based observations confirmed these findings and allowed a more detailed investigation of the sources of this variability, as discussed by *Shepherd et al.* [2005]. One particular feature observed in the WINDII daytime daily zonal mean temperatures at 87 km height was a cold temperature perturbation in the spring of 1993 (March/April), which was also seen in 1995 and 1997 over the latitude range 25°S to 25°N. The perturbation appears centered at 10°S as a departure of 10 K to 35 K below the semiannual climatological mean, which peaks at equinox. After accounting for tidal contributions to the observations, by adopting tidal parameters determined from the Microwave Limb Sounder (MLS) temperature observations, the cold temperature signature still remained in the residual data. The perturbation is a global phenomenon immediately following March equinox and lasts over a period of 2 weeks. A cross section of the temperature monthly zonal mean data and month of the year over the period from January 1992 to December 1995 revealed a distinct mesospheric semiannual oscillation (MSAO), modulated by a QBO with strong cold anomalies in March/April 1993, 1995, and 1997 in excellent agreement with the MSAO easterly phase of correlative MF radar wind observations at Tirunelveli (8.7°N, 77.8°E). It was shown that the observed temperature anomalies could be produced by the residual circulation associated with the wave driving of the MSAO itself.

[78] The MSAO observed in the WINDII Rayleigh scattering temperatures correlated with similar signatures in WINDII atomic oxygen and hydroxyl nightglow emission rates observed at equatorial and tropical latitudes over the period from January 1992 to December 1995 [*Shepherd et al.*, 2006]. Cross sections of the zonal monthly mean temperatures and airglow profiles in the latitude range ±15° show a distinct MSAO and, their relationship with the wind MSAO and apparent modulation by the stratospheric QBO. The first half of the MSAO cycle (beginning with a cold temperature anomaly in the northern winter) appears stronger at the equator, both for the temperature and the airglow emissions compared to the second half (beginning with a cold anomaly in the Southern Hemisphere). In the airglow emissions the MSAO appears as alternating cells of enhanced and decreased emission rate of the O(^{1}S) and OH emissions, corresponding to cold and warm temperature anomalies. The QBO effect is observed as a temperature decrease and O(^{1}S) and OH emission rate enhancements during the easterly phase of the wind MSAO with peaks at the equator in March/April 1993 and 1995. Away from the equator the O(^{1}S) MSAO/QBO coupling appears 180° out of phase with respect to that at the equator with emission rate enhancements in March/April 1992 and 1994. The observed temperature and airglow signatures correlate strongly with the QBO and easterly phase of the zonal wind MSAO. At the 5°S–15°S latitude band, the wind MSAO deteriorates into the prevailing easterly wind, possibly resulting from downward motion of the stratospheric SAO westerlies and small-scale wave activity. Figure 12 shows the MSAO in temperature and O(^{1}S) emission rate at the equator (±5°) and its modulation by the QBO.

[79] In studying the temperature variability of the upper mesosphere and its climatology, combining the WINDII satellite observations with other satellite and ground-based data provided a better understanding of the morphology of this variability and its sources. The studies carried out showed the observed phenomena have a global manifestation and greatly affect seasonal and intra-annual variability of the upper mesosphere. Whenever the observations were insufficient to give the complete picture, data-assimilated fields were employed in the analysis, as was reported by *Shepherd et al.* [2007, 2008] in examining sudden stratospheric warming (SSW) effects on the tropical mesospheric temperature field. Temperature observations from WINDII and the MLS experiments on UARS and the SABER instrument on the TIMED satellite were analyzed together with MF radar winds and the UK Met Office (UKMO) assimilated field. At the time of stratospheric warming a mesospheric cooling was observed at the tropics correlative with stratospheric warming events at middle and high latitudes. Planetary waves with wave number 1 and with periods of 4–5, 6–8, and 10–18 days were found to dominate the northern winter season, while westward 7 day and 16 day waves at the tropics appeared enhanced by stationary planetary waves during events of SSW.

7. WINDII SPIN-OFF SCIENCE: AIRGLOW, NO, O^+, PMC, AND SOLAR FLARES

[80] As part of routine processing to provide near-global distributions of meridional and zonal wind speeds in the upper mesosphere and lower thermosphere, as described above, WINDII serendipitously provided volume emission profiles of the daytime and nighttime target airglow feature emission rates. Of particular interest were those of the O(^{1}S)

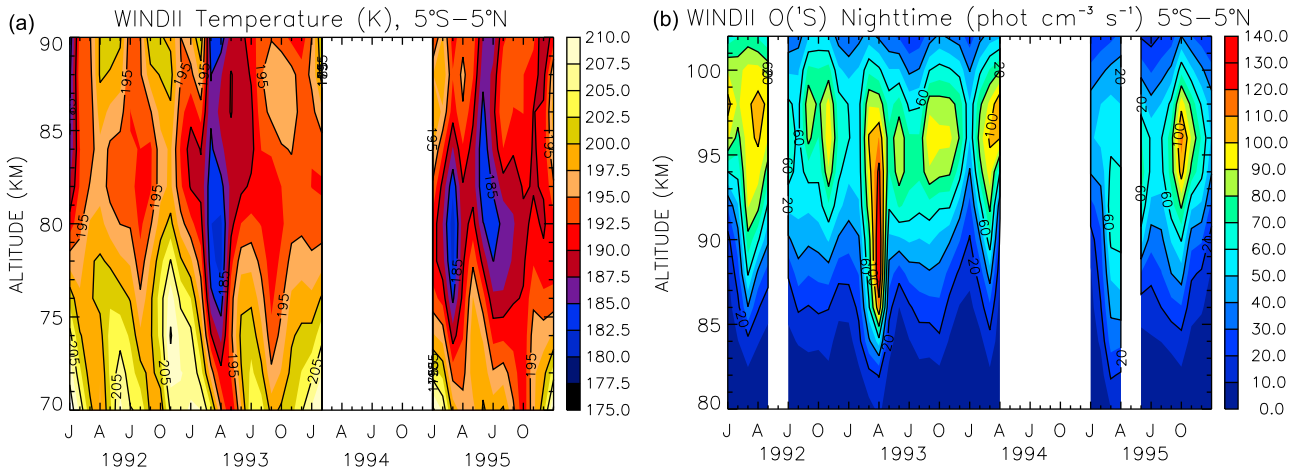

Figure 12. (a) Monthly zonal mean temperature profiles for the period from January 1992 to December 1995 from 70 to 90 km height at the equator (5°S–5°N). (b) Monthly zonal mean O(^{1}S) emission rate profiles for the period from January 1992 to December 1995 from 80 to 110 km height at the equator (5°S–5°N). From *Shepherd et al.* [2006].

green line at 558 nm, the O(^{1}D) redline pair at 630 and 634 nm, the $O^+(^2P)$ pair at 732 and 733 nm, and the Meinel OH 8–3 band at 727 nm. Continuous spectral features, such as the background MLT "airglow continuum" emission near 553 nm, a new stratospheric airglow continuum from 580 nm to 1060 nm, and "anomalous" Rayleigh background scattering of sunlight in the mesosphere, were observed as well. The daytime O(^{1}S) emission also revealed the impact on the airglow of solar flares.

[81] The WINDII database contains a wealth of information still to be exploited on these features; here we only illustrate a few case examples which, at the time of original publication, represented the most comprehensive "survey" of the global and temporal characteristics of these airglow features. These studies have led to questions about the photochemistry assumptions, refined model parameters, challenged established ideas, and inspired further investigation. The details of these cases are not closed yet and are undergoing further study.

7.1. The Dayglow O(^{1}S) Green Line Emission

[82] Altitude profiles taken during one day, 2 December 1992, of the O(^{1}S) volume emission rate during daytime are shown in Figure 13, showing two peaks, one just above 100 km and the other near 150 km, the former peaking around 500 photons cm^{-3} s^{-1}. The small spikes at 200 km and above are thought to be reflections in the baffle system. O(^{1}D) volume emission rate profiles are shown for the following day; these show a single peak near 200 km at 300 cm^{-3} s^{-1}. Altitude profiles of the zonal wind are also shown in Figure 13 for the corresponding days, illustrating the variability over the course of one day, corresponding to the full range of longitudes, as already discussed.

[83] Much progress has been made in understanding the mechanisms for the excitation of the dayglow O(^{1}S) green line emission, but these are still not fully understood. The work by *Singh et al.* [1996a], which was refined by *Witasse et al.* [1999] and *Culot et al.* [2004], using WINDII observations raised questions about many of the relevant photochemical reactions and model parameters. The major sources of O(^{1}S) in the dayglow are still assumed to be dominated by photoelectron impact on ground state O(^{3}P), dissociative recombination of O_2^+ with thermal electrons, photodissociation of O_2 by extreme ultraviolet (EUV) radiation below 133 nm, and energy transfer from N_2 ($A^3\Sigma_u^+$) itself excited by photoelectron impact on ground state N_2. The work of *Singh et al.* [1996a] attempted to model the WINDII observations with these mechanisms and additional sources related to three-body oxygen atom recombination and a potential previously overlooked source—namely, photodissociation of ground state O_2 by solar Lyman-α radiation at 121.6 nm which penetrates through the thermospheric window to below 90 km. The work also raised the possibility of an underestimation of the possible contribution made by soft solar X-rays in the 1.8–5 nm region and Lyman-β at 102.6 nm. Work continues on this topic.

7.2. The Dayglow O(^{1}D) Redline Emission

[84] The dayglow O(^{1}D) redline emission also remains incompletely understood to this day, but the work by *Singh et al.* [1996b] and again by *Witasse et al.* [1999] and *Culot et al.* [2004] using WINDII observations helped to resolve some important issues. In particular, this work placed constraints on the role played by the N(^{2}D) + O_2 reaction and the still-unconfirmed yield of O(^{1}D). Analogous to the dayglow O(^{1}S) green line, the recognized sources of O(^{1}D) are/were photoelectron impact on ground state O(^{3}P), dissociative recombination of O_2^+ with thermal electrons, the reaction of N(^{2}D) atoms with ground state O_2 with the N(^{2}D) atoms produced by photoelectron impact, and photodissociation and recombination of NO^+ ions. Additional recognized sources of O(^{1}D) were photodissociation of ground state O_2 and radiative cascade from dayglow O(^{1}S) discussed above.

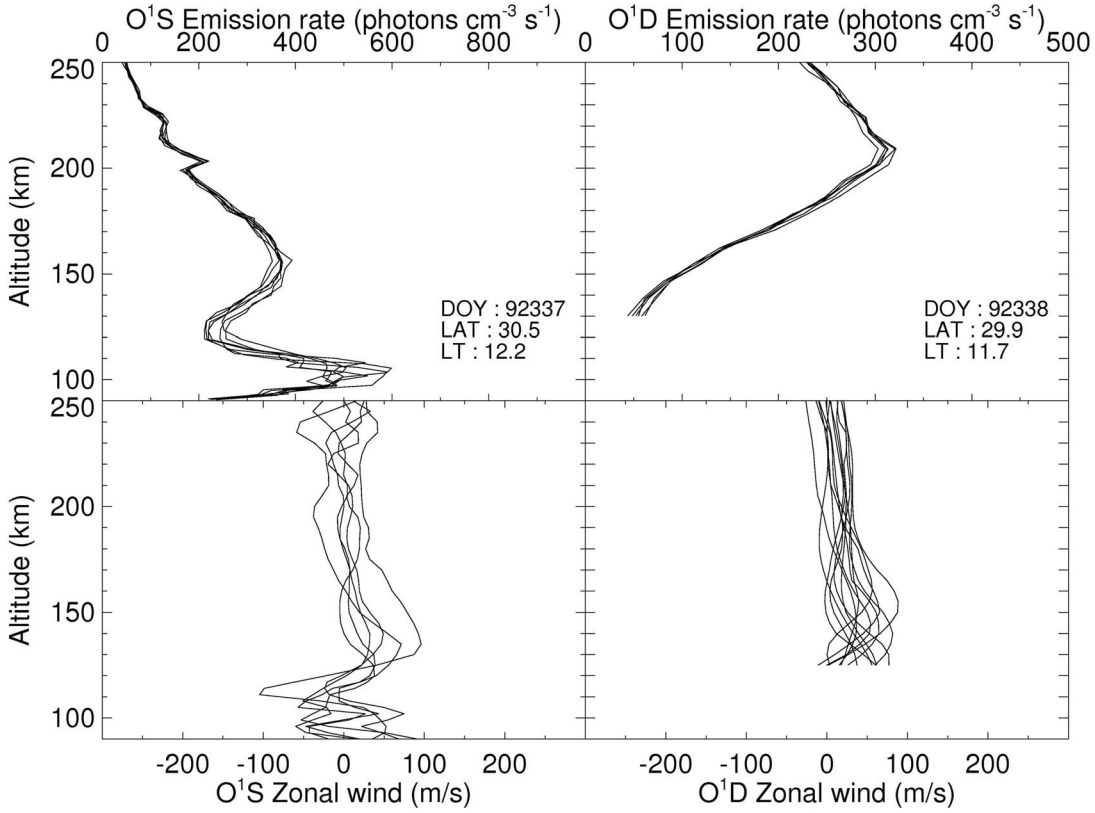

Figure 13. (top) Daytime volume emission rate profiles for (left) O(^{1}S) and (right) O(^{1}D). The multiple profiles are from the orbits of day 337 (2 December) and day 338 of 1992 as indicated. (bottom) The corresponding zonal winds for these successive days. The variability in the profiles is a result of longitudinal variations.

7.3. The Dayglow and Twilight $O^+(^2P)$ Emission

[85] The exploitation of the dayglow and twilight thermospheric emission of the $O^+(^2P)$ pair at 732 and 733 nm, as measured by WINDII, is somewhat different from those described above in that it used limb radiance measurements rather than processed volume emission rates. The limb radiance is essentially the volume emission rate integrated along the line of sight. The aim was to apply a method first suggested by *McDade et al.* [1991] to determine simultaneously thermospheric oxygen atom densities (and hence thermospheric/exospheric temperatures) and the highly variable EUV solar flux near 66.6 nm. The WINDII 732 nm limb radiances obtained simultaneously over a range of tangent heights were well suited for a modification of the *McDade et al.* [1991] approach. Although the WINDII field of view did not extend to the top of the $O^+(^2P)$ 732 nm volume emission profile, the method accommodated this and used the radiances observed at different tangent heights to retrieve the $O^+(^2P)$ unattenuated ionization frequency, designated I_∞; the atomic oxygen density, $[O]_{250}$, at an arbitrary reference altitude of 250 km; and the atomic oxygen exospheric-scale height, H_O, applicable above the 250 km reference pivot point. However, it was found that the filter function had to be corrected in order to obtain valid results. This correction has not been implemented in the routine WINDII processing.

[86] The photochemistry driving the daytime and twilight $O^+(^2P)$ 732 nm emission is quite similar to that described above for the neutral O(^{1}S) green line and the O(^{1}D) red lines. Details are provided in *McDade et al.* [1991, and references therein]. But the key driver is photoionization of ground state O(^{3}P) atoms by solar EUV radiation below a threshold wavelength of 66.6 nm. The total ionization frequency is therefore reflective of, and a potential proxy for, the highly variable solar flux values below this 66.6 nm threshold. The retrieval algorithm is more fully described by *Bacsek* [1998] and *McDade et al.* [1991]. Basically, a nonlinear Levenberg-Marquardt method is used to derive, using a forward photochemical and ionospheric model, the values of the three key geophysical parameters that control the $O^+(^2P)$ 732 nm radiances observed at any tangent height, location, and geophysical conditions. A single radiance observed at just one tangent height obviously cannot provide the sought-after triad of key parameters; I_∞, $[O]_{250}$, and H_O. However, simultaneous observations afforded by WINDII over a range of tangent heights allowed all three sought-after parameters to be independently determined. An important aspect of the work of *Bacsek* [1998] is that the derived $O^+(^2P)$ unattenuated ionization frequencies, I_∞, correlate better with the ground-based He I equivalent widths than the standard ground-based F10.7 cm fluxes normally used as proxies for the highly variable solar EUV

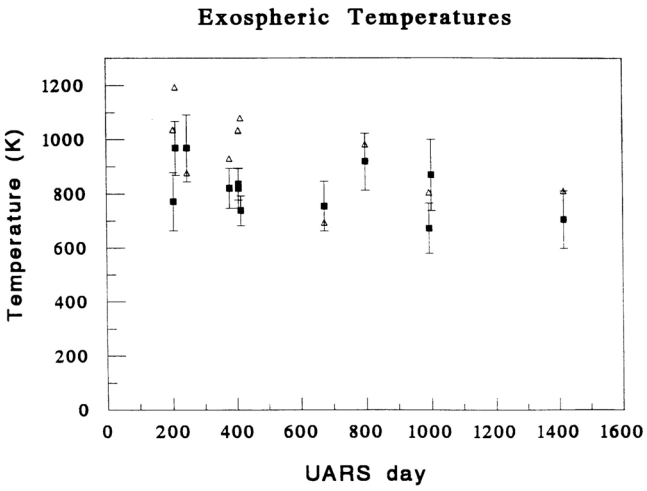

Figure 14. MSIS-86 (open triangles) and WINDII recovered (solid squares) exospheric temperatures versus UARS day number, 1 April 1992 to 26 July 1995. WINDII error bars encompass the error of the acceleration due to gravity, as well as the error in the recovered H_O.

flux below 66.6 nm. The exospheric temperatures selected from 12 days between 1 April 1992 and 26 July 1995 are shown in Figure 14.

7.4. The Nighttime Airglow Continuum and NO Densities

[87] The background nightglow WINDII observations made at 553 nm, in support of the nighttime O(^{1}S) green line measurements at nominally 558 nm, provided, perhaps unintentionally, a unique database on the global and temporal variation of what is known as the "green night airglow continuum." Over many years the origin of this emission has been questioned and extensively discussed. The current consensus is that in the 550 nm region the emission arises predominantly from the chemiluminescent NO + O reaction which proceeds via both a direct bimolecular reaction and a third body mediated recombination reaction into an excited state of NO_2 which promptly emits in the "air afterglow" continuum. Given that WINDII provided near simultaneous observations of both the nighttime O(^{1}S) green line volume emission profiles, from which atomic oxygen density profiles could be derived as explained in section 3, as well as airglow continuum volume emission rates, *von Savigny et al.* [1999] combined the oxygen atom densities derived from the O(^{1}S) green line measurements using the model and parameters of *McDade et al.* [1986a] and the measured 553.1 nm "continuum" observations to derive the local NO densities. The photochemical details of the chemiluminescent NO + O reaction are described in detail by *McDade et al.* [1986b]. The observed continuum volume emission rates are related to the ambient nitric oxide number densities, [NO], and the atomic oxygen densities, [O], via a simple product of the two and a temperature- and background density–dependent effective chemiluminescent bimolecular rate coefficient.

[88] *Von Savigny et al.* [1999] used the WINDII 553 nm continuum emission rates and near-coincident O(^{1}S) green line 558 nm volume emission rates to derive nitric oxide distributions between 90 and 105 km over local times ranging from 20:00 to 4:00 and latitudes between 42°S and 42°N for the period 10 November 1992 to 9 January 1993. More work on this is highly desirable to elucidate tidal effects and solar cycle variations. Figure 15 illustrates a sample contour plot of the zonally averaged derived nitric oxide number densities as a function of local time and altitude for the 24°S to 30°S latitude bin between 10 November 1992 and 9 January 1993.

7.5. The Stratospheric Airglow NO_2 Continuum

[89] In addition to the upper mesospheric and lower thermospheric NO_2 green continuum discussed above, a new airglow layer was discovered in WINDII data at night [*Evans and Shepherd*, 1996]. The STRATOGLOW (stratospheric airglow) is a chemiluminescent airglow layer in the stratosphere at 60 km originating from the ozone and nitric oxide reaction. The same chemical reaction was used in the balloon and aircraft stratospheric nitric oxide detector [*Ridley et al.*, 1992]. Altitude profiles of the STRATOGLOW airglow emission were obtained by *Evans and Shepherd* [1996] during UARS roll-down periods when the WINDII images were taken down to a lower altitude than normal. The upper part of the emission profile could be seen in normal operation with the lower edge of the field of view (FOV) at 70 km. The emission arises from the reaction of ozone with nitric oxide forming excited nitrogen dioxide:

$$O_3 + NO \rightarrow NO_2^* + O_2 \quad (8)$$

$$NO_2^* \rightarrow NO_2 + h\nu. \quad (9)$$

The airglow layer which originates in the stratosphere extends down to 45 km on occasion. Since ozone is easily

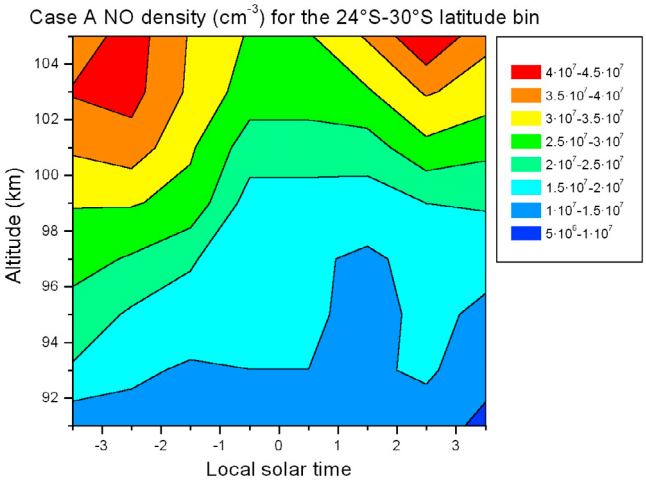

Figure 15. A sample contour plot of the nitric oxide densities as a function of local time and altitude for the 24°S to 30°S latitude bin derived from the WINDII 553 nm nightglow observations derived as described in the text and in more detail by *von Savigny et al.* [1999]. The "Case A" title refers to one of the photochemical models, the preferred model, as suggested by *von Savigny et al.* [1999].

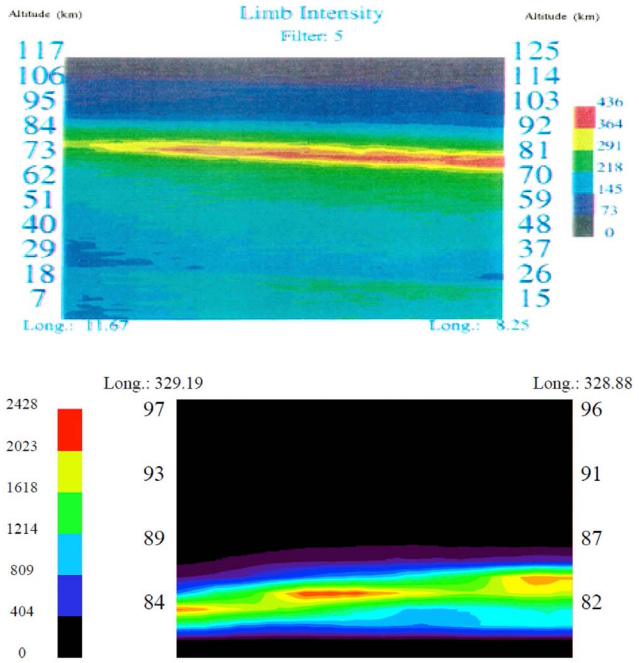

Figure 16. (top) View of polar stratospheric clouds illuminated by moonlight. PSCs are seen as the thin green strip at 19 km observed at 64.7°S latitude, 9.9°E longitude on 15 August 1994. (bottom) WINDII limb image of a PMC illuminated by scattered sunlight. Image taken at 67.7°S latitude, 329.1° longitude and local time 13:56. Note the three-wave structure typical of gravity waves with a wavelength of 50 km. The width of the image is 150 km and the altitudes are shown.

measured, this is a possible way to monitor NO at lower levels in the mesosphere and upper stratosphere. The spectrum of the glow extends from 600 nm to 1500 nm. The emission is similar to, but red-shifted relative to, the NO + O chemiluminescence discussed in section 7.4. The emission was most apparent in the WINDII channel 0 which had no blocking interference filter and was used to take star images for determination of the attitude transformation matrices and for calibration (the calibration lamps had their own filters).

7.6. The Anomalous Scattering of Sunlight Ascribed to PMCs, PSCs, and Aerosol

[90] Since WINDII is a CCD imager viewing through a Michelson interferometer, it can take excellent images of the limb of the atmosphere. An early application of this feature was the observation of polar stratospheric clouds (PSCs) in the Southern Hemisphere winter illuminated by moonlight when WINDII was rolled down so that the tangent height at the bottom of the image was below 0 km in the foreground of the limb FOV. Such a view of PSCs is shown in Figure 16 (top) [*Alfred*, 1999]. Similarly at midlatitudes, the stratospheric aerosol layer at 21 km was visible by moonlight. Using Stratospheric Aerosol and Gas Experiment (SAGE 2) aerosol profile data for training, an artificial intelligence (AI) program was developed to retrieve the aerosol altitude profiles from the WINDII moonlit images [*Sopoco*, 2001].

[91] Although the radiance is lower, numerous polar mesospheric clouds (PMCs) were detected in the day sunlit atmosphere at 83 km in both the Northern and Southern hemispheres [*Evans et al.*, 1995; *Evans and Chardon*, 2000]. The "Mie" scattering from the clouds clearly stands out above the Rayleigh scattering from the atmosphere. The morphology and radiance distributions were measured with the WINDII data. A three-satellite intercomparison of PMCs as measured from WINDII, POAM (Polar Ozone and Aerosol Measurement), and SME (Solar Mesosphere Explorer) [*Shettle et al.*, 2002] was conducted. The agreement was excellent as shown by the figures in that publication. The frequencies of occurrence were mapped for several years in both hemispheres. The frequencies of PMC altitude profiles were extensively investigated. The ice particle sizes were investigated from the angular dependence of the particle scattering. The PMC images also manifested the presence of gravity wave structures in PMCs with wavelengths around 50 km, as shown in Figure 16 (bottom).

[92] *Vergados and Shepherd* [2009] employed the CARMA (Community Aerosol and Radiation Model for Atmospheres) model to predict PMC scattering from the ice crystals simulated by the model. These were compared with the WINDII PMC observations and the water vapor profiles adjusted to match the model results with the observations. This provided an estimate of the water vapor content at the time of the WINDII observations. *Wiens et al.* [1995] presented WINDII observations made during a PMC breakup event as part of the Airborne Noctilucent Cloud (ANLC-93) campaigns.

7.7. Impact on the O(^{1}S) Airglow of a Solar Flare

[93] The authors consider the extensive daytime airglow data set to be unique to WINDII. It made possible the measurement of winds in the daytime, and it also provided much information on the thermosphere, as described in section 8. One of the many unexpected aspects was the observation of solar flares, as shown in Figure 17, which is a map of O(^{1}S) emission for 30 October 1992 during which a solar flare occurred while the Kp value was declining from a peak of 4 on 27 October. The enhancement was about 2000 photons cm^{-3} s^{-1}, more than doubling the normal volume emission rate. The flux of X-rays measured by a Geostationary Operational Environmental Satellite (GOES) from 0.1 to 0.8 nm wavelength increased from near-zero to a peak of 1.7×10^{-4} W m^{-2} during this time [*Maharaj-Sharma*, 2002]; the flux level was above 2×10^{-5} W m^{-2} from 17:00 to 21:00 UT, which corresponds to $-95°$ to $-160°$ longitude at $-20°$ latitude, and agrees well with the enhanced emission region in Figure 17. The modeling has not been done for this event, and these observations have not been published before. The F10.7 solar flux influence on the dayglow emission is described in section 8.

8. THERMOSPHERE DYNAMICS: SOLAR AND GEOMAGNETIC INFLUENCE AND NONMIGRATING TIDES

[94] The primary goal of UARS was to study the energy inputs, species concentrations and temperatures, and dynamics

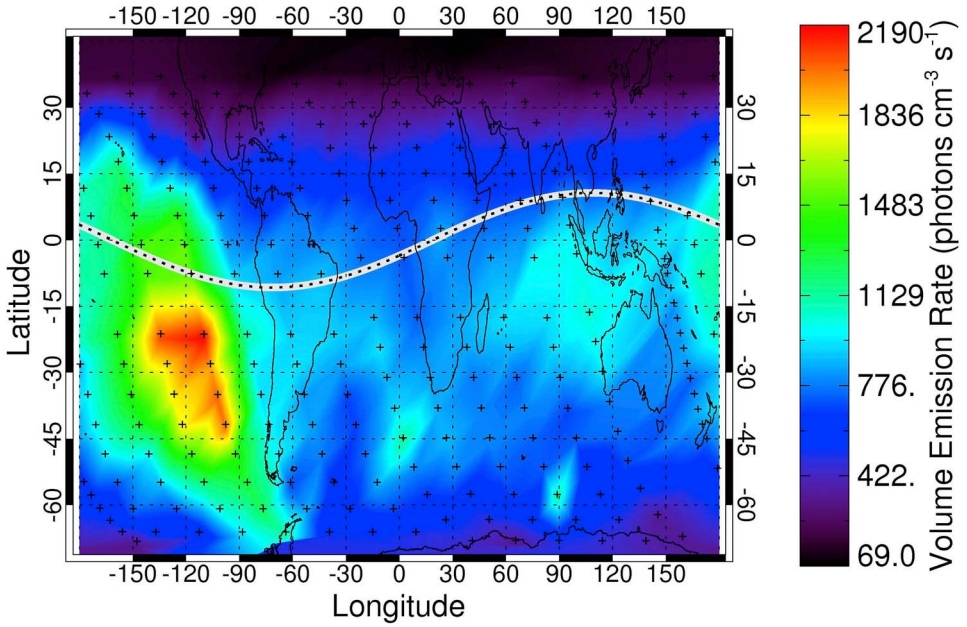

Figure 17. Latitude longitude map of O(^{1}S) volume emission rate at 100 km for 30 October 1992, during which a solar flare occurred. Universal time proceeds from the right to the left, and the solar flare produces an emission enhancement of over 2000 photons cm^{-3} s^{-1} late in the day, lasting for about 6 h. The magnetic equator is shown.

of the atmosphere between 10 and 110 km, and WINDII made major contributions toward this goal. However, it was evident from the beginning that the WINDII data above 110 km were also of great value. In particular, the WINDII baffle performed spectacularly well, providing airglow data in the daytime from 300 km down to about 90 km (as described in section 7) where the Rayleigh scattering became dominant (described in section 6). As shown in Figure 13, two peaks were found in the O(^{1}S) daytime emission that had never been delineated so clearly before [*Maharaj-Sharma and Shepherd*, 2004]. The upper (called the *F* region) peak near 150 km was found to vary systematically with the solar flux, the solar zenith angle, and geomagnetic activity. The lower peak was closely coincident with the nighttime O(^{1}S) airglow but was not the same. It was enhanced in emission rate and at a slightly higher altitude. These characteristics were investigated in more detail by *Zhang and Shepherd* [2005a], who formulated empirical relationships that described the airglow peak emission rates, altitudes, and widths as a function solely of the solar flux and the solar zenith angle. An earlier study [*Zhang and Shepherd*, 2004] accomplished the same for the O(^{1}D) emission.

[95] *Culot et al.* [2005] studied the geomagnetic influence on the *F* region O(^{1}S) and O(^{1}D) emissions and found that when the magnetic activity increased from quiet to strong, the altitude of the peak of both emissions increased by <10%, the peak emission rate of the O(^{1}S) thermospheric layer decreased by about 40%, and the peak emission rate of the O(^{1}D) layer remained almost constant. The effects of solar flux and solar zenith angle were removed from the data so that what was observed was the response solely due to geomagnetic activity, as indicated by Kp. The authors identify the larger O(^{1}S) response with a diminution of the $N_2(A^3\Sigma_u^+)$ + O process (see section 7.1), so it might be postulated that this is a result of the reduction in atomic oxygen concentration. The [O]/[N_2] ratio has been observed by *Meier et al.* [2005] and others to be reduced at high latitudes and increased at equatorial latitudes during geomagnetic storms.

[96] The solar influence on the nighttime O(^{1}S) emission has been more difficult to quantify as it involves the production and loss of atomic oxygen, making the process indirect and subject to strong dynamical influences. In particular, the seasonal variations of this emission tend to obscure the solar flux influence. However, a definitive description has more recently been presented by *Liu and Shepherd* [2008], in which from 300,000 emission profiles the data were deseasonalized and sorted by latitude. Having done this, the solar influence is clearly defined and an empirical model developed, giving the integrated emission rate (radiance) as a function of the F10.7 solar flux, the latitude in 10° latitude increments, and the season, defined by 3 month averages. The solar response increases with increasing latitude by a factor of 2 from the equator to 40° latitude.

[97] At night, the O(^{1}S) emission from the *F* region was absent, except near the geomagnetic equator. The O(^{1}D) emission was strong and clearly seen both in the daytime and at night and, in particular, in the intertropical arcs near the geomagnetic equator [*Thuillier et al.*, 2002] with a seasonal dependence of latitude on the meridional wind observed with WINDII. *Nicolls et al.* [2006] showed that the O_2^+ densities given by the International Reference Ionosphere (IRI) model are much higher than the densities produced by the

$O^+ + O_2$ reaction, which leads to predicted O(^{1}D) emission rates much higher than observed, by an order of magnitude at the equator. WINDII O(^{1}S) emission rates were used by these authors to show that the IRI model overestimates the O_2^+ densities on the bottomside of the *F*2 region, indicating a need for revision of the model.

[98] In the design stage of WINDII it was expected that auroral emissions would be observed in most of the WINDII channels. During the mission, auroral emission was seen at high latitudes above this lower layer [*Shepherd et al.*, 1996]; in a way, it is surprising the aurora was not more dominant, indicating the strength of the limb-viewed airglow. Nevertheless, the aurora was studied, during both daytime and nighttime. *Lee and Shepherd* [2007] removed the airglow component from the daytime data, using the empirical formulation of *Zhang and Shepherd* [2005a], and compared the residual auroral emission with energetic particle fluxes from the Defense Meteorological Satellite Program (DMSP) satellites; the energy flux during the nighttime was found to be greater than in the daytime, with the total electron energy flux increasing with increasing solar zenith angle from 40° to 160°. A strong anticorrelation was also found between the altitude of the peak emission rate and the average precipitating electron energy. *Wiens et al.* [1999] found WINDII enhancements of O(^{1}D) emission of 20 R between the altitudes of 250 and 270 km in the South Atlantic Anomaly region during magnetically disturbed periods.

[99] Twenty years after launch it was discovered that nonmigrating tides could be seen at 250 km in the daytime O(^{1}S) data. It is strange that they had been overlooked for so long as they are easier to detect than the migrating tides. This is because they can be seen as a function of longitude in the data for a single day; information on the local times is not required unless one wants to determine the propagation characteristics. Observation of the nonmigrating diurnal eastward propagating tide of wave number 3 (DE3), seen from a satellite at fixed local time as wave 4, was reported by *Shepherd* [2011] only very recently. Perturbations with amplitudes of about 10% were routinely seen within 20° of the equator. At 250 km in the daytime the dominant excitation process is photoelectron impact on atomic oxygen, and so knowing the solar flux the atomic oxygen concentrations can be determined. *Shepherd and Cho* [2011] normalized the proportionality constant to the Naval Research Laboratory Mass Spectrometer and Incoherent Scatter (NRLMSISE-00) model for 1 month and then made comparisons for other months, with encouraging results. *Talaat and Lieberman* [2010] had previously shown that wave 4 could be discerned in the WINDII data when the whole data set was used; they showed that it extended from the MLT region into the thermosphere.

[100] When polar plots were made of the emission rate, *Shepherd and Cho* [2011] found spiral patterns extending from high latitudes down to the equator. This is consistent with the observations of *Meier et al.* [2005] of the equatorward movement of the [O]/[N_2] ratio during major storms and requires equatorward and westward winds. The WINDII O(^{1}S) thermospheric winds around 250 km have been extensively studied by *Fejer et al.* [2000] and by *Emmert et al.* [2001, 2002, 2004]. These authors derive disturbance winds (differences from quiet time winds) as a function of geomagnetic latitude, geomagnetic local time, and Kp. For values of Kp approaching five, winds of several hundred meters per second are observed, easily sufficient to move atomic oxygen from the auroral region to the equator during 1 day. Thermospheric winds and their response to the interplanetary magnetic field had also been reported by *Richmond et al.* [2003]. They found patterns remarkably similar to the ionospheric convection pattern, even at altitudes as low as 108 km, where the amplitude was only 17% of the convection velocity. This value increased to about 60% at 125 km, reaching winds of 80 m s^{-1} at 200 km. *Zhang and Shepherd* [2000, 2002] studied the winds during the 4–5 April 1993 and February 1994 geomagnetic storms and found winds as high as 700 m s^{-1} at 180 km. At midlatitudes during quiet times, *Duboin* [1997] compared WINDII O(^{1}D) winds at altitudes between 250 and 260 km with results from the Saint-Santin incoherent scatter radar, showing a diurnal behavior pattern with poleward winds of about 50 m s^{-1} near noon and equatorward at about 150 m s^{-1} near midnight; the patterns were similar for all four seasons.

[101] Runs with the TIME-GCM (R. Roble, private communication, 2012) support the view suggested by the above results. Strong heating associated with the aurora generates vertical winds that loft atomic oxygen into the thermosphere, where it is carried by these large thermospheric winds down to equatorial latitudes. WINDII is able to contribute valuable information with the potential of developing this picture in more detail.

[102] Very recently, *Shepherd and Shepherd* [2011] reported thermospheric perturbations associated with SSW, in particular the warming of February 1993. Using the O(^{1}S) dayglow emission and normalizing against the empirical values of *Zhang and Shepherd* [2005a], it was found that there was a depletion in the emission rates above 140 km which commenced around the onset of the SSW and lasted over a period of 3–4 days before returning to and exceeding the pre-SSW values during the SSW recovery phase.

9. WHAT WAS ACCOMPLISHED

[103] The accomplishments of WINDII are the subject of this paper and have been described in some detail. In this section it is appropriate simply to summarize them and make some overall comments. The summary is presented in Table 3, along with corresponding references.

[104] WINDII was a major technological success. The UARS mission proved that a "solid" Michelson interferometer fabricated from cemented glass components was sufficiently robust to survive launch and was able to measure winds on orbit by measuring the interferogram phase using piezoelectric mirror stepping. Moreover, the instrument was field-widened with excellent thermal compensation over a spectral range from 531 to 786 nm, which allowed wind determination from a range of airglow emissions. The instrument was extremely stable with phase calibrations

TABLE 3. Summary of WINDII Accomplishments

Accomplishment	References
The WINDII "solid" Michelson interferometer fabricated from cemented glass components survived launch and measured winds on orbit from the interferogram phase using piezoelectric mirror stepping.	*Gault et al.* [1996a], *Shepherd et al.* [1993a]
WINDII was field-widened with excellent thermal compensation over a spectral range from 531 nm to 786 nm. It was extremely stable with phase calibrations made every 20 min, requiring only modest temperature control of 1 K.	*Hersom and Shepherd* [1995], *Thuillier and Shepherd* [1985], *Thuillier et al.* [1998]
The WINDII optical system suffered no measurable degradation during 12 years of operation on orbit, as monitored by a stable onboard calibration system.	*Thuillier et al.* [1998]
The baffle was key to making measurements in the daytime, providing 24 h of local time coverage in the altitude range 90 to 120 km, allowing the migrating tides to be quantified and dayglow emission to be observed.	*Gault et al.* [1992], *McLandress et al.* [1994, 1996a], *Shepherd et al.* [1993a], *Zhang and Shepherd* [2005a]
Together with HRDI, WINDII defined the dynamics of the MLT in terms of the migrating tides, planetary waves, and mean winds, and later the nonmigrating tides as well.	*Burrage et al.* [1997], *McLandress et al.* [1996b], *Zhang and Shepherd* [2005b], *Zhang et al.* [2001, 2007], *Fauliot et al.* [1997]
The CCD detector made it possible to observe extremely weak nightglow emission, leading to an understanding of the influence of the observed dynamics on atomic oxygen concentrations.	*Liu and Shepherd* [2006a], *Liu et al.* [2008] *Russell and Lowe* [2003], *Russell et al.* [2004, 2005], *Shepherd et al.* [1995, 1998], *Ward* [1999]
WINDII as an imager observed the solar influence on airglow both day and night and the solar flare impact on the dayglow.	*Liu and Shepherd* [2008], *Maharaj-Sharma and Shepherd* [2004], *Witasse et al.* [1999], *Zhang and Shepherd* [2004, 2005a]
The excellent baffle performance also allowed the determination of mesospheric temperature from Rayleigh scattering	*Evans et al.* [1994a, 1994b], *M. G. Shepherd et al.* [1997, 2001, 2004a, 2004b, 2005, 2006, 2007, 2008], *Shepherd and Fricke-Begemann* [2004]
WINDII measurements extended into the thermosphere, allowing winds and emission rate to be observed there.	*Emmert et al.* [2001, 2002, 2004, 2008], *Richmond et al.* [2003], *Shepherd* [2011], *Thuillier et al.* [2002]
Polar mesospheric clouds were observed in an imaging mode but also in normal operations.	*Evans et al.* [1995], *Shettle et al.* [2002], *Vergados and Shepherd* [2009], *Wiens et al.* [1995]
Auroral emission rate profiles were observed both in the daytime and at night, allowing auroral excitation and the influence of geomagnetic disturbances to be studied.	*Culot et al.* [2005], *Lee and Shepherd* [2007], *Shepherd et al.* [1996], *Zhang and Shepherd* [2000, 2002]
$O^+(^2P)$ and $O(^1S)$ emissions leading to thermospheric atomic oxygen concentrations were observed.	*Bacsek* [1998], *Shepherd and Cho* [2011]
Lower thermospheric NO concentrations were derived from the NO_2 continuum emission.	*von Savigny et al.* [1999]
Stratospheric airglow arising from the NO_2 continuum was observed.	*Evans and Shepherd* [1996]
Polar stratospheric clouds and aerosol were observed.	*Alfred* [1999], *Sopoco* [2001]
WINDII made a contribution to wind models.	*Drob et al.* [2008]

required only every 20 min, requiring only modest temperature control of 1 K. The CCD imager, relatively new in space instruments at that time, performed to perfection. The WINDII optical system suffered no measurable degradation during 12 years of operation on orbit, as monitored by a stable onboard calibration system, exceeding the requirements by a wide margin. The baffle was key to making measurements in the daytime, which was possible down to 70 km; its performance far exceeded expectations and greatly expanded the scope of the science. All of this was possible only because the UARS was a 5900 kg spacecraft, large enough to accept nine instruments with essentially no constraints in mass or volume. In addition, the precise orientation stability allowed instrument pointing to an accuracy of 1 km or better. In this sense it was a unique scientific spacecraft.

10. WHAT WAS NOT ACCOMPLISHED

[105] The WINDII project was very ambitious in its science objectives. There were fifteen Science Team members, and each had their own aspirations and objectives. All three agencies involved, the Canadian Space Agency, the Centre National d'Etudes Spatiales, and NASA, were all extremely generous and supportive, and met all requests put forward by the Team to the fullest extent possible. The result was an instrument capable of making many different measurements. Although the primary goal, and the reason for acceptance by NASA, was the measurement of winds, it was evident from the beginning that many other atmospheric characteristics could be measured with WINDII and these all appeared on the "wish list" of the team. There were two limitations that could not be overcome: (1) the data rate for WINDII was limited to what was originally requested, i.e., 2 kbits s^{-1}, and (2) there were only 24 h available each day! WINDII had a single imaging detector, and the different emissions were recorded sequentially through the stepping of a filter wheel.

[106] To meet the primary goal of wind measurement, the Team wanted to cover the maximum altitude range, and this required the use of more than one filter. The atomic oxygen $O(^1S)$ emission covered from 90 to 250 km during the daytime but only 90 to 120 km at night. The nighttime range could be extended down to 80 km using the OH emission, but the OH winds turned out to be of lower quality than those from $O(^1S)$ and were never validated. The winds could in principle be extended upward at night using the $O(^1D)$ emission and obtained lower in the daytime using the O_2 Atm emission. But because these emissions would have to be measured in sequence, the cycle time would have to be lengthened, degrading the horizontal resolution. Ultimately,

it was decided that the horizontal resolution was a priority and that the number of different emissions observed should be minimized on a single day. Thus, on some days, the O(^{1}S) emission was observed for the entire day (filter changes were still necessary to observe background emission and conduct phase calibrations). However, the OH emission was observable only at night, so on the days for its observation, it was paired with O(^{1}S), observing the latter during the daytime portions of the orbits. The O_2 Atm emission was observable both day and night and it was run by itself for a full 24 h, but the wind data were never validated. The O(^{1}D) thermospheric emission was considered of lower priority because the overall middle atmosphere goals of UARS extended up to only 110 km, but the emission was valuable both day and night and so could be run for a full 24 h. Thus, the most common format for a week of observations was 2 days of O(^{1}S) only, 2 days of O_2 Atm only, 2 days of O(^{1}S) during daytime and OH at night, and one full day of O(^{1}D). The O^+ 732 nm emission was observed occasionally, usually as O^+ during the day and O(^{1}D) at night. Late in the mission, when continuous observations no longer became possible because of power limitations, the observations were restricted, almost exclusively, to O(^{1}S).

[107] Prior to launch, the Team was not confident of how well the baffle would perform, as it was impossible to test on the ground, and therefore was not sure of daytime observations below about 100 km. However, after launch it proved possible to see down into the Rayleigh scattering as far as 70 km; providing Rayleigh scattering temperatures. This was fortunate, since as described earlier, the Doppler and rotational temperature methods did not perform well. The Rayleigh scattering observations did not require any operations changes as normal images from the background levels were used. Similarly, PMC observations were possible, but these required higher-resolution images, at 2 × 5 pixels (roughly 2 km high and 5 km wide), and did require special operations. During the PMC season, these were inserted into the orbit schedule at PMC latitudes, every second orbit. There was a problem in this owing to the UARS "frozen" orbit, in that the spacecraft altitude was always higher in the Southern Hemisphere than in the Northern Hemisphere. In order to observe PMC in the Southern Hemisphere, at about 82 km, it was necessary to roll the spacecraft down slightly to accommodate it—a consequence of the fact that WINDII was hard-mounted to the spacecraft, with no adjustment. The UARS Operations staff was very accommodating in making this possible. On the other hand, WINDII suffered the consequences when, for short periods of time, the spacecraft rolled up, although this allowed WINDII observations of the upper thermosphere, and again when the spacecraft was rolled down, allowing observations of the stratosphere, but ruling out normal operations in both of these modes.

[108] As described earlier, WINDII viewed to the side of the spacecraft in order to view common volumes of atmosphere orthogonally with the two fields of view. It also limited the observations to two local times on a given day (one for the ascending portion of the orbit at a given latitude and the other for the descending portion). HRDI, with a pointing telescope, could look on either side of the spacecraft, yielding observations at two different local times all around the orbit. Another consequence, not so obvious, and left as an exercise for the reader, is that while observations between 42°S and 42°N were made on both ascending and descending orbits on all days, yielding in general one daytime and one nighttime orbit, at latitudes higher than this, going to 72°, all the observations were in daytime. For this reason, tidal studies were limited to between 42°N and 42°S. The high-latitude daytime observations turned out to have an advantage, as it made possible regular wind observations between 90 and 250 km at high latitudes, available 4 days per week in daytime, with the nominal schedule described above. It also made frequent observations of daytime PMC possible, as well as Rayleigh scattering temperatures. All of this happened only because of the high-quality performance of the baffle. The WINDII observations of dayglow and scattered sunlight are unique and have revealed much about the thermosphere that was not envisaged before the launch.

[109] The measurement of temperature turned out to be much more difficult than for winds for a Doppler instrument. The observed temperature biases for both the O(^{1}S) and O(^{1}D) emissions have not been explained; the most likely explanation seems to be a nonthermal velocity distribution, but it could also be the result of incorrect background subtraction. Rotational temperatures are known to be of higher accuracy but were not successful here, either because of the sequential viewing of the different rotational lines, or because of an inadequate knowledge of the filter passbands—in spite of very careful measurement on the ground.

[110] In summary, the value of routine and continuous observations of winds over a defined altitude range was not fully appreciated prior to launch, in part because it was not thought that tidal observations would be possible. On the other hand, employing such a restrictive goal in advance would have eliminated the many other observations that turned out to be possible. One can imagine designing an imaging instrument that would simultaneously observe the entire altitude range accessible to airglow, but it would be a complex instrument. Decisions have to be made; the WINDII Team choices ruled out certain types of observations but made others possible.

11. FUTURE PROSPECTS FOR WIND MEASUREMENTS

[111] Following the proven on-orbit success of WINDII, other variants of the instrument have been considered. One weakness of the WINDII method is that with sequential phase stepping, any temporal or spatial changes in the target have an impact on the observed interferogram. This turned out not to be a problem with WINDII, most likely because small-scale structures such as gravity waves averaged out over the limb integrating path of roughly 300 km. *Gault et al.* [1996c] suggested a method of eliminating this problem. One of the Michelson mirrors is divided into quadrants and each quadrant is coated separately, so the path difference varies by about $\lambda/4$ from one quadrant to another. An image

of the mirrors is formed outside the interferometer, where the light from the quadrants is diverted in different directions, and four separate images of the field of view are formed, one for each quadrant. For a given direction in the field of view, the fringe is sampled at four points on the interferogram separated by $\lambda/4$, and from these four intensities, the phase of the fringe is calculated. This method has the advantage that no moving mirror is required to sample the interferogram. However, the four intensities used to determine the phase of the fringe are sampled by four different pixels, and the radiometric calibration of each quadrant must be done carefully. The WINDII CCD proved to be very stable over the lifetime of UARS, and the broad band source provided on-orbit white light calibrations, so this is not expected to be a serious drawback but would have to be considered carefully in the instrument design.

[112] By combining this four-quadrant method with the multiple-line approach used for the O_2 measurements for WINDII, a new measurement approach for using closely spaced emission lines in molecular bands was developed. This approach was used for instruments proposed for wind measurements from the stratopause to lower thermosphere [*Ward et al.*, 2001] using emission lines in the O_2 Infrared Atmospheric band at 1.27 microns. Because of the branch structure within the band, sets of emissions can be chosen with considerable sensitivity to temperature and accurate rotational temperature measurements can be made. This band is intense enough that the accuracy of the wind measurements is limited by the knowledge of the spacecraft parameters and not by any aspects of the measurement. This approach is also applicable to wind measurements on Mars and Venus, where the same bands are also present, and an instrument concept for observation of planetary winds on these planets has also been proposed [*Ward et al.*, 2003].

[113] A new concept for wind measurement, the Doppler Asymmetric Spatial Heterodyne (DASH) interferometer, has been developed by *Englert et al.* [2007] which may be considered a hybrid DMI and SHS (spatial heterodyne spectroscopy) instrument. The SHS is similar to a Michelson except that the mirrors are replaced by gratings, tilted off-axis, and the localized fringes are imaged onto an array detector. This effectively heterodynes the interferogram about a selected reference wavelength, the grating Littrow wavelength, yielding a low spatial frequency fringe which is easy to measure. The interferometer has no moving parts, even in the field-widened configuration, and provides high spectral resolution and high throughput over a limited spectral range. The DASH configuration is like the DMI in that one arm is longer than the other, creating a large optical path difference, but still retains the characteristics of the SHS. This allows the DASH to sample a much larger path difference interval than a DMI and observe a larger range of wavelengths. The most important advantage over WINDII is that the phases of several lines can be measured simultaneously in time, not sequentially, including that of the calibration line. On the other hand, only one-dimensional imaging is possible with the DASH approach; with phase stepping WINDII can obtain true two-dimensional wind images, although this was not done on UARS, in part because of the limited telemetry rate, but also because of signal-to-noise ratio. In general, a SHS or DASH can be tuned to operate in any spectral region, and it is possible to control the trade off between spectral resolution and bandwidth.

[114] *Harlander et al.* [2010] describe the design and fabrication of a DASH interferometer to measure upper atmospheric wind and temperature by observing the oxygen red line at 630 nm, the same as one of the WINDII emission channels. The instrument is fabricated as a monolithic interferometer using a Koster's prism as the beam splitter and is thermally compensated. Thermal drifts in all interferometers pose a challenge; however, a DASH interferometer can measure a calibration line (at rest relative to the interferometer) at the same time as observing the Doppler shifted atmospheric line. This allows any thermal drifts in the instrument to be monitored and then corrected in data processing. This design could be easily adapted to observe some of the other WINDII emissions. In particular, several spectral lines in either the O_2 or OH emission channels could be observed, potentially providing multiple-phase measurements as well as rotational temperatures.

[115] The remarkable success of WINDII stimulated thinking about measuring winds in the stratosphere, over the altitude range 20–45 km. There is no airglow in this region to use as a Doppler target, so thermal infrared emission would have to be used. After a lengthy study, a suitable line in the ozone spectrum was identified at 1133.4335 cm^{-1}, about 8.8 μm. This would allow ozone concentrations to be measured as well as the winds that transport them. However, the implementation would be more challenging than for WINDII, as infrared-transmitting materials would have to be used and the interferometer would have to be cooled to reduce the thermal emission of the instrument to levels below that of the atmospheric signal. A concept for an instrument called SWIFT (Stratospheric Wind Interferometer For Transport studies) was developed [*G. G. Shepherd et al.*, 2001]. An additional challenge is that the WINDII concept works only if the target emission consists of just one narrow line. Since the ozone spectrum is complex, it proved to be difficult to develop a narrow-band filter for this spectral region that would isolate the selected line and did not require very tight temperature control.

[116] This made DASH a strong candidate for the SWIFT instrument in that the necessity to isolate a single ozone line would not be required since several lines could be accommodated within the spectral range of a broader filter. The Canadian Space Agency recently gave York University a contract to build a developmental model of such an instrument. The instrument designed looks like WINDII in that it has an extra length of glass (zinc selenide) in one arm of the interferometer, and gratings separate the different wavelengths as in SHS. The true spectrum cannot be calculated from the DASH truncated interferogram, but that is not required; all that needs to be accomplished is to determine the phases of each wave component. One major advantage of the SHS/DMI approach is that the phase calibration line

and the atmospheric lines can be simultaneously measured across the entire field of the instrument, since they appear as different Fourier components. This would be implemented by using a gas cell, containing either N_2O or NH_3, covering the entire field of view. There is no need to remove the cell from the field of view so that it can be permanently in place. To date, an interferometer design has been achieved that meets the requirements for the wind measurements as defined for the original SWIFT. The monolithic interferometer, built by LightMachinery, Ottawa, has ZnSe optical elements connected together by hollow spacers of BK7 glass; these two materials have very similar thermal expansion coefficients. The design gives a spectral resolution of 0.23 nm (0.029 cm^{-1}), which means that spectral lines of spacing greater than this can be resolved in the analysis with a spectral range of 6 nm (0.774 cm^{-1}). Laboratory work is underway to further characterize the SWIFT-DASH interferometer.

[117] The WINDII DMI performed extremely well and has proven space heritage. There are a few changes to the current WINDII design that would provide improvements and position a WINDII-type instrument as the best choice for certain observations. It would be relatively straightforward to enlarge the field of view and employ a larger, modern CCD. If the data bandwidth could be provided by the spacecraft, then the full thermospheric-mesospheric altitude range could be covered in one image. Modern CCDs have very low dark current and readout noise, so it may also be possible to do true 2-D imaging of the limb. With a larger CCD it would also be possible to employ a split filter, similar to the one used on WINDII, for the OH background and measure the background as well as the target emission line in the same image. This would increase the number of observations and therefore improve coverage. As discussed earlier, a consistent and continuous set of observations would allow a much better determination of the tidal and wave structure.

12. CONCLUDING SUMMARY

[118] The WINDII project has demonstrated that, using the DMI approach, winds can be accurately measured in space from the phase shifts of interferograms generated by a Michelson interferometer. Moreover, it demonstrated the feasibility of fabricating a "solid" interferometer, in which phase stepping was accomplished using piezoelectric spacers and phase stability was achieved using a combination of cemented glasses that at the same time provided field widening. The field widening made it possible to image the limb, obtaining altitude profiles in single images and providing the capability of working at very low light levels. Winds were measured in the MLT during nighttime, from about 90 to 120 km, and in daytime up to 250 km, providing a climatology of the dynamics of this region, including mean winds; migrating tides; planetary waves; gravity waves; and recently, nonmigrating tides. At the same time, the high-quality airglow imaging observations demonstrated dramatically the very strong influence of the dynamics of this region on its species concentrations and their variations; in particular, the atomic oxygen concentrations were characterized in the MLT region and the middle thermosphere.

[119] Doppler temperatures were measured and found to track the currently accepted temperatures, but with a bias that has not been explained. It is thought that this indicates slightly nonthermal excited atomic oxygen distributions in regions where it is not expected; this requires further study. However, this would not affect the measurement of Doppler winds except in conditions of extreme anisotropy. Scale height temperatures were acquired, however, using Rayleigh scattering in the mesosphere and atomic oxygen in the thermosphere.

[120] The imaging capability was demonstrated in the acquisition of PMC images at high resolution (1 $\times$ 5 km), but the time allocated for this was limited. Nevertheless, more could be achieved with the existing body of data. The spectral coverage allowed background filters to be used to measure the green night airglow continuum observed in the mesosphere and also in the stratosphere. Polar stratospheric clouds were observed under lunar illumination and aerosol scattering as well. The $O^+(^2P)$ 732 nm emission was observed, and although it is contaminated, the potential was shown to exist to retrieve valid emission data, and from that, atomic oxygen concentrations. It remains on the list of things to be done.

[121] WINDII is a true imager in the sense that a wind can be measured from every pixel. In practice, the benefit obtained from this capability was limited, because of signal-to-noise limitations, and in any case because of the low data rate. The Level 1 data were acquired in six columns across the image, each 25 km wide, but these were combined into single profiles in the Level 2 processing. There is undoubtedly a wealth of data remaining in the Level 1 data that has not been exploited to date. One unusual example was discovered by *Lee and Shepherd* [2010]. In looking at $O(^1S)$ daytime low-altitude Level 1 images, they found occasional bins with high emission rate, having perfectly sinusoidal interferograms with very large phase shifts, large enough to correspond to supersonic winds. It was originally thought that these arose from dayglow over the sky being Rayleigh scattered as this would reflect very different components of the spacecraft velocity. However, this scattering could not be as large as observed, so such winds appear to exist sporadically, occurring only in summer at high latitudes. It was postulated that they could arise from strong electric fields associated with lightning events.

[122] Now, 20 years after the WINDII launch, there is still value in future data processing as the WINDII measurements have not yet been duplicated. It is expected that WINDII data will continue to provide new insights in the years ahead. This is illustrated by Figure 18, which is the latest result from WINDII, not yet published. It shows the longitudinal variation of the $O(^1D)$ volume emission rate at 250 km (squares) and the zonal wind (asterisks) derived from the same emission at the same altitude. Both show a wave number 4 pattern that is understood to be associated with the diurnal eastward propagating nonmigrating tide of wave

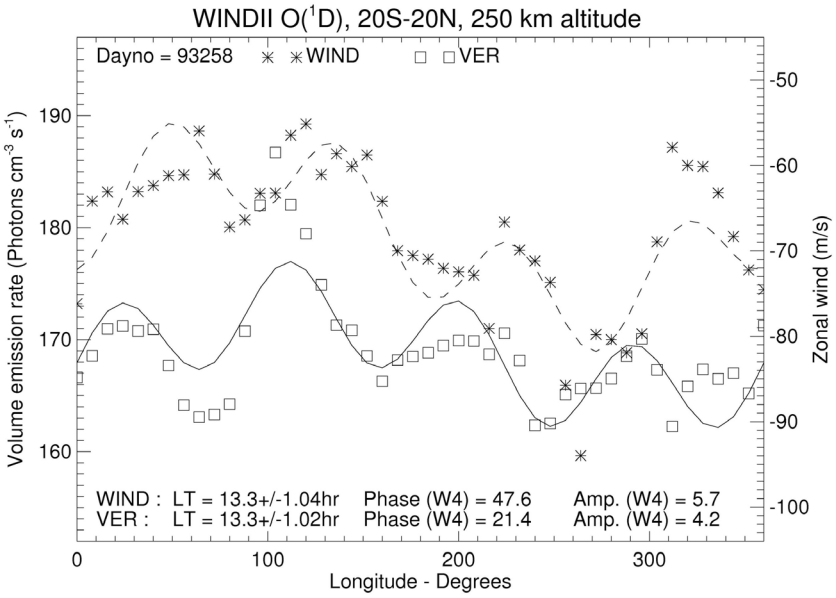

Figure 18. Longitudinal variations of O(^{1}D) volume emission rate (squares) for 15 September 1993, day 258, and of zonal wind (asterisks). Both have been fitted with a wave 1 and wave 4 variation, shown as a solid line for the emission rate and a dashed line for the wind. The local times, phases (degrees of longitude), and amplitudes of the wave 4 component are shown at the bottom of the figure. The wave 4 is prominent with the wind delayed in phase by about 26° of longitude.

number 3 (DE3). The wave 4 pattern is what is seen from a satellite fixed (during 1 day) with respect to the Sun, generating an additional wave because of the Earth's rotation. Figure 18 shows a small phase shift between the volume emission rate and the zonal wind. Indeed, there is more to be accomplished.

[123] **ACKNOWLEDGMENTS.** The authors, on behalf of the Science Team, express their sincere gratitude for the magnificent support provided by their respective sponsoring agencies, the Canadian Space Agency, the Centre National d'Etudes Spatiales, and the National Aeronautics and Space Administration, for what was a truly incredible mission. The Canadian and French teams built a unique and splendid instrument, but it was able to perform only because of the marvelous UARS platform provided to it. In particular, the NASA Operations Team is to be thanked for their tremendous support. The members of the original WINDII Science Team were Gordon Shepherd, Brian Solheim, and Bill Gault (York University); Gérard Thuillier, Alain Hauchecorne, and Michel Hersé (Service d'Aéronomie du CNRS); Sushil Chandra (NASA Goddard Space Flight Center); Leroy Cogger, (University of Calgary); Marie-Louise Duboin (CRPE/CNET, Issy les Moulineaux); Wayne Evans (Trent University); Dick Gattinger (National Research Council of Canada); Chantal Lathuillère (Laboratoire de Planétologie, UJF/CNRS); Edward Llewellyn (University of Saskatchewan); Hector Teitelbaum and Francois Vial (Laboratoire de Météorologie Dynamique, Palaiseau); and Robert Lowe (University of Western Ontario). In addition, the following individuals, listed by institution, are warmly acknowledged and thanked for their dedicated contributions to the WINDII Project: Henry Buijs and Sean Johnston (ABB Bomem); Allan Churgin, Susan Brune, John Ohrt, Lee Matheson, Susan McCall, Dave Harvie, Charlene Lau, Diane Zubac, and Carmen Walker (AIT); O. Peillet (BERTIN, Aix les Milles); Tom Darlington, Bob Gruno, Bob Hum, Steve MacLean, Jack Matsushita, and Barry Wetter (Canadian Space Agency); Patrick Charlot, Jean-Louis Fellous, Claude Fratter, Francoise Girod, Thierry Guinle, Georges-Henri Mingot, Nicole Papineau, Jean-Pierre Thouvenin, and Maurice Winterholer (Centre national d'études spatiales–CNES); G. Azria, Ludovic Bourg, Jean-Francis Brun, Vincent Fauliot, and Francois Leblanc (Service d'aéronomie du Centre national de la recherche scientifique–CNRS); Mike Atlas, Nino Bascelli, John Beck, Margaret Bishop, Bob Brown, Ron Buckingham, Bev Christie, Tan Dang, DonnaLee Desaulniers, Dave Friberg, John Giurgevich, Joe Gore, John Graham, Charlie Hersom, Dan Moffatt, Nancy Mulvihill, John Newnham, Tory Payne, Louis Piché, Paul Proulx, Chris Pye, Doug Reid, Glen Sellar, Randy Shelly, Bob Shmidt, Ken Smith, Gabriel Warshaw, and Dave Wilmut (COM DEV Ottawa (then CAL Corporation)); Ken Cross, Tim Eastland, Mike Faulkner, John Huva, and William Ward (Hierogram Associates); Frederic Culot, and Bruno Lamballais (Laboratoire de Planétologie, UJF/CNRS); Jeff Wimperis (Light-Machinery (formerly Interoptics)); F. Pasternak (MATRA-ESPACE (Toulouse)); George Dobrowolski and Ian Powell (National Research Council of Canada); J. M. Alunni (Quantel); Ken Kosteniuk, Doug Miller, and Zygmunt Pasturczyk (SED Systems); Jerome Alfred, Laurent Chardon, Paul Goodnason, Larry Laframboise, and Mary Jane Pilgrim (Trent University); Christina Azpiazu, Brian Jackel, and Alfredo Louro (University of Calgary); Ayoub Ali, Ron DeSerrano, Kathleen Gilbert, Lisa LeBlanc, Stella Melo, Vladimir Perminov, Nikolai Pertsev, Jason Russell, and David Turnbull (University of Western Ontario); Jean Lilensten (LPG), Michel Menvielle (CETP), and Olivier Witasse (LPG) (Other French Collaborators); Barbara Emery (HAO), John Emmert (NRL), Bela Fejer (USU), Marvin Geller (SUNY), Art Richmond (HAO), and Valery Yudin (SUNY) (Other U.S.A. Collaborators); and Sheldon Bacsek, Vin Bhatnagar, Stephen Brown, Colin Climie, Colin Hines, Tai-Yin Huang, Young-Sook Lee, Guiping Liu, Rawatee Maharaj-Sharma, Charles McLandress, Bob Peterson, Boedijanti Reid, Nayyer Siddiqi,

Alain Soltesz, Christian von Savigny, Chin Tai, Xiaoqi Wang, Rudy Wiens, and Shengpan Zhang (York University).

[124] The Editor on this paper was Mark Moldwin. He thanks two reviewers, Rick Niciejewski and Gary R. Swenson.

REFERENCES

Alfred, J. M. (1999), Analysis of polar stratospheric cloud observations with the WINDII Instrument on UARS, MS thesis, Trent Univ., Petersborough, Ont., Canada.

Andrews, D. G., J. R. Holton, and C. B. Leovy (1987), *Middle Atmosphere Dynamics*, pp. 226–235, Academic, San Francisco, Calif.

Bacsek, S. (1998), Thermospheric atomic oxygen densities and temperatures from WINDII observations of the O^+ (^2P) emissions, MS thesis, Grad. Program in Earth and Space Sci., York Univ., Toronto, Ont., Canada.

Baker, D. J., and J. A. T. Stair (1988), Rocket measurements of the altitude distributions of the hydroxyl airglow, *Phys. Scr.*, *37*, 611–622, doi:10.1088/0031-8949/37/4/021.

Barnett, J. J., and K. Labitzke (1990), Climatological distribution of planetary waves in the middle atmosphere, *Adv. Space Res.*, *10*, 63–91, doi:10.1016/0273-1177(90)90387-F.

Bhattacharya, Y., G. G. Shepherd, and S. Brown (2004), Variability of atmospheric winds and waves in the Arctic polar mesosphere during a stratospheric sudden warming, *Geophys. Res. Lett.*, *31*, L23101, doi:10.1029/2004GL020389.

Bouchareine, P., and P. Connes (1963), Interféromètre a champ compensé pour spectroscopie par transformation de Fourier, *J. Phys. Radium*, *24*, 134–138.

Bruinsma, S., F. Vial, and G. Thuillier (2002), Relative density variations at 120 km derived from tidal wind observations made by the UARS/WINDII instrument, *J. Atmos. Sol. Terr. Phys.*, *64*, 13–20, doi:10.1016/S1364-6826(01)00096-7.

Bruinsma, S., G. Thuillier, and F. Barlier (2003), The DTM-2000 empirical thermosphere model with new data assimilation and constraints at lower boundary: Accuracy and properties, *J. Atmos. Sol. Terr. Phys.*, *65*, 1053–1070, doi:10.1016/S1364-6826(03)00137-8.

Burrage, M. D., N. Arvin, W. R. Skinner, and P. B. Hays (1994), Observations of the O_2 atmospheric band nightglow by the high resolution Doppler imager, *J. Geophys. Res.*, *99*, 15,017–15,023, doi:10.1029/94JA00791.

Burrage, M. D., et al. (1996), Validation of mesosphere and lower thermosphere winds from the high resolution Doppler imager on UARS, *J. Geophys. Res.*, *101*, 10,365–10,392, doi:10.1029/95JD01700.

Burrage, M. D., W. R. Skinner, and P. B. Hays (1997), Intercalibration of HRDI and WINDII wind measurements, *Ann. Geophys.*, *15*, 1089–1098, doi:10.1007/s00585-997-1089-8.

Chahine, M. T. (1972), A general relaxation method for inverse solution of the full radiative transfer equation, *J. Atmos. Sci.*, *29*, 741–747, doi:10.1175/1520-0469(1972)029<0741:AGRMFI>2.0.CO;2.

Chapman, S., and R. S. Lindzen (1970), *Atmospheric Tides*, D. Reidel, Hingham, Mass.

Cho, Y.-M., and G. G. Shepherd (2006), Correlation of airglow temperature and emission rate at Resolute Bay (74.68°N), over four winters (2001–2005), *Geophys. Res. Lett.*, *33*, L06815, doi:10.1029/2005GL025298.

Cogger, L. L., R. D. Elphinstone, and J. S. Murphree (1981), Temporal and latitudinal 5577 Å airglow observations, *Can. J. Phys.*, *59*, 1296–1307, doi:10.1139/p81-170.

Connes, P. (1956), Augmentation du produit luminosité x resolution des interfèromètres par l'emploi d'une différence de marche indépendante de l'incidence, *Rev. Opt.*, *35*, 37–43.

Culot, F., C. Lathuillère, J. Lilensten, and O. Witasse (2004), The OI 630.0 and 557.7nm dayglow measured by WINDII and modeled by TRANSCAR, *Ann. Geophys.*, *22*, 1947–1960, doi:10.5194/angeo-22-1947-2004.

Culot, F., C. Lathuillère, and J. Lilensten (2005), Influence of geomagnetic activity on the OI 630.0 and 557.7 nm dayglow, *J. Geophys. Res.*, *110*, A01304, doi:10.1029/2004JA010667.

Dewan, E. M. (1991), Similitude modeling of internal gravity wave spectra, *Geophys. Res. Lett.*, *18*, 1473–1476, doi:10.1029/91GL01522.

Dewan, E. M. (1994), The saturated-cascade model for atmospheric gravity wave spectra, and the wavelength-period (W-P) relations, *Geophys. Res. Lett.*, *21*, 817–820, doi:10.1029/94GL00702.

Drob, D. P., et al. (2008), An empirical model of the Earth's horizontal wind fields: HWM07, *J. Geophys. Res.*, *113*, A12304, doi:10.1029/2008JA013668.

Duboin, M.-L. (1974), La raie interdite λ 6300 Å de l'oxygène atomique au cours du renforcement précrépusculaire, PhD thesis, Univ. Paris VI, Paris.

Duboin, M.-L. (1997), Dynamics of the thermosphere: Diurnal variations observed by WINDII on board UARS, *J. Atmos. Sol. Terr. Phys.*, *59*, 669–673, doi:10.1016/S1364-6826(96)00102-2.

Ehhalt, D. H., E. P. Röth, and U. Schmidt (1983), On the temporal variance of stratospheric trace gas concentrations, *J. Atmos. Chem.*, *1*, 27–51, doi:10.1007/BF00113978.

Emmert, J. T., B. G. Fejer, C. G. Fesen, G. G. Shepherd, and B. H. Solheim (2001), Climatology of middle- and low-latitude daytime F region disturbance neutral winds measured by Wind Imaging Interferometer (WINDII), *J. Geophys. Res.*, *106*, 24,701–24,712, doi:10.1029/2000JA000372.

Emmert, J. T., B. G. Fejer, G. G. Shepherd, and B. H. Solheim (2002), Altitude dependence of middle and low-latitude daytime thermospheric disturbance winds measured by WINDII, *J. Geophys. Res.*, *107*(A12), 1483, doi:10.1029/2002JA009646.

Emmert, J. T., B. G. Fejer, G. G. Shepherd, and B. H. Solheim (2004), Average nighttime F region disturbance neutral winds measured by UARS WINDII: Initial results, *Geophys. Res. Lett.*, *31*, L22807, doi:10.1029/2004GL021611.

Emmert, J. T., D. P. Drob, G. G. Shepherd, G. Hernandez, M. J. Jarvis, J. W. Meriwether, R. J. Niciejewski, D. P. Sipler, and C. A. Tepley (2008), DWM07 global empirical model of upper thermospheric storm-induced disturbance winds, *J. Geophys. Res.*, *113*, A11319, doi:10.1029/2008JA013541.

Englert, C. R., D. D. Babcock, and J. M. Harlander (2007), Doppler asymmetric spatial heterodyne spectroscopy (DASH): Concept and experimental demonstration, *Appl. Opt.*, *46*, 7297–7307, doi:10.1364/AO.46.007297.

Evans, W. F., and L. Chardon (2000), The diurnal variations of polar mesospheric clouds in the Southern Hemisphere observed from WINDII, *Eos Trans. AGU*, *81*(48), Fall Meet. Suppl, Abstract SA11A-02.

Evans, W. F. J., and G. G. Shepherd (1996), A new airglow layer in the stratosphere, *Geophys. Res. Lett.*, *23*, 3623–3626, doi:10.1029/96GL03333.

Evans, W. F. J., L. LaFramboise, and G. Shepherd (1994a), Mesospheric temperatures from Rayleigh scattering measurements by the WINDII instrument on UARS, *Adv. Space Res.*, *14*, 285–288, doi:10.1016/0273-1177(94)90150-3.

Evans, W. F. J., L. LaFramboise, and G. Shepherd (1994b), Mesospheric temperatures from Rayleigh scattering measurements by the WINDII instrument on UARS, *Adv. Space Res.*, *14*, 285–288, doi:10.1016/0273-1177(94)90150-3.

Evans, W. F. J., L. R. Laframboise, K. R. Sine, R. H. Wiens, and G. G. Shepherd (1995), Observation of polar mesospheric clouds in summer, 1993 by the WINDII instrument on UARS, *Geophys. Res. Lett.*, *22*, 2793–2796, doi:10.1029/95GL03018.

Fauliot, V., G. Thuillier, and F. Vial (1997), Mean vertical wind in the mesosphere-lower thermosphere region (80–120 km) deduced from the WINDII observations on board UARS, *Ann. Geophys.*, *15*, 1221–1231.

Fejer, B. G., J. T. Emmert, G. G. Shepherd, and B. H. Solheim (2000), Average daytime F region disturbance neutral winds measured by UARS: Initial results, *Geophys. Res. Lett.*, *27*, 1859–1862, doi:10.1029/2000GL003787.

Fisher, G. M., T. L. Killeen, Q. Wu, J. M. Reeves, P. B. Hays, W. A. Gault, S. Brown, and G. G. Shepherd (2000), Polar cap mesosphere wind observations: Comparisons of simultaneous measurements with a Fabry-Perot interferometer and a field-widened Michelson interferometer, *Appl. Opt.*, *39*, 4284–4291, doi:10.1364/AO.39.004284.

Forbes, J. M., X. Zhang, W. Ward, and E. R. Talaat (2002), Climatological features of mesosphere and lower thermosphere stationary planetary waves within ±40° latitude, *J. Geophys. Res.*, *107*(D17), 4322, doi:10.1029/2001JD001232.

Forbes, J. M., X. L. Zhang, E. R. Talaat, and W. Ward (2003), Nonmigrating diurnal tides in the thermosphere, *J. Geophys. Res.*, *108*(A1), 1033, doi:10.1029/2002JA009262.

Garcia, R., and S. Solomon (1985), The effect of breaking gravity waves on the dynamics and chemical composition of the mesosphere and lower thermosphere, *J. Geophys. Res.*, *90*, 3850–3868, doi:10.1029/JD090iD02p03850.

Gardner, C. S. (1994), Diffusive filtering theory of gravity wave spectra in the atmosphere, *J. Geophys. Res.*, *99*, 20,601–20,622, doi:10.1029/94JD00819.

Gardner, C. S., C. A. Hostetler, and S. J. Franke (1993), Gravity wave models for the horizontal wave number spectra of atmospheric velocity and density fluctuations, *J. Geophys. Res.*, *98*, 1035–1049, doi:10.1029/92JD02051.

Gault, W. A., J.-F. Brun, D.-L. Desaulniers, D. W. Miller, F. Pasternak, Y. Rochon, J. M. Rupil, and G. G. Shepherd (1992), Design and on-orbit performance of the WINDII baffle system, in *Stray Radiation in Optical Systems II*, *Proc. SPIE*, *1753*, 189–195.

Gault, W. A., et al. (1996a), Validation of O(^{1}S) Wind Measurements by WINDII the Wind Imaging Interferometer on UARS, *J. Geophys. Res.*, *101*, 10,405–10,430, doi:10.1029/95JD03352.

Gault, W. A., S. Brown, A. Moise, D. Liang, G. Sellar, G. G. Shepherd, and J. Wimperis (1996b), Erwin: An E-region wind interferometer, *Appl. Opt.*, *35*, 2913–2922, doi:10.1364/AO.35.002913.

Gault, W. A., S. Sargoytchev, and G. G. Shepherd (1996c), Divided-mirror scanning technique for a small Michelson interferometer, in *Optical Spectroscopic Techniques and Instrumentation for Atmospheric and Space Research II*, edited by P. B. Hays and J. Wang, *Proc SPIE*, *2830*, 15–18.

Greer, R. G. H., et al. (1986), Eton 1: A data base pertinent to the study of energy transfer in the oxygen nightglow, *Planet. Space Sci.*, *34*, 771–788, doi:10.1016/0032-0633(86)90074-7.

Groves, G. V. (1980), Seasonal and diurnal variations of middle atmosphere winds, *Philos. Trans. R. Soc. London, Ser. A*, *296*, 19–40, doi:10.1098/rsta.1980.0153.

Harlander, J. M., C. R. Englert, D. D. Babcock, and F. L. Roesler (2010), Design and laboratory tests of a Doppler Asymmetric Spatial Heterodyne (DASH) interferometer for upper atmospheric wind and temperature observations, *Opt. Express*, *18*(25), 26,430–26,440, doi:10.1364/OE.18.026430.

Hays, P. B. (1990), Circle to line interferometer optical system, *Appl. Opt.*, *29*, 1482–1489, doi:10.1364/AO.29.001482.

Hays, P. B., V. J. Abreu, M. E. Dobbs, D. A. Gell, H. J. Grassl, and W. R. Skinner (1993), The high-resolution Doppler imager on the Upper Atmosphere Research Satellite, *J. Geophys. Res.*, *98*, 10,713–10,723, doi:10.1029/93JD00409.

Hays, P. B., J. F. Kafkalidis, W. R. Skinner, and R. G. Roble (2003), A global view of the molecular oxygen night airglow, *J. Geophys. Res.*, *108*(D20), 4646, doi:10.1029/2003JD003400.

Hedin, A. E. (1991), Extension of the MSIS thermosphere model into the middle and lower thermosphere, *J. Geophys. Res.*, *96*, 1159–1172, doi:10.1029/90JA02125.

Hedin, A. E., et al. (1996), Empirical wind model for the middle and lower atmosphere, *J. Atmos. Terr. Phys.*, *58*, 1421–1447, doi:10.1016/0021-9169(95)00122-0.

Hersom, C. H., and G. G. Shepherd (1995), Characterization of the WIND Imaging Interferometer, *Appl. Opt.*, *34*, 2871–2879, doi:10.1364/AO.34.002871.

Hilliard, R. L., and G. G. Shepherd (1966a), Wide-angle Michelson interferometer for measuring Doppler line widths, *J. Opt. Soc. Am.*, *56*, 362–369, doi:10.1364/JOSA.56.000362.

Hilliard, R. L., and G. G. Shepherd (1966b), Upper atmospheric temperatures from Doppler line widths - IV. A detailed study using the 0I 5577 Å auroral and night glow emissions, *Planet. Space Sci.*, *14*, 383–406, doi:10.1016/0032-0633(66)90011-0.

Hines, C. O. (1991a), The saturation of gravity waves in the middle atmosphere, Part I: Critique of linear instability theory, *J. Atmos. Sci.*, *48*, 1348–1360, doi:10.1175/1520-0469(1991)048<1348:TSOGWI>2.0.CO;2.

Hines, C. O. (1991b), The saturation of gravity waves in the middle atmosphere, Part II: Development of Doppler spread theory, *J. Atmos. Sci.*, *48*, 1361–1379, doi:10.1175/1520-0469(1991)048<1361:TSOGWI>2.0.CO;2.

Hines, C. O. (1997), A fundamental theorem of airglow fluctuations induced by gravity waves, *J. Atmos. Sol. Terr. Phys.*, *59*, 319–326, doi:10.1016/S1364-6826(96)00017-X.

Hines, C. O., and D. W. Tarasick (1987), On the detection and utilization of gravity waves in airglow studies, *Planet. Space Sci.*, *35*, 851–866, doi:10.1016/0032-0633(87)90063-8.

Hines, C. O., and D. W. Tarasick (1993), On the nonlinear response of airglow to atmospheric gravity waves, *J. Geophys. Res.*, *98*, 19,127–19,131, doi:10.1029/93JA00219.

Hoffmann, P., E. Becker, W. Singer, and M. Placke (2010), Seasonal variation of mesospheric waves at northern middle and high latitudes, *J. Atmos. Sol. Terr. Phys.*, *72*, 1068–1079, doi:10.1016/j.jastp.2010.07.002.

Hubert, B., J.-C. Gérard, T. L. Killeen, Q. Wu, D. V. Bisikalo, and V. I. Shematovich (2001), Observation of anomalous temperatures in the daytime O(^{1}D) 6300 Å thermospheric emission: A possible signature of non-thermal atoms, *J. Geophys. Res.*, *106*, 12,753–12,764, doi:10.1029/2000JA900122.

Hunten, D. M., F. E. Roach, and J. W. Chamberlain (1956), A photometric unit for the airglow and aurora, *J. Atmos. Terr. Phys.*, *8*, 345–346, doi:10.1016/0021-9169(56)90111-8.

Iwagami, N., et al. (2002), The wave 2000 campaign: Overview and preliminary results, *J. Atmos. Sol. Terr. Phys.*, *64*, 1095–1104, doi:10.1016/S1364-6826(02)00060-3.

Jacobi, C., C. Arras, D. Kürschner, W. Singer, P. Hoffmann, and D. Keuer (2009), Comparison of mesopause region meteor radar winds, medium frequency radar winds and low frequency drifts over Germany, *Adv. Space Res.*, *43*, 247–252, doi:10.1016/j.asr.2008.05.009.

Killeen, T. L., P. B. Hays, B. C. Kennedy, and D. Rees (1982), Stable and rugged etalon for the Dynamics Explorer Fabry-Perot interferometer. 2: Performance, *Appl. Opt.*, *21*, 3903–3912, doi:10.1364/AO.21.003903.

Killeen, T. L., Q. Wu, S. C. Solomon, D. A. Ortland, W. R. Skinner, R. J. Niciejewski, and D. A. Gell (2006), TIMED Doppler Interferometer: Overview and recent results, *J. Geophys. Res.*, *111*, A10S01, doi:10.1029/2005JA011484.

Kirkwood, S., and K. Stebel (2003), Influence of planetary waves on noctilucent cloud occurrence over NW Europe, *J. Geophys. Res.*, *108*(D8), 8440, doi:10.1029/2002JD002356.

Lathuillère, C., and M. Menvielle (2004), WINDII thermosphere temperature perturbations for magnetically active situations, *J. Geophys. Res.*, *109*, A11304, doi:10.1029/2004JA010526.

Lathuillère, C., W. A. Gault, B. Lamballais, Y. J. Rochon, and B. H. Solheim (2002), Doppler temperatures from O(^{1}D) airglow in the daytime thermosphere as observed by the WIND Imaging Interferometer (WINDII) on the UARS satellite, *Ann. Geophys.*, *20*, 203–212, doi:10.5194/angeo-20-203-2002.

Lee, Y.-S., and G. G. Shepherd (2007), The statistical comparison of WINDII auroral green line emission rate with DMSP/SSJ4 electron energy input for high and low solar flux years, *J. Geophys. Res.*, *112*, A12301, doi:10.1029/2007JA012323.

Lee, Y.-S., and G. G. Shepherd (2010), Summer high-latitude mesospheric observations of supersonic bursts and O(^{1}S) emission rate with the UARS WINDII instrument and the association with sprites, meteors, and lightning, *J. Geophys. Res.*, *115*, A00E26, doi:10.1029/2009JA014731.

Liu, G., and G. G. Shepherd (2006a), An empirical model for the altitude of the OH nightglow emission, *Geophys. Res. Lett.*, *33*, L09805, doi:10.1029/2005GL025297.

Liu, G., and G. G. Shepherd (2006b), Perturbed profiles of oxygen nightglow emissions as observed by WINDII on UARS, *J. Atmos. Sol. Terr. Phys.*, *68*, 1018–1028, doi:10.1016/j.jastp.2005.12.004.

Liu, G., and G. G. Shepherd (2008), An investigation of the solar cycle impact on the lower thermosphere O(^{1}S) nightglow emission as observed by WINDII/UARS, *Adv. Space Res.*, *42*, 933–938, doi:10.1016/j.asr.2007.10.008.

Liu, G., G. G. Shepherd, and R. G. Roble (2008), Seasonal variations of the nighttime O(^{1}S) and OH airglow emission rates at mid-to-high latitudes in the context of the large-scale circulation, *J. Geophys. Res.*, *113*, A06302, doi:10.1029/2007JA012854.

Llewellyn, E. J. (1988), The concentration of atomic oxygen in the mesosphere and thermosphere, *Planet. Space Sci.*, *36*, 892, doi:10.1016/0032-0633(88)90095-5.

López-González, M. J., et al. (2007), Ground-based mesospheric temperatures at mid-latitude derived from O_2 and OH airglow SATI data: Comparison with SABER measurements, *J. Atmos. Sol. Terr. Phys.*, *69*, 2379–2390, doi:10.1016/j.jastp.2007.07.004.

Lowe, R. P., L. M. LeBlanc, and K. L. Gilbert (1996), WINDII/UARS observation of twilight behaviour of the hydroxyl airglow at mid-latitude equinox, *J. Atmos. Terr. Phys.*, *58*, 1863–1869, doi:10.1016/0021-9169(95)00178-6.

Maharaj-Sharma, R. (2002), Solar variability of the atomic oxygen greenline emissions in the middle and lower thermosphere, PhD thesis, York Univ., Toronto, Ont., Canada.

Maharaj-Sharma, R., and G. G. Shepherd (2004), Solar variability of the daytime atomic oxygen O(^{1}S) emission in the middle and lower thermosphere, *J. Geophys. Res.*, *109*, A03303, doi:10.1029/2003JA010183.

Makhlouf, U. B., R. H. Picard, M. J. Taylor, and J. R. Winick (1997), Gravity waves and vertical diffusion in the lower thermosphere from 557.7nm airglow, *Adv. Space Res.*, *19*, 583–586, doi:10.1016/S0273-1177(97)00177-4.

McDade, I. C. (1997), Laboratory measurements required for upper atmospheric remote sensing of atomic oxygen, *Adv. Space Res.*, *19*(4), 653–661, doi:10.1016/S0273-1177(97)00159-2.

McDade, I. C. (1998), The photochemistry of the MLT oxygen airglow emissions and the expected influences of tidal perturbations, *Adv. Space Res.*, *21*, 787–794, doi:10.1016/S0273-1177(97)00674-1.

McDade, I. C., and E. J. Llewellyn (1986), The excitation of O(^{1}S) and O_2 bands in the nightglow: A brief review and preview, *Can. J. Phys.*, *64*, 1626–1630, doi:10.1139/p86-287.

McDade, I. C., D. P. Murtagh, R. G. H. Greer, P. H. G. Dickinson, G. Witt, J. Stegman, E. J. Llewellyn, L. Thomas, and D. B. Jenkins (1986a), ETON 2: Quenching parameters for proposed precursors of $O_2(b^1\Sigma_g^+)$ and O(^{1}S) in the terrestrial nightglow, *Planet. Space Sci.*, *34*, 789–800, doi:10.1016/0032-0633(86)90075-9.

McDade, I. C., E. J. Llewellyn, R. G. H. Greer, and D. P. Murtagh (1986b), ETON 3: Altitude profiles of the nightglow continuum at green and near-infrared wavelengths, *Planet. Space Sci.*, *34*, 801–810, doi:10.1016/0032-0633(86)90076-0.

McDade, I. C., E. J. Llewellyn, D. P. Murtagh, and R. G. H. Greer (1987), ETON 5: Simultaneous rocket measurements of the OH Meinel $\Delta\nu = 2$ sequence and (8,3) band emission profiles in the nightglow, *Planet. Space Sci.*, *35*, 1137–1147, doi:10.1016/0032-0633(87)90020-1.

McDade, I. C., W. E. Sharp, P. G. Richards, and D. G. Torr (1991), On the inversion of $O^+(^2D\text{-}^2P)$ twilight airglow observations: A method for recovering both the ionization frequency and the thermospheric oxygen atom densities, *J. Geophys. Res.*, *96*, 259–266, doi:10.1029/90JA01995.

McLandress, C. (2002), The seasonal variation of the propagating diurnal tide in the mesosphere and lower thermosphere. Part II: The role of tidal heating and zonal mean winds, *J. Atmos. Sci.*, *59*, 907–922, doi:10.1175/1520-0469(2002)059<0907:TSVOTP>2.0.CO;2.

McLandress, C., and S. P. Zhang (2007), Satellite observations of mean winds and tides in the lower thermosphere: Part 1. Aliasing and sampling issues, *J. Geophys. Res.*, *112*, D21104, doi:10.1029/2007JD008456.

McLandress, C., Y. Rochon, G. G. Shepherd, B. H. Solheim, G. Thuillier, and F. Vial (1994), Meridional wind component of the thermospheric tide observed by WINDII on UARS, *Geophys. Res. Lett.*, *21*, 2417–2420, doi:10.1029/94GL02367.

McLandress, C., G. G. Shepherd, and B. H. Solheim (1996a), Satellite observations of thermospheric tides: Results from WINDII on UARS, *J. Geophys. Res.*, *101*, 4093–4114, doi:10.1029/95JD03359.

McLandress, C., G. G. Shepherd, B. H. Solheim, M. D. Burrage, P. B. Hays, and W. R. Skinner (1996b), Combined mesosphere/thermosphere winds using WINDII and HRDI data from the Upper Atmosphere Research Satellite, *J. Geophys. Res.*, *101*, 10,441–10,453, doi:10.1029/95JD01706.

Meier, R., G. Crowley, D. J. Strickland, A. B. Christensen, L. J. Paxton, D. Morrison, and C. L. Hackert (2005), First look at the 20 November 2003 superstorm with TIMED/GUVI: Comparisons with a thermospheric global circulation model, *J. Geophys. Res.*, *110*, A09S41, doi:10.1029/2004JA010990.

Melo, S. M. L., R. P. Lowe, and J. P. Russell (2000), Double-peaked hydroxyl airglow profiles observed from WINDII/UARS, *J. Geophys. Res.*, *105*, 12,397–12,403, doi:10.1029/1999JD901169.

Meriwether, J. W. (1989), A review of the photochemistry of selected nightglow emissions from the mesopause, *J. Geophys. Res.*, *94*, 14,629–14,646, doi:10.1029/JD094iD12p14629.

Nicolls, M. J., M. N. Vlasov, M. C. Kelley, and G. G. Shepherd (2006), Discrepancy between the nighttime molecular ion composition given by the International Reference Atmosphere model and airglow measurements at low latitudes, *J. Geophys. Res.*, *111*, A03304, doi:10.1029/2005JA011216.

Oberheide, J., Q. Wu, T. L. Killeen, M. E. Hagan, and R. G. Roble (2006), Diurnal nonmigrating tides from TIMED Doppler Interferometer wind data: Monthly climatologies and seasonal variations, *J. Geophys. Res.*, *111*, A10S03, doi:10.1029/2005JA011491.

Oberheide, J., Q. Wu, T. L. Killeen, M. E. Hagan, and R. G. Roble (2007), A climatology of nonmigrating semidiurnal tides from TIMED Doppler Interferometer (TIDI) wind data, *J. Atmos. Sol. Terr. Phys.*, *69*, 2203–2218, doi:10.1016/j.jastp.2007.05.010.

Osprey, S. M., and B. N. Lawrence (2001), A possible mechanism for in situ forcing of planetary waves in the summer extratropical mesosphere, *Geophys. Res. Lett.*, *28*, 1183–1186, doi:10.1029/2000GL011984.

Pancheva, D., et al. (2008), Planetary waves in coupling the stratosphere and mesosphere during the major stratospheric warming in 2003/2004, *J. Geophys. Res.*, *113*, D12105, doi:10.1029/2007JD009011.

Phillips, D. L. (1962), A technique for the numerical solution of certain integral equations of the first kind, *J. ACM*, *9*, 84–97, doi:10.1145/321105.321114.

Portnyagin, Y. (2006), A review of mesospheric and lower thermosphere models, *Adv. Space Res.*, *38*, 2452–2460, doi:10.1016/j.asr.2006.04.030.

Richmond, A. D., C. Lathuillère, and S. Vennerstroem (2003), Winds in the high-latitude lower thermosphere: Dependence on the interplanetary magnetic field, *J. Geophys. Res.*, *108*(A2), 1066, doi:10.1029/2002JA009493.

Ridley, B. A., F. E. Grahek, and J. G. Walega (1992), A small high sensitivity, medium-response ozone detector suitable for measurements from light aircraft, *J. Atmos. Oceanic Technol.*, *9*, 142–148, doi:10.1175/1520-0426(1992)009<0142:ASHSMR>2.0.CO;2.

Roble, R. G., and G. G. Shepherd (1997), An analysis of Wind Imaging Interferometer observations of O(^{1}S) equatorial emission rates using the thermosphere-ionosphere mesosphere-electrodynamics general circulation model, *J. Geophys. Res.*, *102*, 2467–2474, doi:10.1029/96JA02930.

Rochon, Y. J. (1999), The retrieval of winds, Doppler temperatures, and emission rates for the WINDII experiment, PhD thesis, York Univ., Toronto, Ont., Canada.

Russell, J. P., and R. P. Lowe (2003), Atomic oxygen profiles (80–4 km) derived from Wind Imaging Interferometer/Upper Atmospheric Research Satellite measurements of the hydroxyl airglow: 1. Validation of technique, *J. Geophys. Res.*, *108*(D21), 4662, doi:10.1029/2003JD003454.

Russell, J. P., R. P. Lowe, and W. E. Ward (2004), Atomic oxygen annual and semi-annual oscillations in the mesopause region for mid and equatorial latitudes, *J. Atmos. Sol. Terr. Phys.*, *66*, 451–461, doi:10.1016/j.jastp.2004.01.004.

Russell, J. P., W. E. Ward, R. P. Lowe, R. G. Roble, G. G. Shepherd, and B. H. Solheim (2005), Atomic oxygen profiles (80 to 115 km) derived from WINDII/UARS measurements of the hydroxyl and greenline airglow: Local time–latitude dependence, *J. Geophys. Res.*, *110*, D15305, doi:10.1029/2004JD005570.

Schoeberl, M. R., and M. A. Geller (1977), A calculation of the structure of stationary planetary waves in winter, *J. Atmos. Sci.*, *34*, 1235–1255, doi:10.1175/1520-0469(1977)034<1235:ACOTSO>2.0.CO;2.

She, C.-Y., and R. P. Lowe (1998), Seasonal temperature variations in the mesopause region at mid-latitude: Comparison of lidar and hydroxyl rotational temperatures using WINDII/UARS height profiles, *J. Atmos. Sol. Terr. Phys.*, *60*, 1573–1583, doi:10.1016/S1364-6826(98)00082-0.

Shepherd, G. G. (2002), *Spectral Imaging of the Atmosphere*, *Int. Geophys. Ser.*, vol. 82, Academic, San Diego, Calif..

Shepherd, G. G. (2011), Thermospheric observations of equatorial wavenumber 4 density perturbations from WINDII data, *Geophys. Res. Lett.*, *38*, L08801, doi:10.1029/2011GL046986.

Shepherd, G. G., and Y.-M. Cho (2011), Global thermospheric atomic oxygen variations observed with the WIND Imaging Interferometer (WINDII): Wave 4 at low and high latitudes, *J. Geophys. Res.*, *116*, A10314, doi:10.1029/2011JA016880.

Shepherd, G. G., W. A. Gault, D. W. Miller, Z. Pasturczyk, S. F. Johnston, P. R. Kosteniuk, J. W. Haslett, D. J. Kendall, and J. R. Wimperis (1985), WAMDII: Wide-angle Michelson Doppler imaging interferometer for Spacelab, *Appl. Opt.*, *24*, 1571–1584, doi:10.1364/AO.24.001571.

Shepherd, G. G., et al. (1993a), WINDII, the Wind Imaging Interferometer on the Upper Atmosphere Research Satellite, *J. Geophys. Res.*, *98*, 10,725–10,750, doi:10.1029/93JD00227.

Shepherd, G. G., et al. (1993b), Longitudinal structure in atomic oxygen concentrations observed with WINDII on UARS, *Geophys. Res. Lett.*, *20*, 1303–1306, doi:10.1029/93GL01105.

Shepherd, G. G., C. McLandress, and B. H. Solheim (1995), Tidal influence on O(^{1}S) airglow emission rate distributions at the geographic equator as observed by WINDII, *Geophys. Res. Lett.*, *22*, 275–278, doi:10.1029/94GL03052.

Shepherd, G. G., R. G. Roble, S.-P. Zhang, C. McLandress, and R. H. Wiens (1998), Tidal influence on midlatitude airglow: Comparison of satellite and ground-based observations with TIME-GCM predictions, *J. Geophys. Res.*, *103*, 14,741–14,751, doi:10.1029/98JA00884.

Shepherd, G. G., J. Stegman, P. Espy, C. McLandress, G. Thuillier, and R. H. Wiens (1999), Springtime transition in lower thermospheric atomic oxygen, *J. Geophys. Res.*, *104*, 213–223, doi:10.1029/98JA02831.

Shepherd, G. G., I. C. McDade, W. A. Gault, Y. J. Rochon, A. Scott, N. Rowlands, and G. Buttner (2001), The Stratospheric Wind Interferometer For Transport Studies (SWIFT), *Adv. Space Res.*, *27*, 1071–1079, doi:10.1016/S0273-1177(01)00140-5.

Shepherd, G. G., J. Stegman, W. Singer, and R. G. Roble (2004a), Equinox transition in wind and airglow observations, *J. Atmos. Sol. Terr. Phys.*, *66*(6–9), 481–491, doi:10.1016/j.jastp.2004.01.005.

Shepherd, G. G., G. Liu, and R. G. Roble (2004b), Remote sensing of the large-scale circulation of atomic oxygen, in *Remote Sensing of Clouds and the Atmosphere IX*, edited by K. Schafer et al., *Proc. SPIE*, *5571*, 173–181.

Shepherd, M. G., and C. Fricke-Begemann (2004), Study of the tidal variations in mesospheric temperature at low and mid latitudes from WINDII and potassium lidar observations, *Ann. Geophys.*, *22*, 1513–1528, doi:10.5194/angeo-22-1513-2004.

Shepherd, M. G., and G. G. Shepherd (2011), Stratospheric warming effects on thermospheric O(^{1}S) dayglow dynamics, *J. Geophys. Res.*, *116*, A11327, doi:10.1029/2011JA016762.

Shepherd, M. G., R. L. Gattinger, Y. Rochon, G. G. Shepherd, B. H. Solheim, and D. J. W. Kendall (1996), Auroral observations with the WIND Imaging Interferometer (WINDII) on UARS, *Adv. Space Res.*, *17*, 5–10, doi:10.1016/0273-1177(95)00724-S.

Shepherd, M. G., A. Dudhia, M. Lopez-Puertas, and W. F. J. Evans (1997), Upper mesosphere temperatures in summer; WINDII observations and comparisons, *Geophys. Res. Lett.*, *24*, 357–360, doi:10.1029/97GL00187.

Shepherd, M. G., B. Reid, S. Zhang, B. H. Solheim, G. G. Shepherd, V. B. Wickwar, and J. P. Herron (2001), Retrieval and validation of mesospheric temperatures from Wind Imaging Interferometer observations, *J. Geophys. Res.*, *106*, 24,813–24,829, doi:10.1029/2000JA000323.

Shepherd, M. G., P. J. Espy, C. Y. She, W. Hocking, P. Keckhut, G. Gavrilieva, G. G. Shepherd, and B. Naujokat (2002), Springtime transition in upper mesospheric temperature in the northern hemisphere, *J. Atmos. Sol. Terr. Phys.*, *64*, 1183–1199, doi:10.1016/S1364-6826(02)00068-8.

Shepherd, M. G., W. F. J. Evans, G. Hernandez, D. Offermann, and H. Takahashi (2004a), Global variability of mesospheric temperature: 1. Mean temperature field, *J. Geophys. Res.*, *109*, D24117, doi:10.1029/2004JD005054.

Shepherd, M. G., Y. J. Rochon, D. Offermann, M. Donner, and P. J. Espy (2004b), Longitudinal variability of mesospheric temperatures during equinox at middle and high latitudes, *J. Atmos. Sol. Terr. Phys.*, *66*, 463–479, doi:10.1016/j.jastp.2004.01.036.

Shepherd, M. G., G. G. Shepherd, W. F. J. Evans, and S. Sridharan (2005), Global variability of mesospheric temperature: Planetary scale perturbation at equatorial and tropical latitudes, *J. Geophys. Res.*, *110*, D24103, doi:10.1029/2005JD006128.

Shepherd, M. G., G. Liu, and G. G. Shepherd (2006), Mesospheric semiannual oscillation in temperature and nightglow emission, *J. Atmos. Sol. Terr. Phys.*, *68*, 379–389, doi:10.1016/j.jastp.2005.02.029.

Shepherd, M. G., G. L. Wu, I. N. Fedulina, S. Gurubaran, J. M. Russell, M. G. Mlynczak, and G. G. Shepherd (2007), Stratospheric warming effects on the tropical mesospheric temperature field, *J. Atmos. Sol. Terr. Phys.*, *69*, 2309–2337, doi:10.1016/j.jastp.2007.04.009.

Shepherd, M. G., D. L. Wu, I. N. Fedulina, and S. Gurubaran (2008), Temperature variability in the tropical mesosphere during the northern hemisphere winter, *Adv. Space Res.*, *41*, 1435–1446, doi:10.1016/j.asr.2007.04.035.

Shettle, E. P., G. E. Thomas, J. J. Olivero, W. F. J. Evans, D. J. Debrestian, and L. Chardon (2002), A three satellite comparison

of polar mesospheric clouds: Evidence for long-term change, *J. Geophys. Res.*, *107*(D12), 4134, doi:10.1029/2001JD000668.

Singh, V., I. C. McDade, G. G. Shepherd, B. H. Solheim, and W. E. Ward (1996a), The O(^{1}S) dayglow emission as observed by the WIND imaging interferometer on the UARS, *Ann. Geophys.*, *14*, 637–646, doi:10.1007/s00585-996-0637-y.

Singh, V., I. C. McDade, G. G. Shepherd, B. H. Solheim, and W. E. Ward (1996b), The (O^{1}D) dayglow emission as observed by the Wind Imaging Interferometer on UARS, *Adv. Space Res.*, *17*(11), 11–14, doi:10.1016/0273-1177(95)00725-T.

Slanger, T. G., and D. E. Osterbrock (2000), Investigation of potassium, lithium and sodium emissions in the nightglow, and OH cross-calibration, *J. Geophys. Res.*, *105*, 1425–1429, doi:10.1029/1999JD901027.

Smith, A. K., D. R. Marsh, M. G. Mlynczak, and J. C. Mast (2010), Temporal variations of atomic oxygen in the upper mesosphere from SABER, *J. Geophys. Res.*, *115*, D18309, doi:10.1029/2009JD013434.

Sopoco, T. H. (2001), A Neural Network Technique for Atmospheric Inversion of WINDII and Osiris Data, MS thesis, Trent Univ., Petersborough, Ont., Canada.

Talaat, E. R., and R. S. Lieberman (2010), Direct observations of nonmigrating diurnal tides in the equatorial thermosphere, *Geophys. Res. Lett.*, *37*, L04803, doi:10.1029/2009GL041845.

Taylor, M. J., D. C. Fritts, and J. R. Isler (1995), Determination of horizontal and vertical structure of an unusual pattern of short period gravity waves imaged during ALOHA-93, *Geophys. Res. Lett.*, *22*, 2837–2840, doi:10.1029/95GL02945.

Thuillier, G., and M. Hersé (1988), Measurements of wind in the upper atmosphere: First results of the MICADO instrument, in *Progress in Atmospheric Physics*, edited by R. Rodrigo et al., pp. 61–73, Kluwer Acad., Dordrecht, Netherlands.

Thuillier, G., and M. Hersé (1991), Thermally stable field compensated Michelson interferometer for measurements of temperature and wind of the planetary atmosphere, *Appl. Opt.*, *30*, 1210–1220, doi:10.1364/AO.30.001210.

Thuillier, G., and G. G. Shepherd (1985), Fully compensated Michelson interferometer of fixed path difference, *Appl. Opt.*, *24*, 1599–1603, doi:10.1364/AO.24.001599.

Thuillier, G., C. Lathuillère, M. Hersé, C. Senior, W. Kofman, M.-L. Duboin, D. Alcayde, F. Barlier, and J. Fontanari (1990), Coordinated EISCAT-MICADO interferometer measurements of neutral winds and temperatures in *E*- and *F*-regions, *J. Atmos. Terr. Phys.*, *52*, 625–636, doi:10.1016/0021-9169(90)90057-T.

Thuillier, G., V. Fauliot, M. Herse, L. Bourg, and G. G. Shepherd (1996), The MICADO wind measurements from Observatoire de Haute-Provence for the validation of the WINDII green line data, *J. Geophys. Res.*, *101*, 10,431–10,440, doi:10.1029/95JD03522.

Thuillier, G., W. A. Gault, J.-F. Brun, M. Hersé, W. Ward, and C. Hersom (1998), In-flight calibration of the Wind Imaging Interferometer (WINDII) on board the Upper Atmosphere Research Satellite, *Appl. Opt.*, *37*, 1356–1369, doi:10.1364/AO.37.001356.

Thuillier, G., R. H. Wiens, G. G. Shepherd, and R. G. Roble (2002), Photochemistry and dynamics in thermospheric intertropical arcs measured by the WIND Imaging Interferometer on board UARS: A comparison with TIE-GCM simulations, *J. Atmos. Sol. Terr. Phys.*, *64*, 405–415, doi:10.1016/S1364-6826(01)00109-2.

Tikhonov, A. N. (1962), Solution of incorrectly formulated problems and the regularization method, *Sov. Math. Dokl., Engl. Transl.*, *4*, 1035–1038.

Title, A. M., and H. E. Ramsey (1980), Improvements in birefringent filters. 6: Analog birefringent elements, *Appl. Opt.*, *19*, 2046–2058, doi:10.1364/AO.19.002046.

Twomey, S. (1963), On the numerical solution of Fredholm integral equations of the first kind by the inversion of the linear systems produced by quadrature, *J. ACM*, *10*, 97–101, doi:10.1145/321150.321157.

Vergados, P., and M. G. Shepherd (2009), Retrieving mesospheric water vapour from observations of volume scattering radiances, *Ann. Geophys.*, *27*, 487–501, doi:10.5194/angeo-27-487-2009.

von Savigny, C. H., I. C. McDade, G. G. Shepherd, and Y. Rochon (1999), Lower thermospheric nitric oxide concentrations derived from WINDII observations of the green nightglow continuum at 553 nm, *Ann. Geophys.*, *17*, 1439–1446.

Wang, D. Y., C. McLandress, E. L. Fleming, W. E. Ward, B. Solheim, and G. G. Shepherd (1997), Empirical model of 90–120 km horizontal winds from wind-imaging interferometer green line measurements in 1992–1993, *J. Geophys. Res.*, *102*, 6729–6745, doi:10.1029/96JD03492.

Wang, D. Y., W. E. Ward, G. G. Shepherd, and D. L. Wu (2000a), Stationary planetary waves inferred from WINDII wind data taken within 90–120 km altitudes 90–120 km during 1991–1996, *J. Atmos. Sci.*, *57*, 1906–1918, doi:10.1175/1520-0469(2000)057<1906:SPWIFW>2.0.CO;2.

Wang, D. Y., W. E. Ward, B. H. Solheim, and G. G. Shepherd (2000b), Wavenumber spectra of horizontal wind and temperature measured with WINDII, Part I: Observational results, *J. Atmos. Sol. Terr. Phys.*, *62*, 967–979, doi:10.1016/S1364-6826(00)00064-X.

Wang, D. Y., W. E. Ward, B. H. Solheim, and G. G. Shepherd (2000c), Wavenumber spectra of horizontal wind and temperature measured with WINDII, Part II: Diffusive effect on spectral formation, *J. Atmos. Sol. Terr. Phys.*, *62*, 981–991, doi:10.1016/S1364-6826(00)00065-1.

Wang, D. Y., W. E. Ward, Y. J. Rochon, and G. G. Shepherd (2001a), Airglow intensity variations induced by gravity waves, Part 1: Generalization of the Hines-Tarasick's theory, *J. Atmos. Sol. Terr. Phys.*, *63*, 35–46, doi:10.1016/S1364-6826(00)00157-7.

Wang, D. Y., Y. J. Rochon, S. P. Zhang, W. E. Ward, R. H. Wiens, D. Y. Liang, W. A. Gault, B. H. Solheim, and G. G. Shepherd (2001b), Airglow intensity variations induced by gravity waves, Part 2: Comparisons with observations, *J. Atmos. Sol. Terr. Phys.*, *63*, 47–60, doi:10.1016/S1364-6826(00)00158-9.

Wang, D. Y., W. E. Ward, B. H. Solheim, and G. G. Shepherd (2002), Longitudinal variations of green line emission rates observed by WINDII at altitudes 90–120 km during 1991–1996, *J. Atmos. Sol. Terr. Phys.*, *64*, 1273–1286, doi:10.1016/S1364-6826(02)00041-X.

Ward, W. E. (1998), Tidal mechanisms of dynamical influence on oxygen recombination airglow in the mesosphere and lower thermosphere, *Adv. Space Res.*, *21*, 795–805, doi:10.1016/S0273-1177(97)00676-5.

Ward, W. E. (1999), A simple model of diurnal variations in the mesospheric oxygen nightglow, *Geophys. Res. Lett.*, *26*, 3565–3568, doi:10.1029/1999GL003661.

Ward, W. E., Y. J. Rochon, C. McLandress, D. Y. Wang, J. R. Criswick, B. H. Solheim, and G. G. Shepherd (1994), Correlations between the mesospheric O(^{1}S) emission peak intensity and height and temperature at 98 km using WINDII data, *Adv. Space Res.*, *14*(9), 57–60, doi:10.1016/0273-1177(94)90115-5.

Ward, W. E., D. Y. Wang, B. H. Solheim, and G. G. Shepherd (1996), Observations of the two-day wave in WINDII data during January, 1993, *Geophys. Res. Lett.*, *23*, 2923–2926, doi:10.1029/96GL02897.

Ward, W. E., B. H. Solheim, and G. G. Shepherd (1997), Two day wave induced variations in the oxygen green line volume emission rate: WINDII observations, *Geophys. Res. Lett.*, *24*, 1127–1130, doi:10.1029/97GL01022.

Ward, W. E., W. A. Gault, G. G. Shepherd, and N. Rowlands (2001), The Waves Michelson Interferometer: A visible/near-IR interferometer for observing middle atmosphere dynamics and constituents, in *Sensors, Systems and Next-Generation Satellites V*, *Proc. SPIE*, *4540*, 100–111.

Ward, W. E., W. A. Gault, N. Rowlands, S. Wang, G. G. Shepherd, I. C. McDade, J. C. McConnell, D. Michelangeli, and J. Caldwell (2003), An imaging interferometer for satellite observations of

wind and temperature on Mars, the dynamics atmosphere Mars observer (DYNAMO), in *Applications of Photonic Technology 5*, edited by R. A. Lessard, G. A. Lampropoulos, and G. W. Schinn, *Proc. SPIE*, *4833*, 226–236, doi:10.1117/12.473823.

Ward, W. E., et al. (2010), On the consistency of model, ground-based, and satellite observations of tidal signatures: Initial results from the CAWSES tidal campaigns, *J. Geophys. Res.*, *115*, D07107, doi:10.1029/2009JD012593.

Wiens, R. H., G. G. Shepherd, W. A. Gault, and P. R. Kosteniuk (1988), Optical measurements of winds in the lower thermosphere, *J. Geophys. Res.*, *93*, 5973–5980, doi:10.1029/JA093iA06p05973.

Wiens, R. H., W. F. J. Evans, M. S. Zalcik, A. H. Manson, and G. G. Shepherd (1995), WINDII observation of a PMC breakup event during ANLC-93, *Geophys. Res. Lett.*, *22*, 2797–2800, doi:10.1029/95GL03023.

Wiens, R. H., V. P. Bhatnagar, and L. L. Cogger (1999), WINDII measurements of nightglow enhancements in the South Atlantic magnetic anomaly zone, *Geophys. Res. Lett.*, *26*, 2355–2358, doi:10.1029/1999GL900515.

Winick, J. R., P. P. Wintersteiner, R. H. Picard, D. Esplin, M. G. Mlynczak, J. M. Russell III, and L. L. Gordley (2009), OH layer characteristics during unusual boreal winters of 2004 and 2006, *J. Geophys. Res.*, *114*, A02303, doi:10.1029/2008JA013688.

Witasse, O., J. Lilensten, C. Lathuillère, and P.-L. Blelly (1999), Modeling the OI 630.0 and 557.7 nm thermospheric dayglow during EISCAT-WINDII coordinated measurements, *J. Geophys. Res.*, *104*, 24,639–24,655, doi:10.1029/1999JA900260.

Xu, J., A. K. Smith, G. Jiang, H. Gao, Y. Wei, M. G. Mlynczak, and J. M. Russell III (2010), Strong longitudinal variations in the OH nightglow, *Geophys. Res. Lett.*, *37*, L21801, doi:10.1029/2010GL043972.

Yee, J.-W., G. Crowley, R. G. Roble, W. R. Skinner, M. D. Burrage, and P. B. Hays (1997), Global simulations and observations of $O(^1S)$, $O_2(^1\Sigma)$ and OH mesospheric nightglow emissions, *J. Geophys. Res.*, *102*, 19,949–19,968, doi:10.1029/96JA01833.

Yudin, V. A., B. V. Khattatov, M. A. Geller, D. A. Ortland, C. McLandress, and G. G. Shepherd (1997), Thermal tides and studies to tune the mechanistic tidal model using UARS observations, *Ann. Geophys.*, *15*, 1205–1220, doi:10.1007/s00585-997-1205-9.

Yudin, V. A., M. A. Geller, B. V. Khattatov, D. A. Ortland, M. D. Burrage, C. McLandress, and G. G. Shepherd (1998), TMTM simulations of tides: Comparison with UARS observations, *Geophys. Res. Lett.*, *25*, 221–224, doi:10.1029/97GL03584.

Zhang, S. P., and G. G. Shepherd (1999), The Influence of the diurnal tide on the $O(^1S)$ and OH emission rates observed by WINDII on UARS, *Geophys. Res. Lett.*, *26*, 529–532, doi:10.1029/1999GL900033.

Zhang, S. P., and G. G. Shepherd (2000), Neutral winds in the lower thermosphere observed by WINDII during the April 4–5th, 1993 storm, *Geophys. Res. Lett.*, *27*, 1855–1858, doi:10.1029/2000GL000034.

Zhang, S. P., and G. G. Shepherd (2002), Neutral winds and $O(^1S)$ emission rates in the lower thermosphere as measured with WINDII/UARS during the April 4–5th 1993 and February 1994 geomagnetic storms, *J. Atmos. Sol. Terr. Phys.*, *64*, 1201–1214, doi:10.1016/S1364-6826(02)00069-X.

Zhang, S. P., and G. G. Shepherd (2004), Solar influence on the $O(^1D)$ dayglow emission rate: Global-scale measurements by WINDII on UARS, *Geophys. Res. Lett.*, *31*, L07804, doi:10.1029/2004GL019447.

Zhang, S. P., and G. G. Shepherd (2005a), On the response of the $O(^1S)$ dayglow emission rate to the Sun's energy input: An empirical model deduced from WINDII/UARS global measurements, *J. Geophys. Res.*, *110*, A03304, doi:10.1029/2004JA010887.

Zhang, S. P., and G. G. Shepherd (2005b), Variations of the mean winds and diurnal tides in the mesosphere and lower thermosphere observed by WINDII from 1992–1996, *Geophys. Res. Lett.*, *32*, L14111, doi:10.1029/2005GL023293.

Zhang, S. P., and G. G. Shepherd (2008), Extreme longitudinal disturbances in the mesosphere and thermosphere observed with the Wind Imaging Interferometer on UARS, *Geophys. Res. Lett.*, *35*, L16802, doi:10.1029/2008GL034352.

Zhang, S. P., R. H. Wiens, B. H. Solheim, and G. G. Shepherd (1998), Nightglow zenith emission rate variations in $O(^1S)$ at low latitudes from wind imaging interferometer (WINDII) observations, *J. Geophys. Res.*, *103*, 6251–6259, doi:10.1029/97JD03326.

Zhang, S. P., R. G. Roble, and G. G. Shepherd (2001), Tidal Influence on the oxygen and hydroxyl nightglows: Wind Imaging Interferometer observations and thermosphere/ionosphere/mesosphere electrodynamics general circulation model, *J. Geophys. Res.*, *106*, 21,381–21,393, doi:10.1029/2000JA000363.

Zhang, S. P., C. McLandress, and G. G. Shepherd (2007), Satellite observations of mean winds and tides in the lower thermosphere: 2. WINDII monthly winds for 1992 and 1993, *J. Geophys. Res.*, *112*, D21105, doi:10.1029/2007JD008457.

Zwick, H. H., and G. G. Shepherd (1973), Upper atmospheric temperatures from Doppler line widths—V. Auroral electron energy spectra and fluxes deduced from the 5577 and 6300 Å atomic oxygen emissions, *Planet. Space Sci.*, *21*, 605–621, doi:10.1016/0032-0633(73)90073-1.